SAPIENZA
UNIVERSITÀ DI ROMA

ISTITUTO ITALIANO
DI TECNOLOGIA

A thesis submitted for the degree of
PhD in Theoretical and Applied Mechanics
2019

Cavitation-enhanced permeability in a vessel on a chip

by : Giulia Silvani

Department of Mechanical and Aerospace Engineering.
"La Sapienza", University of Rome

CLNS@Sapienza
Istituto Italiano di Tecnologia

Supervisor : Prof. Carlo Massimo Casciola
Tutors : Giovanna Peruzzi, PhD and Giorgia Sinibaldi, PhD

> *We are slowed down sound and light waves, a walking bundle of frequencies tuned into the cosmos. We are souls dressed up in sacred biochemical garments and our bodies are the instruments through which our souls play their music.*
>
> (Albert Einstein)

Contents

Abbreviations

AM	**A**cetoxy **M**ethyl
AFM	**A**tomic **F**orce **M**icroscopy
BF	**B**right **F**ield
BBB	**B**lood **B**rain **B**arrier
BSA	**B**ovin **S**erum **A**lbumin
ECs	**E**ndothelial **C**ells
ECM	**E**xtra **C**ellular **M**atrix
EGM	**E**ndothelial **G**rowth **M**edium
FDA	**F**ood and **D**rug **A**dministration
FFT	**F**ast **F**ourier **T**rasform
HUVEC	**H**uman **E**ndothelial **V**ascular **C**ell
HIFU	**H**igh **I**ntensity **F**ocus **U**ltrasound
IF	**I**mmuno **F**luorescence
MB	**M**icro **B**ubble
MI	**M**echanical **I**ndex
PACs	**P**hoto **A**ctive **C**omponents
PBS	**P**hosphate **B**uffer **S**saline
PCF	**P**ulse **C**entre **F**requency
PDMS	**P**oly **D**i **M**ethyl **S**iloxane
PEB	**P**ost **E**xposure **B**acking
PFA	**P**paraFormalDehyde
PGMEA	**P**ropylene **G**lycol **M**onomethyl **E**ther **A**cetate
PD	**P**ulse **D**uration
PNP	**P**eak **N**egative **P**ressure

POC	**P**oint **O**f **C**are
PRF	**P**ulse **R**epetition **F**requency
PRF	**P**ulse **R**arefactional **P**eak
RBEC	**R**at **B**rain **E**ndothelial **C**ells
RF	**R**adiation **F**orce
ROI	**R**egion **O**f **I**nterest
RT	**R**oom **T**emperature
SEM	**S**canning **E**lectron **M**icroscopy
TEM	**T**rasmission **E**lectron **M**icroscopy
TC	**T**issue **C**ompartment
UCAs	**U**ltrasound **C**ontrast **A**gents
US	**U**ltra **S**ound
UV	**U**ltra **V**iolet
VC	**V**ascular **C**hannel
VE-Cadherin	**V**ascular **E**ndothelial Cadherin
VWF	**V**on **W**illebrand **F**actor

Symbols

$A_{buckling}$	Area of the bubble in a buckled state	m^2
$C_{A,1/2}$	Concentration of a chemical specie A in compartment 1/2	$\mathrm{Kg\,m^{-3}}$
$C_{A,1/2}^{M}$	Concentration of a chemical specie A in compartment 1/2 at the membrane interface	$\mathrm{Kg\,m^{-3}}$
D	Diffusion coefficient of air in water	m^2/s
D	Transducer diameter	m
$D_{A,M}$	The diffusion coefficient of the chemical specie A through the membrane M	$\mathrm{m^2\,s^{-1}}$
f	Frequency	Hz
G	Shear modulus of the elastic layer	Pa
h	High of the microfluidic channel	m
$I_{A,2}$	Time-dependent fluorescent intensity in compartment 2	
I_{TC}	Light intensity in the tissue compartment	W/m^2
$I_{VC,0}$	Light intensity in the vascular channel	W/m^2
$J_{x,A}$	Diffusion flux of the chemical species A along x-direction	$\mathrm{mol\,m^{-2}\,s^{-1}}$
K_P	Paritition coefficient	
K_V	Compression modulus of the bubble	Pa
M_g	Molar mass of the incondensable gas in the bubble	Kg/mol
$M(t)$	Mass of the oscillating fluid	Kg
N	Near sound field	m

p	Liquid pressure	Pa
P	Permeability coefficient	cm/s
p_0	Liquid ambient pressure	Pa
p_a	Acoustic pressure amplitude	Pa
$p_a(x,t)$	Acoustic plane wave propagating linearly in space, x, and time, t	
p_b	Pressure inside the bubble	Pa
P_B	Blake threshold pressure	Pa
P_{cells}	Effective cells permeability coefficient	cm/s
$P_{cells-free}$	Permeability coefficient for the device without cells	cm/s
$p_{g,eq}(T_0)$	Equilibrium gas pressure	Pa
P_{opt}	Optimal threshold pressure for inertial cavitation	Pa
$p(R)$	Liquid pressure at the bubble interface	Pa
$p_{v,eq}(T_0)$	Equilibrium vapour pressure at temperature T_0	Pa
p_∞	Liquid pressure far from the bubble	Pa
Q	Volumetric flow or flow rate	$\mu l/min$
R	Bubble radius	m
$\mathbf{R}$	Universal constant of gas	$J/molK$
R_b	Radius of the bubble	m
$R_{b,0}$	Initial radius of the bubble	m
R_B	Blake critical radius	m
$R_{break-up}$	Critical break-up bubble radius	m
$R_{buckling}$	Bubble radius in a buckled state	m
S_π	Exchange surface	m^2
T	Temperature	°C
T_0	Liquid ambient temperature	°C
T_b	Temperature inside the bubble	°C
$T_{boiling}$	Boiling temperature	°C

$\mathbf{u}$	Liquid velocity	m
$\mathbf{u}(r,t)$	Liquid velocity at distance r from the bubble center at instant t	m/s
$\mathbf{u}(R,t)$	Liquid velocity at the bubble interface	m/s
V	Volume	m^3
$V(t)$	Volume of the oscillating fluid	m^3
w	Width of the microfluidic channel	m
Z	Acoustic impedance	Kg/m^2s
α	Acoustic attenuation coefficient	m^{-1}
$\dot{\epsilon}$	Displacement in a oscillatory system	$\mathrm{m\,s^{-1}}$
$\ddot{\epsilon}$	Displacement in a oscillatory system	$\mathrm{m\,s^{-2}}$
δ_M	Thickness of the membrane	m
γ	Polytropic constant	
κ_s	Shell dilatational viscosity	Pas
λ	Wavelength	m
μ_L	Dynamic liquid viscosity	Pas
ξ	Damping coefficient	m/s
$\xi(t)$	Position of a particle of an oscillating fluid	
ξ_0	Mean position of a particle of an oscillating fluid	m
ξ_1	Maximum displacement of a particle of an oscillating fluid	m
ρ_L	Density of the liquid	kg/m^3
σ	Surface tension	N/m
$\sigma_{breack-up}$	Critical breack-up tension	N/m
Σ_R	Effective surface tension	N/m
σ_{water}	Water surface tension	N/m
τ	Shear stress on endothelial surface	$dyne/cm^2$
τ_{wall}	Shear stress at parallel plates for a newtonian fluid flowing through them	$dyne/cm^2$
χ	Elastic modulus	N/m^2

ω_0	Natural bubble resonant frequency of the bubble	rad/s
$\omega_{0,M}$	Minneart natural bubble resonant frequency	rad/s

Chapter 1

Introduction

1.1 Enhanced-Drug Delivery system

Advances in pharmacology have led to a welcome increase in efficacy of disease treatments. However, enhancing therapeutic efficiency of conventional drugs is still a major challenge that involve and interest different scientific areas. Indeed, drugs would have to survive and overcome numerous obstacles of physical, chemical and biological nature before reaching the site of interest.

Currently, the success rate of traditional clinical therapies still remains low primarily due to the limited local accumulation of drugs to the site of interest. Due to the lack of the natural affinity to the target, for most therapeutic agents, only a small portion reaches the affected organ, such as in chemotherapy where roughly 99 % of the drugs administered do not reach the tumour site. Consequently, to improve drug efficiency, large dose of pharmaceutical agent needs to be administrated, causing risk of toxicity to the patient [1]. This aspect is of particular importance for anti-tumour drugs as their intolerable toxicity can lead also to systemic damage. In this context, the development of drug delivery systems -that refer to approaches, formulations or technologies for safely transporting drugs into the body- represents a possible solution to this unmet need [2].

The first experimental pharmacology dates to the early nineteenth century, when the Nobel prize Paul Ehrlich, the founder of chemotherapy, envisioned that it could be possible to kill specific microbes (such as bacteria), which cause diseases in the body, without harming the body itself. His postulate, the ‘magic bullets’, inspired generations of scientists that have decided to focus on the treatment of human diseases with new drugs synthesized for specific targets [3–5].

Indeed, several drug delivery strategies have been developed in order to maximize drug concentration at the target site while minimizing off-target effects [6, 7].

Intravascular route

Drugs can be introduced in the body via various pharmacological routes, depending on target localisation [8]. Among all, the intravascular route seems the most useful for drug delivery to diverse organs since pharmaceutical agents are instantaneously distributed to otherwise inaccessible sites of action. Even so, the quantity delivered is limited by several factors. To avoid damage to healthy tissue and toxicity risk for the patient, the maximum therapeutical dose, for a safe blood concentration, is restricted. Besides, a drug is only active for a finite period because of degradation, limiting the circulation time. Most important, in order to reach the intended target and become active, drugs must diffuse out of the vascular wall, travel through the extracellular matrix (ECM) and reach the intracellular compartment of interest.

The diffusion is hampered by the endothelial barrier lining the innermost surface of blood vessels, forming an interface between the circulating blood and the ECM [9, 10]. Capillaries are the smallest of blood vessels consisting of an endothelium supported by its basal lamina. The barrier is made of a continuum, single layer of specialized cells, called vascular endothelial cells (VECs), tightened together by a system of protein complexes, to form a highly selective physical membrane (Figure 1.1) [11].

Molecule exchange, ranging from 0.1 nm (sodium ion) to 11.5 nm (immunoglobulin G) in diameter, through the endothelium barrier, is tightly regulated and occurs through two specific transport pathways. The transcellular pathway (transcytosis) involves the molecule transport through the cellular membrane, while in the paracellular pathway passage occurs between adjacent VECs [12].

VECs are connected by cell-cell junctions which tight together neighbouring

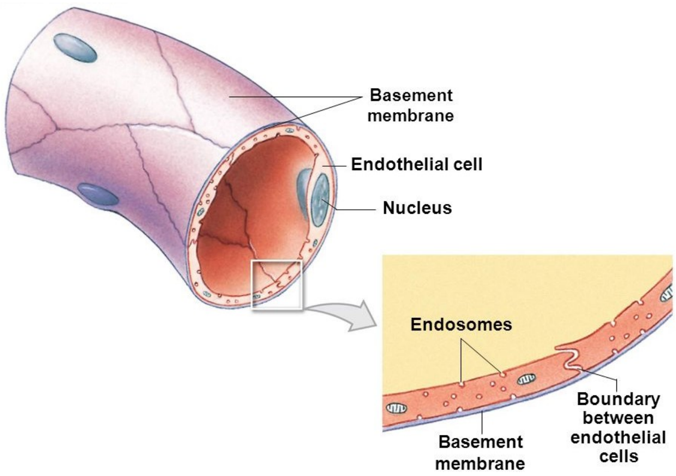

FIGURE 1.1: **Continuous capillaries.** The thinness of the wall, the small size of these vessels, and the slowness of blood flow permit exchange of materials between the blood and interstitial fluid [11].

cells and co-ordinately open and close to allow or deny molecule passage depending on their size and charge. Specialized endothelial barriers involve different junctions but the most important for barrier selectivity are tight and adherent junctions [13]. The typical protein in adherent junctions is the vascular endothelial cadherin (VE-cadherin), a protein responsible for regulating vessel permeability and endothelium integrity [14–16].

The maintenance of this size-selective property is crucial for several physiological functions, including normal tissue-fluid homeostasis, angiogenesis, vessel tone and most important, host defence [10, 17]. On the other hand, endothelial barriers, create a considerable challenge for the treatment of many diseases, such as disorders related to the central nervous system. The blood-brain barrier (BBB) is, indeed, the most highly specialised vasculature consisting of VECs connected by tight junctions, surrounded by pericytes and packed by astrocytes [18]. Since the BBB plays a fundamental role in protecting and maintaining the homeostasis of the brain, the delivery of drugs is much more difficult than that to other compartments of the body.

Concerning the transcellular pathway, the central biological structure is the cellular membrane, consisting of a lipid bilayer, where the hydrophilic lipid heads are exposed to the aqueous environments of the cytoplasm from one side and the ECM on the other, with the hydrophobic hydrocarbon tails sandwiched in the intra-leaflet space [19]. The ability of a drug to cross cell's membrane depends on the characteristics of the targeted tissue as well as the size and physicochemical properties of the drug. Many hydrophilic or charged drugs are unable to enter the cell by diffusion and rely on endocytosis mechanisms for internalization [20].

From these evidences, endothelium and cell membranes together with the close extracellular matrix, represent the main physiological obstacle for the real efficiency of a therapy. In this context, several targeted delivery methods have been developed with the aim at enhancing the efficiency of a therapy by increasing the local up-take of pharmaceutical agents with specific sub-cellular address, minimizing off-target effects.

Most of these strategies consists of a better design and characterisation of therapeutics [21] or encapsulate a drug into nano or micro-meter sized drug carriers. The latter option utilizes a variety of particles, such as liposomes (200 nm or less in diameter) [22] and other self-assembling systems [23]. Encapsulating drugs within a vesicle, instead of attaching them to a single polymer chain, has the potential to provide a higher drug-carrying capacity [24]. Liposomes possess many advantages in drug delivery applications, such as the capacity for size and surface manipulations. After being modified with targeting groups, their drug delivery efficiency to specific cells and subcellular compartments could be further improved [25, 26]. More importantly, both the chemical compositions (phospholipids) and the lipid bilayer structures of liposomes are extremely close to the cellular membranes, making them highly compatible with the biological environment [25].

Although carrier-mediated delivery systems have been shown to increase target affinity and in turn, the local amount of drug delivered, there is growing evidence that nano-drug carriers are still too large to cross the endothelium and the cellular membrane [27, 28]. Even when tumour vasculature is permeable to 100-nm liposomes, the drug distribution pattern is extremely susceptible to a large variance in vascular permeability [29].

An alternative strategy to chemical manipulation or encapsulation of the drug molecule, is to actively increase the sensitivity of the tissue for the drug. The so-called membrane-disruption modalities are primarily physical, involving the introduction of transient discontinuities in the plasma membrane via mechanical, electrical, thermal, optical or chemical means [30] as shown in Figure 1.2.

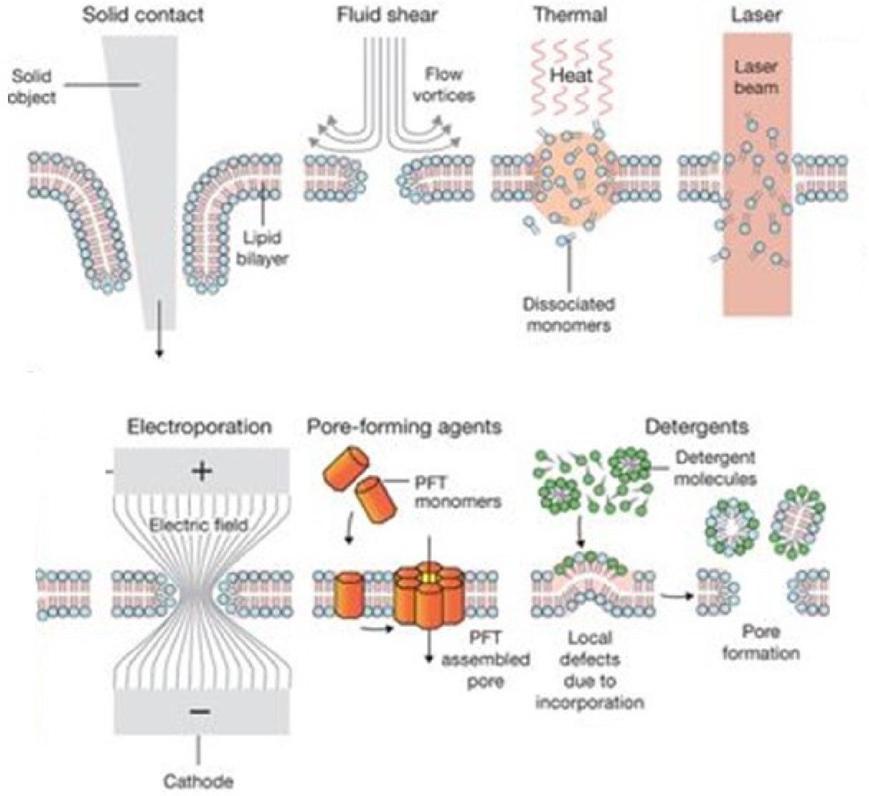

Figure 1.2: **Membrane disruption modalities.** Image taken from [30]. Schematic of plasma membrane disruption by mechanical forces (solid contact and fluid shear), thermal effects, focused lasers, electric fields, lodging of pore-forming agents that assemble into complexes, and the action of detergents that solubilize membrane lipids.

These approaches belong to the category of permeabilization method since a cell becomes permeable to a substance, *i.e.* drug-carrier, when membrane disruptions are big enough to allow passage through the membrane.

An example of mechanical membrane-disruption modality is a patch with microneedles for transdermal drug delivery. These needles pierce the stratum corneum, the outermost layer of the epidermis, which normally inhibits drugs to cross the skin at therapeutic rates, resulting in enhanced drug uptake [31]. Such an approach is limited to topical drug delivery due to accessibility. Conversely, treating a solid tumour within the body to increase the uptake of chemotherapeutic drugs requires localized approaches, preferably non-invasive and possibly customized 'on demand'.

A promising mechanically triggered drug delivery method combines ultrasound (US) with microbubbles (MBs), known as USMB-mediated drug delivery [32, 33]. MBs, already approved for human safety [34], were originally developed and are still clinically used as ultrasound contrast agents (UCAs) for enhanced-US imaging [35]. More recently, they have been proposed for therapeutic applications, drug delivery in particular [36–38]. In addition to a diagnostic application, the dynamic behaviour of intravenously administrated MBs in response to US excitation is used as a non-invasive therapeutic modality to promote the local permeabilization of challenging biological barriers by inducing endothelium integrity alteration [39–41]. Thanks to the fast response of junction proteins at cell-cell border, drug extravasation upon USMB exposure may be coordinated by suitably tuned mechanical actions. Indeed, oscillating MBs can induce the dynamic opening and closure of inter-endothelial junctions, giving rise to a reversible interruption of the endothelial layer continuity. Doing so, macromolecule delivery is facilitated through tissue regions where diffusion alone is inadequate.

The so-called acoustic cavitation method is especially promising for enhancing drug delivery given its ability to transiently and reversibly increase vascular- and membrane permeability. Hence, the growing interest for basic studies aim at quantifying the effect of the irradiation on endothelial barrier function contributing to the state of the art in this field.

1.2 Diagnostic and Therapeutic US

Sound waves are pressure waves propagating through a certain medium that carries energy and momentum outward from its source and results in alternating compression and rarefaction of the medium itself. US are defined as any sound wave above 20 kHz frequency, the threshold of audible sound for humans. The simplest mathematical description of US is a pure sine wave (Figure 1.3), characterised by a single frequency, f, and hence a single period, T, in the time domain, corresponding to a single wavelength, λ,in space [42].

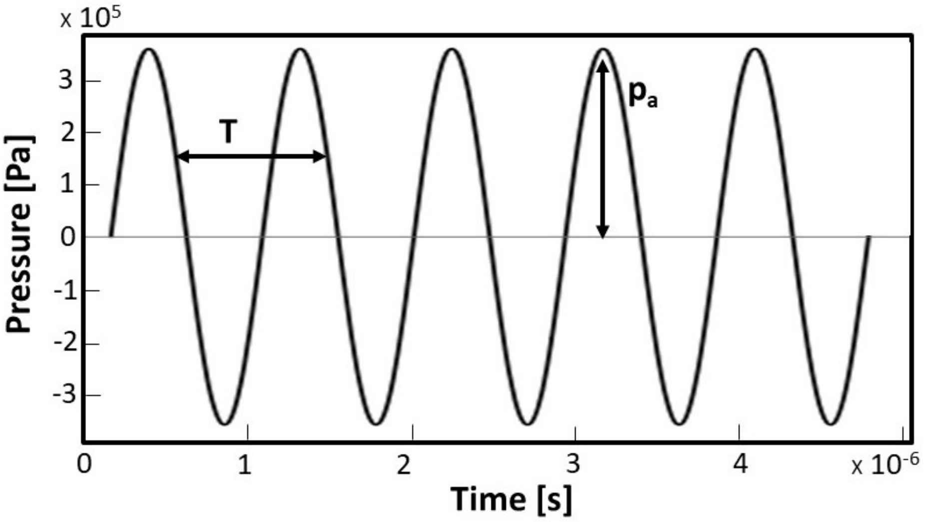

FIGURE 1.3: **Pure sine wave.** An example of a 5 Cycle, 1,0 MHz sinusoidal wave with peak amplitude of 380kPa. The period and amplitude of the sound wave are denoted respectively by symbols T and p_a.

The wave amplitude is typically expressed in terms of pressure, p, although it can be equivalently represented in terms of particle displacement, velocity or acceleration. The equation describing an idealised plane wave propagating linearly in space, x, and time, t, can be written as:

$$p_a(x,t) = p_a e^{i2\pi(ft - \left(\frac{x}{\lambda}\right))} e^{\alpha x}. \tag{1.1}$$

where p_a is the wave pressure amplitude and the last term, $e^{\alpha x}$, describes the attenuation of the wave as it propagates through inhomogeneous media, i.e. soft tissues, due to viscous absorption and scattering. In most practical biomedical applications, US is generated by a piezoceramic crystal as a series of pulses rather than a continuous wave as shown in Figure 1.4. In this way, thermal effects, produced by the attenuation of the sound wave as it passes through the tissue, are avoided. A pulse consists of a number of cycles at a given frequency. Due to its finite length, however, the pulse will contain a broader range of frequencies than does a continuous wave, but it may be characterized by the average frequency of its Fourier representation, known as the pulse centre frequency (PCF). However, the shorter the pulse the wider the range of frequencies it contains.

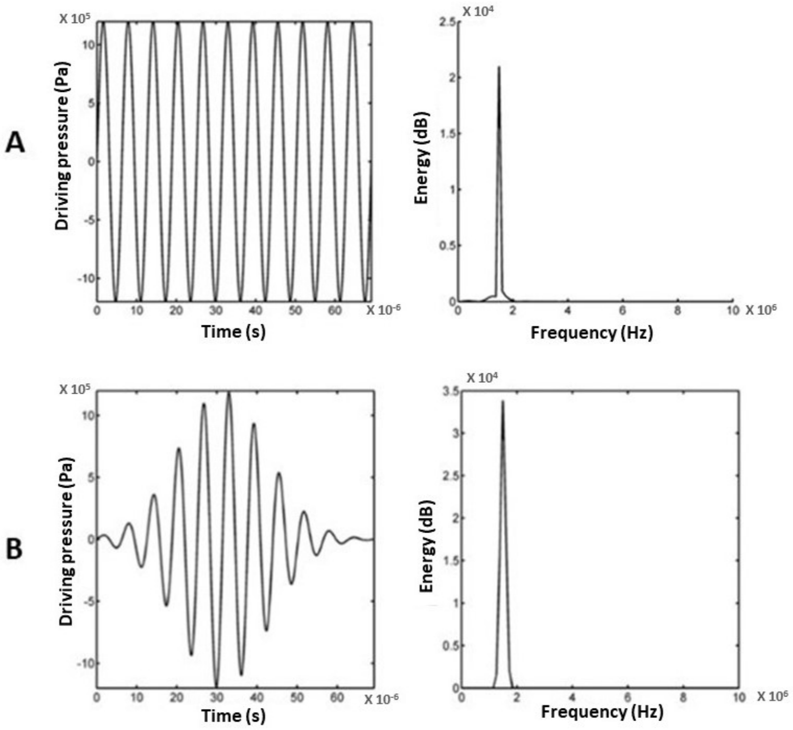

FIGURE 1.4: **Image taken from Azmin[49] A**. Example of an idealised US continuous wave: (i) time domain (ii) frequency domain. **B**. Example of an US pulse (10 cycle Gaussian enveloped sinusoid): (i) time domain (ii) frequency domain.

Since the 19th century, when first experimental studies on the properties of sound waves were published, the application of US have increased enormously, especially in medical research [43]. US application as a medical diagnostic tool began around the 1940s when Karl Dussik, a neurologist at the University of Vienna, attempted to locate brain tumours by measuring the transmission of US beams through the head [44]. Since then, diagnostic US pulses, typically with a PCF in the megahertz range, *e.g.* 3-15 MHz, has evolved into one of the main medical imaging modalities around the globe [45].

In diagnostic US, energy deposition in tissues, is minimal in order to avoid biological effects. Temperature elevations and the potential for bioeffects are kept relatively low or negligible by carefully limiting temporal average intensities, and generally imposing short exposure durations, *i.e.* 1 to 5-cycle per pulse [46]. Thus, US waves can travel through the body without being absorbed by biological tissues and create images based on the difference in impedance Z between tissues, Z being the product between the density and sound velocity of the material through which sound propagates. Indeed, the larger the impedance mismatch, the higher the intensity of the reflected US.

On the other hand, therapeutic US bursts, consisting of lower PCF, often between 500 kHz and 2 MHz, are based on intentionally depositing US energy to create specific effects. The absorption of such waves by the human body results in molecular oscillatory motion. This energy transfer is converted into heat proportional to the intensity of the US. If this heat is not dissipated by physiological means, a localized increase in temperature will occur and thermal therapeutic effects may arise. As a general rule, the greater the rate of energy being deposited in the tissue, the more pronounced the effects being generated. Low-level energy deposition is typically used for healing purposes in physical therapy [47]. Then, higher rates of energy deposition are presently being used as thermal ablation of tumours [48].

The thermal effects of US is determined by the frequency, the US intensity (dosage) and the type of tissue that is exposed to the acoustic energy. Therapeutic applications of ultrasonic heating either utilize longer durations of heating with unfocused beams or shorter irradiation with high intensity focused US (HIFU). However, the potent application of US for therapeutic efficacy also carries the risk for adverse bioeffects which can lead to significant patient injury [49]. Therefore, standardization, US dosimetry and side-effects risk minimization must be carefully considered in order to provide an optimal outcome for the patient.

1.3 Cavitation: a non-thermal mechanism of US

In addition to thermal therapies, there are presently a large range of applications based on the non-thermal mechanism of US. Any process that can produce a biological effect without a significant degree of heating, *e.g.* one producing an increase of less than about 1°C above normal physiological temperature, is a nonthermal mechanism [50].

Several *in vitro* experimental designs appear to have successfully isolated the nonthermal from the thermal effects of US within cellular systems to identify the mechanical aspects [51, 51–53]. In 1980, Love and Kremkau [52] demonstrated that by eliminating extracellular tissue structures (collagen, fibrin, elastin, etc) and placing only the cells in tissue culture media, maintained at 37°C, they could treat cells with US at therapeutic levels without significant increases in temperature (less than 0.58°C over a 10 min exposure).

There are two general classes of non-thermal mechanisms, namely cavitation and non-cavitation, that may arise during exposure of a biological material to US. These generally occur in the presence and absence, respectively, of gas bodies.

Referring to the non-cavitation mechanisms, if the traveling acoustic wave, that carries energy, impinges on an object that absorbs the energy, the interaction becomes manifest as a unidirectional force on the object, also known as radiation force (RF) [54, 55]. The magnitude of RF is W/c, the ratio of the acoustic power to the speed of sound in the medium. If RFs are large enough, biological tissue responds by distorting/bending in the direction of the incident sound wave with a degree of displacement determined by the elastic (Young's) modulus of the tissue [56]. Tissues having low physical strength may lose their mechanical integrity or otherwise disrupted, if this distortion is of enough magnitude.

On the other hand, US can also produce direct physical effects in liquids by a process known as Acoustic cavitation. This process can be defined as any activity involving a population of MBs stimulated into motion by an acoustic field and resulting in localized mechanical actions. The gas bodies required for this class of mechanisms fall into one of three categories. They may be naturally present in the body, as in the lung or intestine or they may nucleate from pre-existing cavitation nuclei within the body by the passage of an acoustic wave of sufficient intensity, *e.g.* in the kidney during shock wave lithotripsy [60]. Even more, they may be produced by an external process and subsequently introduced into the body, *e.g.* by intravenous injection, in order to be distributed to the site of action.

In the classical view, once introduced into the bloodstream, the dynamic behaviour of MBs may induce mechanical actions on the vessel wall eliciting endothelium permeabilization by the transient opening of ECs membranes and reversibly increasing intercellular distances thereby temporarily dissolving the inter-endothelial junctions [61–63]. The first process, called sonoporation, consists in pores formation within the cellular membrane and was firstly observed in 1999 by electron microscopy [64]. In the same years, it was also found that MBs activated by US into the blood vessels transiently increase the space between VECs [65]. This other process is known as sonopermeabilization and results in the distribution of particles into the extracellular space [65].

Recent theoretical models suggest a novel point of view for cavitation-enhanced drug delivery. The application of high intensity US may result in transient cavitation, including bubble nucleation, expansion, collapse and subsequent shock waves [66, 67]. The model refers to the lipid bilayer and focus the attention on the hydrophobic chains forming the inner layer between the two membrane leaflets which may host dissolved gas. Under the negative pressure due to US excitation gas pockets may coalesce in the intra-leaflet space nucleating MBs. Their subsequent expansion would lead to membrane permeabilization by mechanically forcing the bilayer structure and the junctions holding together the endothelium. The model may explain why relatively moderate US intensity is able to induce significant bioeffects, although experimental evidences don't exist yet. However, when pre-formed MBs are injected before sonication, the required acoustic power level is substantially reduced, and the effect is restricted in a more controllable manner to the vasculature. In this way, adverse bioeffects, i.e. ischemic, apoptotic areas or bleeding are mitigated [68]. This thesis only considers the classical perspective of cavitation enhanced endothelium integrity.

The following sections provide a description on how acoustic cavitation mechanisms can be exploited to enhance the delivery, penetration and distribution of therapeutics through the vessel wall.

1.3.1 Microbubble Cavitation activity on a vessel wall

In intravascular drug delivery, the bioeffects associated with cavitation are primarily caused by the dynamic behaviour of MBs in the near proximity of a vessel wall. Being filled with gas and/or vapour makes MBs highly responsive to changes in pressure and temperature, both of which can cause rapid and critical changes in their volume. These volume changes may lead to mechanical, thermal and chemical phenomena that can impact their surroundings. In the following paragraphs, a list of mechanisms is reported while a more detailed physical explanation will be given in Chapter 2.

Mechanical Action

When injected into the bloodstream and exposed to a time-varying acoustic pressure, MBs undergo volumetric oscillations, i.e. contracts and expands, with consequent bio-effects depending on several US parameters such as the pressure amplitude or Peak Negative Pressure (PNP), the excitation frequency, the pulse length (PL) and the pulse repetition frequency (PRF) of the acoustic beam [69].

Bubbles can indeed stably oscillate at low acoustic pressure (stable cavitation) or violently collapse at higher acoustic pressure (inertial cavitation) near a vessel wall, inducing endothelium integrity alteration through several mechanical and fluid mechanical stresses as schematically sketched in Figure 1.5.

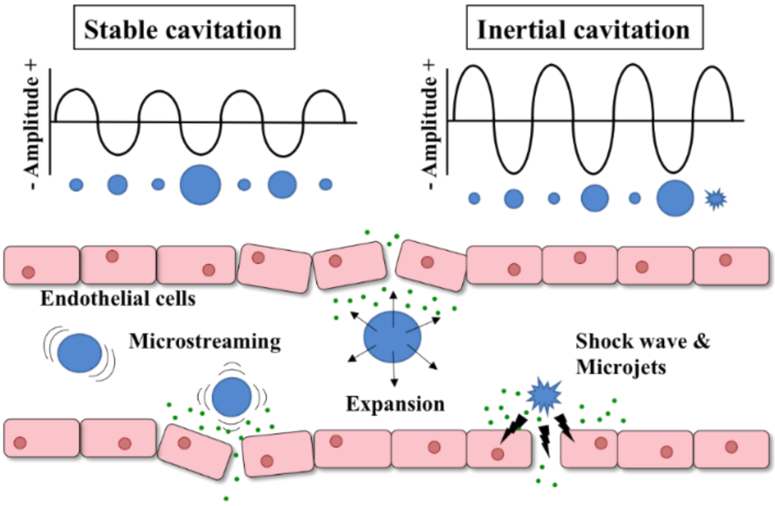

FIGURE 1.5: **Sketch of stable and inertial cavitation showing the effects on the endothelium [32].** Upon stimulation by US, oscillating microbubbles can increase drug internalization through membrane pores, and/or junction opening.

When MBs stably oscillate over time, upon exposure to low PNP (typically in the range of 0.5 – 0.8 MPa), they re-radiate energy from the incident US field in the form of spherical pressure waves. Owing to the compressibility of MBs, the amplitude of these waves is considerably larger than the acoustic scattering from a rigid sphere of equivalent size [70]. Doing so, oscillating MBs push the endothelial barrier during the bubble expansion phase and pull it during the contractions phase. These repeated mechanisms of push-pull could potentially induce the junctions opening, promoting drugs diffusion into the interstitial.

Momentum transfer from the oscillating bubble to the surrounding liquid through interfacial friction can also produce localized flui−flow pattern called microstreaming [71]. An oscillating bubble, in a traveling sound field, generates a small scale (hence "micro"), vigourous circulatory motion consisting of fluctuation in velocity and pressure in the viscous fluid surrounding the bubble. When the temporal average of these fluctuations is non−zero, a steady streaming flow appears. This phenomenon is a consequence of the vorticity generated within the oscillatory boundary layer [72], that is the boundary layer formed in proximity of the bubble wall due to its oscillatory motion. Due to this vorticity, the streaming velocity at the layer borders induces an outer streaming [73], giving birth to different flow patterns depending on the acoustic frequency and bubble size. If the bubble is close to a surface, such as vessel wall, it can exhibit highly non spherical oscillations [74] giving rise to higher microstreaming velocities.When a cell is subjected to such a strong fluid velocity gradient, the fluid will exert greater force on the side of the cell near the bubble and less force on the side farther away. This unequal distribution of forces results in shearing stresses that may increase strain in the cellular membrane and even exceed its critical value for membrane rupture. Because cells exhibit viscoelasticity, some minimum time is required for a given level of shear stress to disrupt a membrane and potentially enabling drug release. Thus, more than one exposure to a high stress field may be required for microstreaming to produce significant cell's damage. Experimentally, it has been shown that cavitation microstreaming might cause vesicle rupture due to the shear forces present in the proximity of to the bubble [75, 76]. Hence, VECs may temporarily loosen junction integrity under such forces.

At higher PNP ($>$ 1 MPa), the bubble oscillation may become unstable and the bubble may undergo "inertial cavitation", *i.e.* expand up to a maximum radius and very rapidly collapse to a radius extremely small, due to the dominant role of the liquid inertia [69]. During inertial collapse, the motion of the surrounding fluid may reach high speed such that the rising pressure within the bubble, which easily counteracts this momentum at low acoustic intensities, cannot resist the in-rushing liquid. What follows is the formation of shockwaves in the surrounding fluid that will propagate outwardly as a spherically diverging wave. When collapsing bubbles are in the proximity of solid boundaries, e.g. vessel wall, the collapse will be asymmetrical and can result in the formation of high-speed fluid microjets [77]. A biological cell exposed to such a shock will briefly experiences vary large stress [78–80] followed by membrane disruption.

Thermal Action

The nonlinear character of MBs oscillations (as later explained in Chapter 2) leads to energy being re-radiated over a range of frequency. At moderate driving pressures (< 0.5 MPa), the bubble spectrum contains integer multiples (harmonics) of the driving frequency while at higher pressures (> 0.5MPa), it also contains fractional components (subharmonics and ultraharmonics). Since the absorption of US energy by a biological tissue is proportional with frequency, the higher harmonics re radiated by the oscillating MBs also leads to heating of the immediate surrounding [81, 82]. Consequently, thermal ablation of tissue and release of drugs from thermally sensitive carriers can be obtained [83]. The increased temperature inside the bubble, during compression phases of the US wave, also produces thermal conduction from the compressed gas core to the surrounding liquid. Whether one of both mechanisms take place depends on different parameters, *i.e.* bubble size, the acoustic pressure driving the phenomenon and the viscosity of the medium [84]. Nevertheless, as the time constant of heat transfer is much longer than MBs oscillations time scale, conductive heating is typically negligible in US biomedical application .

Chemical Action

Surprisingly, when liquids are exposed to intense US, high-energy chemical reactions occur, often accompanied by the emission of light in a brief period of time

(<1 μs). Acoustic cavitation is responsible for both processes called sonochemistry and sonoluminescence [85], since the rapid bubble collapse in liquids results in an enormous concentration of energy. The mechanism consists of the conversion of the kinetic energy of liquid motion into heating of the gas inside the bubble. During this process, the interior bubble temperature may reach several thousand Kelvin [86] allowing sonochemical reactions to occur. The predominant chemical effects of such extreme conditions are through the generation of highly reactive oxygen species (ROS) [87]. The very high temperatures and pressures of collapsing gas bubbles lead to the thermal dissociation of water vapor into hydroxyl radicals ·OH and hydrogen atom ·H. In biological context, ROS have important roles in multiple biological processes such as cell signalling and homeostasis [88, 89]. Nevertheless, the relationship between cavitation activity and ROS formation has yet to be determined because direct measurements are challenged to be performed. The complex environment in which hundreds or thousands of cavitating bubbles interact with a biological tissue during their transient cavitation behaviour, precludes conventional measurement. However, recently has been shown that substantial ROS quantities can be generated in the surrounding fluid by acoustic cavitation under condition relevant for drug delivery (<1 MPa at 1 MHz) [90] and Sonoluminescence has been hypothesized to be a consequence of the recombination of these ROS [91].

1.3.2 Cavitation enhanced drug transport

Cavitation can be used to trigger release and/or activation of drugs but it no guarantees the effective delivery. Besides bubble oscillations, another process that may contribute to improve drug delivery across the endothelial barrier and drugs concentration at the target site relies on the RFs generated by a propagating US wave in the fluid. As already introduced in Sec. 1.3, the absorption of US energy results in acoustic forces that may act on an object along its propagation path. Owing to their high gas compressibility, MBs can experience an even higher acoustic radiation force, also known as the primary Bjerknes force. Indeed, a bubble in a sound field experiences not only the time-varying acoustic pressure $p(t)$, but also the gradient, *i.e.* the spatial variation, of the pressure ∇p. Conceptually, since the pressure is greater on one side of the bubble than on the other, it is clear that the bubble will tend to move in response to the acoustic field and that the magnitude of the driving force will depend on the bubble volume [92](see Chapter 2, Sec.2.3 for more details). First observation revealed that these forces had the ability to modulate the position and velocity of UCAs flow in the vasculature causing their displacement to the walls of blood vessels in laboratory animals [93, 94]. This can thereby improve MBs−cell contact, which might enhance cavitation-mediated target penetration of intravascular compounds [95–97], as sketch in Figure 1.6.

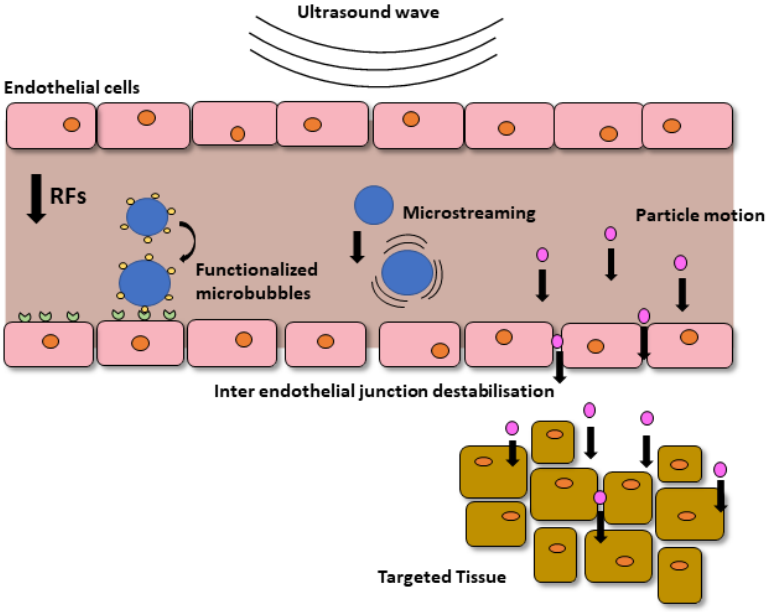

FIGURE 1.6: **Sketch of acoustic radiation forces acting on MBs and particles.** This translational force may facilitate the adhesion of targeted MB to the VECs, increase the extravasation of free circulating drugs and destabilize inter−endothelial junction by decrease the distance between oscillating MBs and the vessel wall.

With the same driving mechanism, RFs alone may enhance the diffusion of free circulating drug or drug-loaded nanoparticles into plasma membrane by pushing them towards the endothelial wall [98](Figure 1.6).

At high acoustic pressure, the primary radiation force results in the ballistic motion of bubbles which, travelling at high velocity, are violently pushed towards the vessel wall creating large opening in the endothelial monolayer and penetrating the surrounding tissue. Bubble “tunnelling” has been reported from different studies [99, 100] and may explain why vessel permeabilization appears to be reversable at low US intensities but correlated with permanent damage under more intense exposures [101].

In biomedical applications, the observable effects of cavitation are typically produced by a population of MBs and the influence of inter-bubble interactions should not be ignored. In addition to the primary Bjerkness force, another force, the secondary Bjerkness force, results from the interaction of nearby pulsating bubbles driven by the same sound field and may lead to effects that are relevant for drug delivery. In this case the oscillating bubble acts as a secondary US source causing the mutual attraction or repulsion between bubbles [102, 103] and inducing the formation of large clusters [104, 105] with a consequent larger concentration near the vessel wall. These clusters behave very differently from individual bubbles. For instance, they may experience much larger primary radiation forces inducing “tunnel” diameter through tissue much larger than that of the single bubble.

The ability to modulate microbubbles distribution has enabled several unique strategies such as facilitating receptor-ligand mediated adhesion of drug [106, 107] or deflecting the drug towards a vessel’s wall prior to be fragmented for improving local deposition of the carrying agents [108] (Figure 1.6). For a comprehensive review on how these types of interactions can be used for potential drug delivery applications, see Ferrara et al. [37]. For a theoretical description of these cascade of events, the reader is referred to Chapter 2.

1.4 Triggered cavitation bioeffects

US−driven MBs can trigger reversible bioeffects on cells and tissues, thus providing a temporary and reversible time-window for the delivery of macromolecules across endothelial barriers and biological membranes, as illustrated in Figure 1.7.

This time-window is related not only to cavitation events, but also to biological regulatory mechanisms. A crucial issue in controlled drug delivery is then to assess

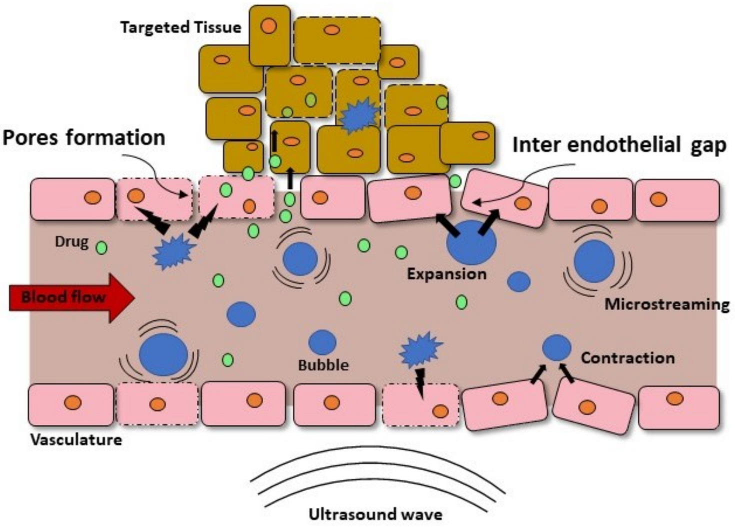

FIGURE 1.7: **Sketch of the two main triggered delivery routes enhanced by MBs cavitation**Sonoporation, which refers to reversable formation of pores within the cellular membrane by acoustic cavitation, allows macromolecule to passively diffuse into the cell. Inter endothelial gap, referring to the alteration of cell-cell junction integrity and to the increase of the distance between VECs, provides an active route for macromolecule delivery into the interstitial.

the biological effects induced by external stimuli aimed at facilitating drug passage, which is especially difficult to carry out IN VIVO. Previous studies achieved progress towards understanding the dynamic interactions of cavitating MBs with cells, spatiotemporally monitoring the cavitation activities [33, 109, 110]. Beside plasma membrane perforation (sonoporation) and inter-endothelial gap formation (sonopermeabilization), other cellular and molecular responses, in different spatial and temporal scales may be produced by US−activated MBs, thereby affecting the kinetics of cavitation−enhanced permeability and cell viability. These sections outline the bioeffects and the related biological regulatory mechanism involved in cavitation-enhanced drug delivery.

1.4.1 Sonoporation

Sonoporation refers to transient and reversible membrane perforation due to the mechanical stress of oscillating and collapsing MBs. This implies two sequential biophysical processes: membrane perforation and pore resealing through complementary biological mechanisms [111](Figure 1.8).

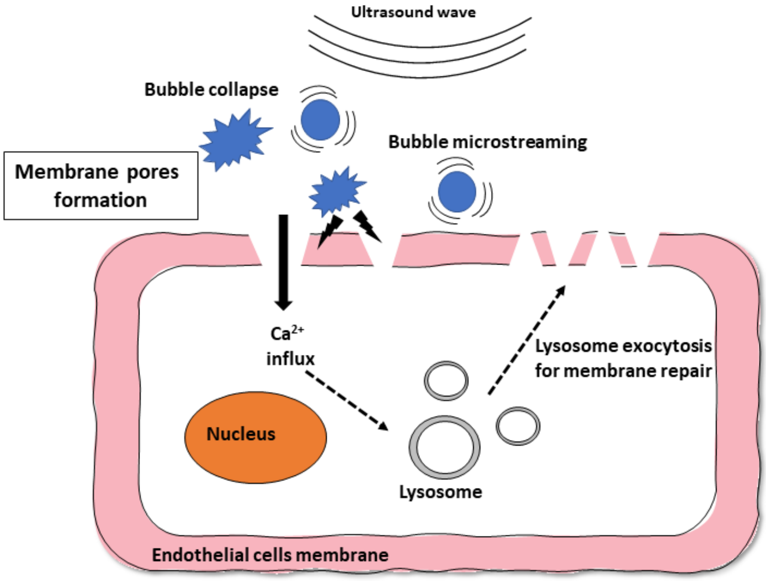

FIGURE 1.8: **Sketch of sonoporation mechanism**Acoustic cavitation can induce membrane pore formation that leads to C_a^{2+} entry and consequent lysosome exocytosis for membrane resealing.

Indeed, one of the principals bioeffects triggered by cavitation activity is the synchronously occurrence of intracellular C_a^{2+} influx, mainly due to the concentration-driven passive diffusion through the perforated membrane [112, 113]. As explained later, the influx of C_a^{2+}, increased by USMB directly application, can stimulate the process of exocytosis for membrane resealing [114] where secretory vesicle export material from intracellular compartments outside the cell and hence restore plasma membrane tension [115, 116].

In the last few years, in vitro high-speed photography and fluorescence microscopy provided a clear understanding of membrane perforation dynamics and cell−MBs interactions during cavitation [117–121]. Single−cell experiments [119, 120] indicate that when MBs are exposed to US pulses, stable or inertial cavitation occur and almost synchronously membrane perforation appear within several to tens of microseconds. What have been found is also that the spatial characteristics of membrane perforation, including the size and the location of pores on the plasma membrane, are mainly correlated with the magnitude of the acoustic field but also with some non−acoustic parameters, *e.g.* features related with bubbles or bubbles with cells.

Different studies have revealed that membrane perforation does not occur until MBs are close to the cellular membrane, suggesting the importance of the bubble-cell distance (d) for cavitation-perforated membrane [122–124]. Large distances would hamper direct mechanical contact between oscillating MBs and the cellular membrane, decreasing the influence of microstreaming on the membrane. This hypothesis was already posed by Ward in 2000 when he noticed the clear relationship between cell-MBs distance and membrane sonoporation efficiency [122]. In 2006, the research group of Professor de Jong show with real-time, ultrafast transmission microscopy that a direct interaction between MBs and the cellular membrane was required for membrane poration [117]. They attributed pore formation to stably cavitating MBs closely located to the cellular membrane, which were able to gently push and pull the membrane thus disturbing its functionality. In 2012, Zhou et al., found that shockwaves formed by inertial cavitation evoked membrane perforation when the ratio of d to the bubble diameter (D) was < 0.75 [125]. Given the importance of d in sonoporation, several physical and biochemical strategies were proposed to bring bubbles close to the targeted cell to achieve the critical distance for sonoporation, as sketched in Figure 1.6. Some of them regard the generation of primary RFs [108] or the use of biochemical methods such as the conjugation of specific ligands or antibodies to MBs [126].

Sonoporation induce pores that in turn determines the size of molecules or agents that can be delivered. For this reason, several research groups have tried to estimate the size of membrane pores arising during sonoporation [127, 128]. Nevertheless, size information has not been readily available due to the challenges in measuring dynamic, submicron sized pores opening. Post US assays such as atomic force microscopy (AFM), scanning electron microscopy (SEM) or transmission electron microscopy (TEM), often time consuming and labour intensive, have been used to estimate pore size but are intrinsically limited to static measurements. Real−time observation would provide more convincing results than the mentioned methods used for measuring pore sizes in samples post−exposure. Zhou et al., evaluated pores diameter as small as 10−100 nm by measuring the maximal transmembrane current via the patch−clamp technique after bubble exposure to low pressure amplitude (0.12 or 0.3 MPa) [127]. Using SEM microscopy, Kudo et al. determined large membrane perforation up to 1 μm after a more intense acoustic pressure (1.1 MPa) [129]. In general, the pore size induced by low pressure amplitude ranged from several tens to a few hundred nanometres [63], whereas higher acoustic pressure causes membrane perforation up to micron scale [119, 121, 130].

Sonoporated cells gradually recover to their pre−exposure state by two sequential biological processes: membrane resealing and cell recovery. The former is a process that refers to the rapid and short−term (minutes) closure of perforation sites, whereases the latter refers to the long−term (hours) return of the cell morphology to its initial state. Repair large or small pores may depend on different cellular mechanisms as elucidated by the identification in previous studies of endocytosis and exocytosis events involved in the resealing of cavitation-perforated membrane as later explain in sec. 1.4.3 (Figure 1.8). Different methods have been developed to evaluate the time−varying morphology of membrane resealing. The patch−clamp technique was used to show that pores close within second after switching US off [110]. Real-time confocal microscopy was performed to observe the achievement of pore closure and showed that the perforation sites within the area of less than $30\mu m^2$ successfully resealed in a short period of time (order of seconds), whereases large perforation areas ($> 100\mu m^2$) failed to reseal [121]. In other works, the perforated membrane was monitored through temporal changes on internalized impermeable marker and the time needed to completely reseal was found to be around 100 second [124, 125]. However, one hour after sonoporation, most cells exhibited a full recovery to their original membrane integrity.

All these findings suggest that the kinetics of membrane resealing, upon US exposure may ranging from the order of milliseconds to minutes depending on the degree of perforation.

1.4.2 Sonopermeabilization: reversable cavitation-induced inter-endothelial junction opening

US−driven MBs can temporarily alter the vascular integrity and open the inter-endothelial junctions, providing another effective route for macro-molecular delivery into extravascular tissue (Figure 1.9).

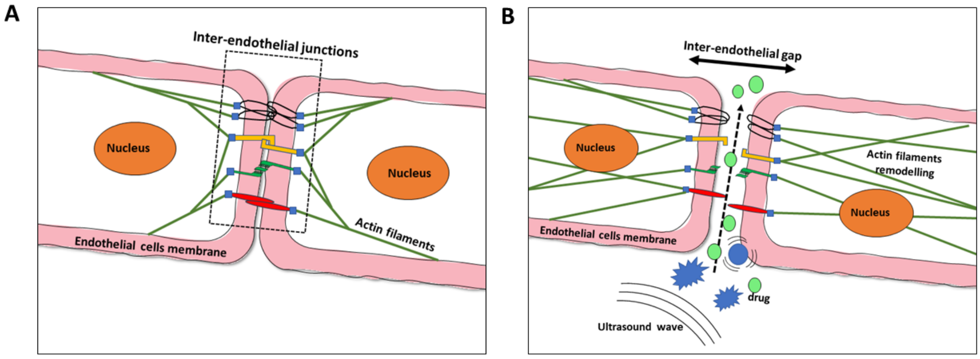

FIGURE 1.9: **Overview of the mechanism for intercellular junction opening by cavitation events.**Image modified from [59].**A.**Structural organization of different inter-endothelial junction pre-exposure. **B.** shear stress from oscillating and collapsing MBs resulting in the formation of inter−endothelial gap. Changes in the cytoskeleton, *i.e.* actin filaments remodelling, may disaggregate the proteins of inter−endothelial junction,facilitating drug passage through inter−endothelial space.

Previous *in vivo* studies observed changes of inter−endothelial junction associated with the interaction between cavitating bubbles and VECs [131, 131, 132]. These studies demonstrate that the expanded phase of large bubbles may causes circumferentially displacement of the vessels on a millisecond scale, increasing intercellular space and creating large gaps between cells. On the other hand, during the contraction phase of oscillating bubble, invagination of blood vessel occurs, leading to the delamination of the endothelial layer.

The magnitude of inter−endothelial junctions opening depends on the type and dose of cavitation, and on the relative localization of the bubbles to the endothelium [133]. However, in contrast to membrane perforation and resealing, there is a lack of understanding the spatiotemporal relationship between cavitation activities and the kinetics of inter−endothelial junction dynamic changes. Tracking the dynamics of opening and closure of proteins complexes is particularly challenge because of the lack in adequate technology to detect the microscopic events of MBs activities and the triggered biological response in the vasculature. Since now, SEM microscopy and immunofluorescence microscopy (IF) were the main methodologies used on post−exposure samples to analyse the molecular changes associated with cavitation-opened inter endothelial junction.

Sheikov et al., for example, found that the expression of trans−membrane protein Claudins, a component of tight junctions in blood−brain−barrier, significantly decreased 1-2 hours after exposure to USMB at low-power sonication and then returned to normal levels after 24h [62]. These temporal molecular changes indicate the gradual disintegration and reassembling of tight junction complexes post−exposure, proving the transient nature of the inter endothelial gap.

In 2009, Juffermans et al. showed that MBs oscillation at low acoustic pressure significantly affect the integrity of an endothelial monolayers by the formation of gap between VECs [134], as shown in Figure 1.10.

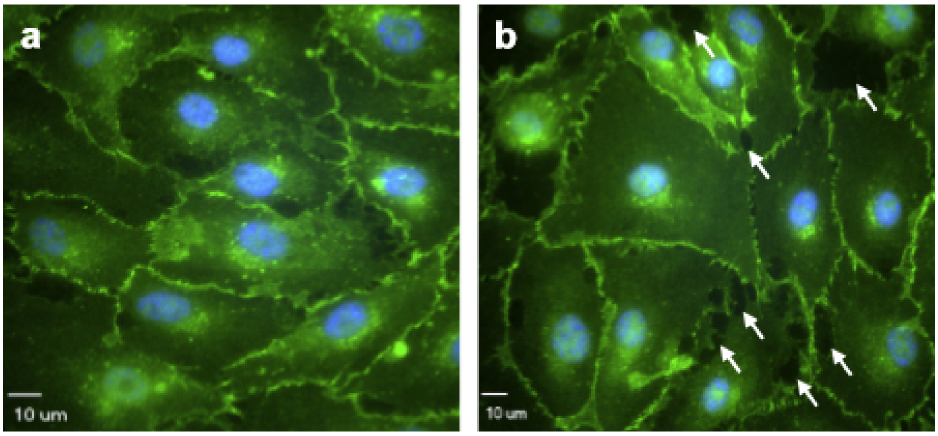

FIGURE 1.10: **Images taken from [134].** Representative images of human umbilical vein endothelial cells (HUVECs) stained for b-catenin (green), nuclei are stained in blue. Intercellular gaps are indicated by arrows. **A.** Control. Cells not exposed to US or microbubbles. **B.** Cells exposed to US and MBs.

They also found that the number of gaps were reduced to control levels within 30 minutes, suggesting that cell viability was not affected. However, because of the complexity of proteins structures and the difficulty to quantitatively establish the spatiotemporal correlation between cavitation activities and molecular changes, more sophisticated experiments need to be designed.

Bioeffects of cavitation-opened inter-endothelial junctions

The main bioeffect triggered by inter−endothelial junction opening is related to the actin cytoskeleton dynamic, in particular to the F−actin stress fibres rearrangement under mechanical stress by US-activated MBs exposure [134]. These structures, assembled from short filaments, are the main mechanic conduction pathways that converts mechanical stimuli exerted at the cellular membrane into intracellular biochemical signals [135]. In previous studies, it has been observed that changes in junction morphologies, typically stabilized by linkages to the circumpherential actin bundles [136], are related to the actin cytoskeleton dynamic [137]. Under mechanical stress, actin filaments are capable to reorganize into F-actin stress fibres transmitting contractile force to inter endothelial junctions, thus affecting junction architecture and endothelial permeability [138]. However, because of the non−uniform distribution of cavitation events, and the related mechanical forces around VECs in a blood−flow environment, it is difficult to observe the spatiotemporal relationship between cavitation events and actin remodelling in real−time. Previous studies determined that oscillatory strains from pulsed US with 0.17 – 0.29 MPa PNP promoted the fluidization of the filament cytoskeleton within 3 min post−exposure [139, 140]. In the presence of MBs, when cells were exposed to US with 0.1 MPa PNP, F−actin stress fibres were observed to spatially rearrange and mainly gather at the centre of the cells; subsequently, the fibres returned to a perimetral uniform distribution at 30 min post-exposure [134]. However, the founding mentioned above only provide preliminary insight into the changes in the cytoskeleton upon USMB exposure. The way in which the cytoskeleton responds to cavitation events and its role in the mechano-transduction to the intercellular junction proteins domain remain unclear.

1.4.3 Endocytosis stimulated by acoustic cavitation

Beside loosening cells junctions or membrane pore formation, the mechanical stress of oscillating MBs acting on the cellular membrane may result in membrane invagination leading to endocytosis [141, 142]. Endocytosis is an active transport—process independent from pore formation, controlled by several molecules and organelles that guide specific endocytic pathways, such as receptor-mediated endocytosis [143], phagocytosis or pinocytosis [144, 145]. Oscillating microbubbles upon US exposure may stimulate the aforementioned processes and contribute to the uptake of macromolecules that cannot be accommodated through pores [146]. In Figure 1.11 a schematic representation of USMB—induced endocytosis is reported. The mechanisms involving have been the subject of debate and have not been completely elucidated up till now. A first possible explanation, as reported by several studies [139, 147, 148], may be that oscillating MBs induce mechanical forces, *e.g.* micro-streaming, that lead to changes in cell membrane tension which is accompanied by cytoskeletal rearrangements and membrane bending[149] .

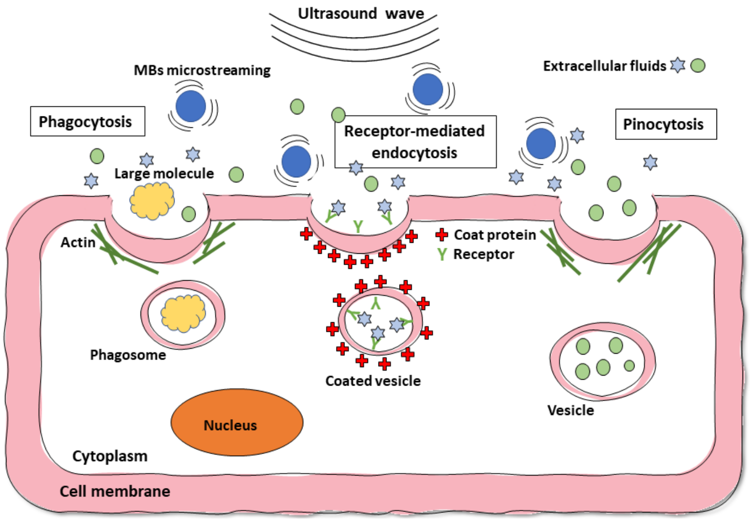

FIGURE 1.11: **Schematic representation of USMB-induced 3 different endocytosis pathways.** Phagocytosis is a specific form of endocytosis by which cells internalise large molecule or other cells. Receptor-mediated endocytosis refers to the process by which cells absorb metabolites, hormones or proteins by the inward bending of the plasma membrane. Pinocytosis, otherwise known as fluid endocytosis, is a mode of endocytosis in which small particles suspended in the extracellular fluid are brought into the cell through an invagination of the cellular membrane.

Whether the main route for internalization is by membrane pores or by endocytosis, depends on acoustic pressure and drug size, as identified by the localization of different conjugated dextran molecules size in primary VECs *in vitro* [150, 151]. After USMB exposure at 1 MHz, 0.22 MPa PNP small dextran molecules (range 4.4—70 kDa) are homogeneously distributed in the cytoplasm, implying uptake through membrane pores. Instead, above a certain size, *i.e.* 155−500 kDa, dextran macromolecules localise inside endocytic compartments [150]. De Cock et al. showed that the uptake route significantly depends also on the applied acoustic pressure [151]. Increasing the acoustic pressures up to 0.5 MPa at 1 MHz, the intracellular delivery of large fluorescent dextran (2 MDa) shifts from uptake by endocytosis to uptake via the membrane pores.

Exocytosis as a mechanism of resealing cavitation-perforated membrane

Initially, cell membrane wounds were believed to be repaired by resealing of the phospholipid bilayer, driven by the energetically favoured configuration [152]. However, cell membrane, supported by the cytoskeleton, creates a membrane tension which opposes to the spontaneous resealing. Under this consideration, only the repair of small pores ($< 2\ \mu$m in diameter) may be explained by self−sealing [153]. Later, has been demonstrated that C_a^{2+} influx, resulting from the physical disruption of the cellular membrane and the consequent pore formation, triggers exocytosis, a crucial process for membrane repair. More specifically, it consists in the recruitment of intracellular vesicles (lysosomes), to the site of injury [115, 116], which can fuse to form a "patch" and cover the membrane pores [154] as sketched in Figure 1.8. Schlicer et al. used TEM microscopy to observe blebs and patch formation at the perforation sites of sonoporated cells, which temporally correlated with a decrease in fluorescence of labelled intracellular vesicles [142]. These findings suggest that lysosomes trafficking is involved in pore resealing in response to elevated C_a^{2+} concentration. However, these early findings don't elucidate the spatiotemporal relationship between intracellular C_a^{2+} and exocytosis of vesicles in the resealing of the perforated membrane.

1.5 Microbubbles designed for drug delivery

As well as clinically approved as US contrast agents (UCAs) for diagnostic US application, MBs injected into the blood stream have been shown to enhance multiple types of US therapy in animal and clinical studies. UCAs typically have diameters of 1-10 μm. At room temperature (21°C) and pressure (1atm) the mean diameter is 2 μm, nevertheless, at physiological temperature (37°C) bubble may expand. To be useful clinically, UCAs must persist for enough time and must be sufficiently small to traverse the capillary bed of the lung without being destroyed and without posing any risk of causing an embolism.

The first generation of MBs was composed of air encapsulated by albumin (Albunex®) or galactose/palmitic acid shells (Levovist®) [155]. However, the stability of such air−filled MBs was less than ideal [156, 157]. They dissolved in the bloodstream within a few seconds after intravenous injection because of the high solubility of air in blood and their low resistance to arterial pressure gradients. To overcome limitations involved in the use of free gas MBs as contrast agents, therefore prolonging the stability and contrast enhancement in diagnostic imaging, a second generation of MBs were introduced. These were filled with heavy−weight hydrophobic gas, with lower solubility and lower diffusivity encapsulated by a biocompatible shell (*e.g.*, lipids, polymer) [158] (see Figure 1.14). All current commercially available UCAs use some sort of encapsulation to increase their persistence [159, 160].

There are two main groups identifying in the second generation of MBs. First are MBs filled with perfluorocarbon gases. These are inert gases, immiscible with water which can be injected intravenously if emulsified. Examples of this type are Definity®, Imagent® and Optison® [161, 162]. Definity® and Imagent® bubbles have a phospholipid shell, whereas Optison® has an Albumin shell. The second group are those filled with Sulphur Hexafluoride. A primary example of this type is SonoVue® bubbles which are also phospholipid coated [163]. It should be noted that although second generation contrast agents show an improved stability, they are very sensitive to their environment, especially to the temperature, gas saturation and preparation protocol [164]. Compared to the uncoated air bubble, the second generation of UCAs have different mechanical properties, leading to different dynamic behaviours as will be elucidate in Chaper 2, Sec. 2.2.2.

The simplest method for drug delivery application using US−activated MBs is to use co−administration injection of bubbles and drugs. They can be mixed in solution before the mixture is injected into the blood circulation or both constituents can be handled completely separately before two separate injections are performed. The latter strategy allows drugs to reach plasma peak levels before injecting MBs [165]. Indeed, MBs have a short circulation time and therefore need to be exposed to US within minutes after injection, otherwise they will be degraded and unable to induce bio−effects.

In parallel to the co−administration approach, the co−localization of drug and cavitation activity has also been investigated by preparing drug loaded MBs. To increase the selectivity of the therapy, MBs have been modified to function not only as cavitation nuclei, but also as drug delivery carriers [166]. The strategy is to encapsulate drugs into the bubble and then induce stable or transient cavitation only in the feeder vessels of the lesion, allowing for a high spatial control of drug release [167]. Besides, an additional advantage of loading MBs with therapeutics is that it can act as protective drug carrier avoid drugs degradation in biological fluids thus prolonging their half−life. On the other hand, the small size of a MB and its gaseous lumen restricts the space for drug loading. To improve loading efficiency the therapeutic agent can also be embedded on/in the outer surface of the bubble. For this purpose, several strategies have been used such as chemical conjugation or electrostatic adsorption [166, 167] (Figure 1.12A).

The choice for the best loading method depends mainly on the nature of the drug. For example, lipophilic drugs can be incorporated into the lipid monolayer shell of the bubble or dissolved in an oil pocket between the gas core and the bubble's shell [168] (Figure 1.12B−C).

An even more specific drug delivery approach can be obtained by conjugating a targeting ligand to the dug loaded MBs surface to facilitate accumulation of bubbles to the designated surface target (Figure 1.12D). As an example, VECs during pathological events, overexpress some membrane markers in irregular zones. These markers are thus the perfect candidates to bind the functionalized MBs [169], allowing to a selectively extravasation of the drug, upon US exposure, in the area where they are overexpressed.

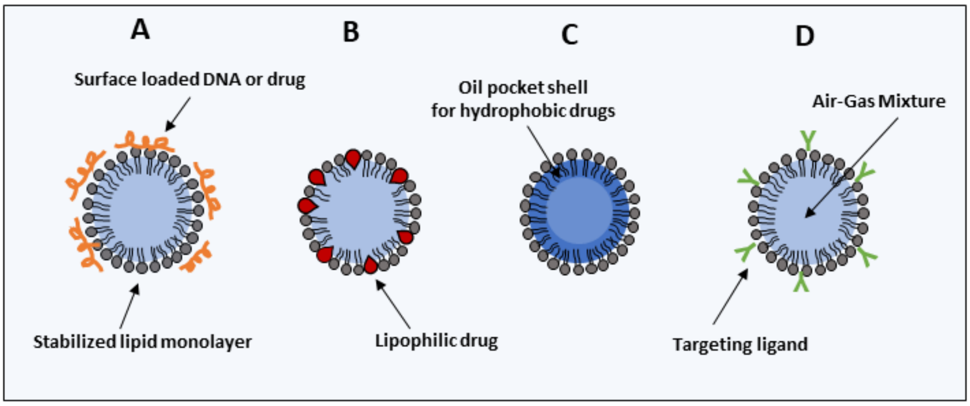

FIGURE 1.12: **Different options for drug loaded MBs.** The basic bubble design with heavy-weight hydrophobic gas core, stabilized by a lipid monolayer. **A.** MBs modified to function as drug carrier by attaching drugs to the surface using electrostatic attraction or chemical conjugation. **B.** Lipophilic drugs can be incorporated into the lipid monolayer shell of the bubble. **C.** An oil pocket can be thickened between the gas core and the bubble's shell allowing the hydrophobic drugs to be carried within it. **D.** Targeting ligands can be conjugated to the surface in order to facilitate MBs accumulation to the targeted tissue.

Functionalized MBs, as efficient drug carriers, are one of the most promising approaches in tumours therapy. However, targeted molecules expression does not differ that much between normal and tumour tissues, leading to poor treatment efficacy. A very difficult task is also to determine if the target is expressed enough to bind detectable amounts of the agent. In this scenario, providing an *in vitro* approach, able to reproduce the biological effect that cancer imposes on the vasculature, will be crucial in view of identifying a selective ligand−mediated targeting mechanism for improving MBs−cell contact. Thus, as explained in the following section, studying endothelium morphology in presence of either healthy or malignant tissues under controlled and physiological conditions will optimize targeting capability.

1.6 Microfluidics for advanced drug delivery system

Despite the potential of cavitation—enhanced drug delivery approach, *in vivo* animal models turned out to be extremely expensive, time—consuming and difficult to perform. An additional effort to improve drug delivery efficiency and understand the involved transport mechanism can be given by microfluidic systems. With their ability for precise handling and transport of small liquid quantities, microfluidics systems have emerged as a promising *in vitro* platform for designing advanced drug delivery system [170, 171]. Beside the capability to developing drug carriers able to enhance drug bioavailability and specificity test while reducing cytotoxicity [172–175], microfluidic devices may also be exploited to investigate on drug delivery mechanisms at the cellular level while performing analysis under physiological and precise reproducible conditions [176, 177].

In particular, the application of microfabrication techniques to tissue engineering allow to create "bioinspired devices" in order to replicate organs functions or physiologically relevant disease models [178–180].

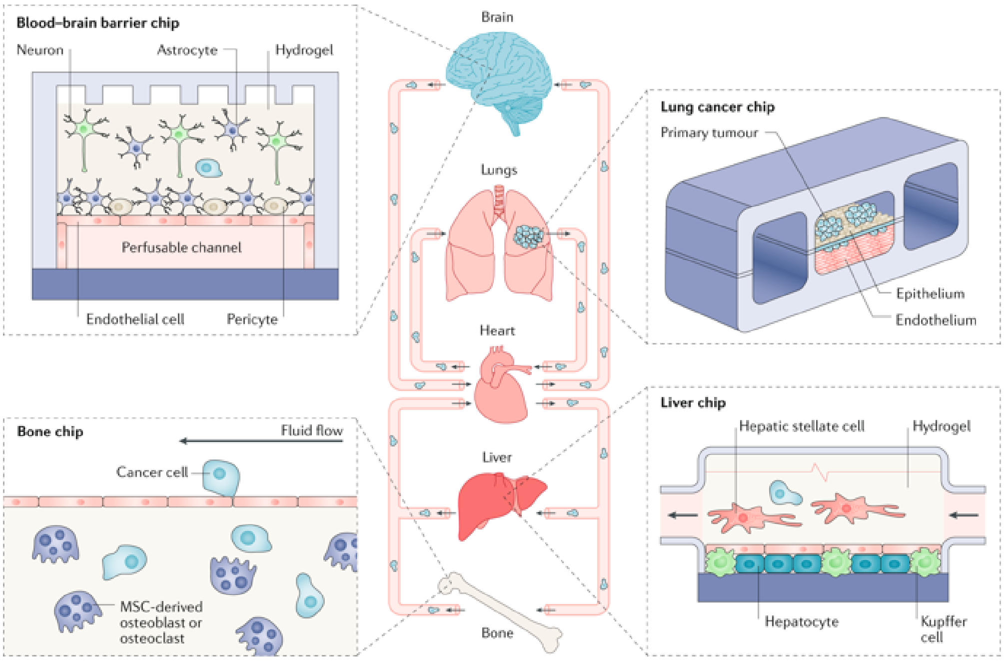

Figure 1.13: **Image taken from [181].**Modelling systemic metastasis in a body-on-chip.

The so−called organs−on−a−chip systems can be designed to incorporate the appropriate biophysical stimuli and can be exploited for high−throughput drug screening with better preclinical predictability. In this way cost and time for new drug development can in principle be saved, minimizing the risk for the patient [182] and partially avoiding ethical issues related to *in vivo* studies [183].

Among many microfluidic devices, recently designed to replicate complex biological micro−environment, a relevant example is the vasculature−on−a−chip. Considering that vasculature is indispensable in modeling any process that is circulation driven such as inflammatory responses [184], cardiovascular diseases [185], cancer intravasation [186] and extravasation [187], creating 3D *in vivo* like vasculature has always been an important research question in the engineering of tissue surrogates and disease-on-a-chip.

A crucial issue in mimicking vasculature systems is the reproduction of the mechanical stress acting on the endothelial barrier [188, 189]. Indeed, the VECs phenotype is established by the frictional forces generated by blood flow that induces functional cell responses through signalling molecules and/or cytoskeleton reorganisation [190, 191].

First *in vitro* approach, to replicate endothelium phenotype, have consisted in flow chambers with idealized geometry. Parallel plate flow chambers, for example, have been used to investigate the effect of flow conditions on vasculature through perfusion at low Reynolds number [192]. These flow chambers also allow for the quantification of particle adhesion, shear stress and VECs response [193, 194]. Although the idealized chambers structure can be exploited for an easy characterization of the flow−induced effects, the complex geometry and configuration found in *in vivo* microvasculature is not realistically reproduced. This simple setting lacks in correspondence with *in vivo* flow dynamics, cell and drug transport. As a first observation, flow chamber plates are usually designed with channels larger than capillary vessels (5-10 μm)[176]. Furthermore, the microvasculature is morphologically different in diseased tissues resulting in abnormalities and irregular structure. The presence of bifurcations, tortuous path or the variation of the cross-sectional areas are aspects that influence the local flow and the transport of cells or drugs to a targeted site.

Thanks to the many advantages microfluidics possess, tissue engineers have been employing microfluidics technology to mimic vasculature networks over the past two decades [195, 196]. With channels from a few to hundreds of microns in diameter, they are a convenient tool to mimic the geometry of microcirculation. Besides, in order to mimic complex microvascular networks including bifurcations and other physiologically realistic patterns, several microfluidic devices have been realized in Polydimethylsiloxane (PDMS) [197, 198]. PDMS is an affordable, flexible, optically transparent and easy to handle polymer that is also easy to bond to other surfaces [199]. It is compatible with biological assay since it is non−toxic to cells, impermeable to water while allow gas entrance, *e.g.* sufficient transfer of CO_2 to the cells. Flow in microfluidic devices can be also personalized to recapitulate the dynamic and fluidic microenvironment that cells experience *in vivo* including shear stresses. One successful example is an endothelialized microvasculature developed by Tsai et al., with branching channels (smallest diameter of 30 μm) emulating a postcapillary venule and used to study the effect of inflammatory cytokines on microvascular obstruction under perfusion of patient blood [200]. Apart from the simulation of vasculature morphology and hemodynamics, spatiotemporally controlled chemical gradients are also achievable by manipulating liquids of different chemical concentrations in parallel microfluidic channels. Moroever, heterotypic cells can be subsequently seeded and co-cultured in the same microfluidic chip. Such co-culture capability offers significant convenience for researchers interested in cell–cell interactions [201] happening in tumor-immune response [202–204] and vasculogenesis [205].

To summarize, microfluidics provide unique microenvironmental attributes such as lumen architecture, flow and spatial distribution of cells/particles that are difficult to define using other 3D culture technologies.

Over the decade, various techniques have been established to pattern microfluidic networks for vasculature generation. The most common and well established fabrication method is photolithographic moulding of PDMS. Microvessels of rectangular cross-section can be easily fabricated to be later populated by human vascular endothelial cells [206]. However, the diameter of these microvessels is limited by the resolution of soft lithography. Most microvessels patterned via soft lithography are able to mimic arteries and veins of more than 100 μm in diameter [207–209], but are far from reaching the geometry of very fine capillaries (10–20 μm) [210]. In addition, most of the lithography-moulded microvessels are made of synthetic polymers including PDMS and are lined with a single layer of vascular endothelial cells. Such synthetic and monolayer structures are unable to mimic the natural architecture of blood vessel walls, which usually consist of stacked layers of endothelial cells, a basement membrane, pericytes, smooth muscle cells and fibroblasts.

To mimic such complex architecture, alternative techniques have been developed to pattern vasculature inside ECM hydrogels. For instance, Baker et al. injection-moulded gelatin, a natural thermoplastic protein, into a microvasculature construct and embedded it within collagen hydrogel [211]. The gelatin was then melted at 37°C and left open channels inside the collagen gel. The vasculature reached a diameter of less than 100 μm and the cros section was quasi-cylindrical. A similar strategy was developed in the same group, where 3D printed lattices made of sacrificial carbohydrate glass were used to pattern vasculature inside ECM [49]. Alternatively, viscous finger patterning [212], removable nitinol rods [213] and laser beams [214] were also used to pattern cylindrical microchannels inside ECM gels. For example, Hasan et al. inserted concentric needles of varying diameters into a microchannel and subsequently loaded cell laden gelatin methacryloyl (GelMA) hydrogel into the annular interneedle space. The use of concentric needles was to create multilayered cylindrical vascular walls consisting of endothelial, smooth muscle and fibroblast layers [**?**]. Using these aforementioned microfluidic fabrication methods, microchannel networks in the hundreds of micron scale can be patterned within synthetic or natural polymeric materials and be lined with vascular endothelial cells. This microvessel generation technique can be termed as 'prevascularization technique' [215]. However, to replicate the complex networks of fine capillaries, angiogenesis-assisted vascularization is a more appropriate strategy. Briefly, vascular endothelial cells are seeded inside

ECM hydrogels with angiogenic stimuli such as shear stress and vascular endothelial growth factor (VEGF) [201], and are cultured for days to form spontaneously interconnected capillary networks. The main limitation of the angiogenesis technique is that the system often requires a set of predefined culture conditions, which restrict system tunability and hemodynamic controllability. It is of note that individual [216] or combined [217] strategies can be employed to address various research questions. To improve physiological relevance, important directions for the future development of biomimetic vasculature include: improving coculture complexity, refining vasculature dimension and enhancing fluidic control.

Considering the incredible interest in microfluidic devices as *in vitro* systems and functionalized MBs as tools for drug delivery, there is an unexpected lack of studies where these two elements are combined. Several works focused on the bubble dynamics under given US fields, as well as their disruption thresholds [218] or their binding to specific markers [95]. However, the devices used to confine MBs do not contain living cells: they consist only of microfluidic chambers whose surfaces are, in some cases, coated with target−proteins.

In the few works where US−activated MBs interact with living cells [134, 141, 142, 219], the VECs condition were extremely far from the physiological conditions found *in vivo*. Current *in vitro* models of the endothelial barrier comprise permeable membranes covered with an endothelial monolayer and immersed in liquid tanks where MBs are injected and irradiated by US [62, 220]. Alternatively, tissue phantom models consisting of an agarose gel tissue platform and optimized to hold the bubble suspension are used to study tissue−like response to USMB irradiation [221]. While these devices have significantly contributed to our understanding of cavitation in tissue, they are limited by the lack of physiological flow conditions and appropriate vessel geometry which, as explain above, are crucial to achieve a functional endothelium.

It is worth mentioning the study carried out by Yooniee C. Park and collaborators [222] who recreated in a microfluidic device the spontaneous formation of blood microvessels for the visualization of microbubble and ultrasound-dependent drug delivery across microvasculature. However, since the vessels show a high variable range of sizes, controlled quantitative and statistically valid results, regarding permeability for example, are difficult to obtain.

Recently, a relatively simple and effective commercially available device has been developed as a model of microvasculature−on−chip [223, 224]. The microfluidic network has been optimised with the main intent to investigate on BBB permeability and therapeutics screening. The favourable features of this model are the real−time measurement and visualisation capability, the three−dimensional channels that good match the size of micro−vessel, the correct perfusion rate at physiological shear stress intensity ($1 - 12 dyne/cm^2$) [188, 225, 226] and the biochemical interactions between different cultured tissues. In particular, in [223] the neonatal stage BBB has been reproduced *in vitro* by co−culturing rat brain endothelial cells (RBEC) and astrocytes in different compartments, kept in communication through a porous interface. The two distinct cell cultures, communicating through a bio−interface, offer the opportunity to investigate the cell−cell interactions that occur between different tissues, *e.g.* immune system and tumour.

In the present work, we use this system to characterize and quantitatively understand the mechanism behind cavitation assisted drug delivery, combining the vessel−on−a−chip with controlled MBs injection and US irradiation. Our bioinspired system is proposed to provide a significant advancement of the state of the art in this field with novel biophysical insights into the mechanism behind the endothelial permeabilization upon USMB exposure and in particular into the destabilization of inter−endothelial junctions that may facilitate the diffusion of a macromolecule through biological barriers.

1.7 Goal of the thesis

The goal of this thesis aims to develop and characterized a microfluidic device mimicking a capillary vessel, adapting the high−fidelity biomimetic device proposed by [223] to reproduce the three−dimensional morphology, size and flow characteristic of *in vivo* micro-vasculatures, as a platform to quantitatively understand

and quantify the morphological cellular changes upon cavitation. Human Umbilical Vein Endothelial Cells (HUVECs) are cultured to form a complete lumen lining two independent vascular channels (VCs) encircling an inner tissue compartment (TC). VCs and TC are connected through a membrane characterized of micrometres size pores. The important role of shear stresses exerted on the innermost surface of the cell−covered microchannels and induced by the dynamic cell culture condition is firstly investigate with immunofluorescence (IF) microscopy. Morphological changes of cell-cell junctions and actin filaments proteins are then observed and analysed in order to asses endothelium integrity and functionality. Measurements of permeability are then performed to quantify the tightness of the artificial endothelial barrier by injecting a fluorescence dye into the VC and measuring its diffusion across the artificial barrier over time. This is made with a time-lapse acquisition under a confocal microscope operated in epifluorescence mode. Once the feasible and reproducible bioinspired platform is obtained, it is used in combination with USMB technology in order to study and characterize the physical and biological mechanism behind junction opening and cavitation-enhanced endothelial permeability. MBs are injected into the VC and irradiated by low intensity US to force stable acoustic cavitation. The efficacy of US at different intensity, both with and without MBs, is monitored and quantified in a highly reproducible manner at different stage of the experiment: i) before USMB exposure, ii) during MBs driven by US exposure, iii) after a certain period of time for endothelial layer recovery. The cavitation-induced mechanical stress acts on the endothelial layer forming inter-endothelial gaps that are indeed detected within different time windows with IF microscopy. Measurements of the enhanced endothelial permeability are also carried out with a dedicated acoustic/optical setup in presence of US, either with or without activated MBs.

Before presenting the experimental methods adopted in this study and discussing the obtained results the physics of US-driven microbubbles is briefly introduced to provide the theoretical and mathematical tools in order to better understand the phenomena of cavitation in blood vessels used as a novel drug delivery strategy.

Chapter 2

Cavitation: the physics

A relatively recent and novel application in drug delivery takes advantage of the remarkable ability of US to produce cavitation activity, that is the oscillatory motion of MBs within a liquid. This approach has been reported to improve spatially confined delivery of drugs to target tissues, while reducing systemic dose and toxicity. The physical basis behind the enhanced drug delivery are the fluid mechanical stresses generated on vasculature, through which drugs are distributed, induced by US−triggered oscillations of MBs.

In 1982, Apfel was the first to discuss the possibility of using cavitation in biomedical application. He related and quantified the parameters used in describing cavitational activity with those parameters most often associated with equipment used for biomedical applications of US [227].

In his studies, cavitation dynamics was divided in two categories depending on different types of sound fields: small to moderate amplitude oscillations and large amplitude bubble motion in which the bubble grows in one cycle by an amount equal to or greater than the radius. In the latter case, also a short pulse of US is sufficient to cause biological damages if the bubble has the time to grow enough to collapse.

Whether MB collapse occurs or not, for a free−floating spherical nucleus of known gas content in a given liquid, depends primarily on the acoustic pressure amplitude, the acoustic frequency, and the size of the nucleus. If the nucleus is too small, then surface tension forces prevents the initial sudden growth, and inertial cavitation does not occur. If it is too large, then the bubble may grow, but too slowly to concentrate the energy sufficiently on collapse to generate bioeffects on an adjacent cell. There is therefore a critical size range in which, for a given sound field, the initial size of the bubble must fall in order to provide inertial cavitation [228, 229]. The lower the frequency, the wider this range. In 1989, R. Apfel and C. Holland introduced for the first time the cavitation threshold, as the minimum pressure required to induce bubble growth and subsequent adiabatic collapse [229].

This is shown in Figure 2.1A−B where the transition threshold between inertial

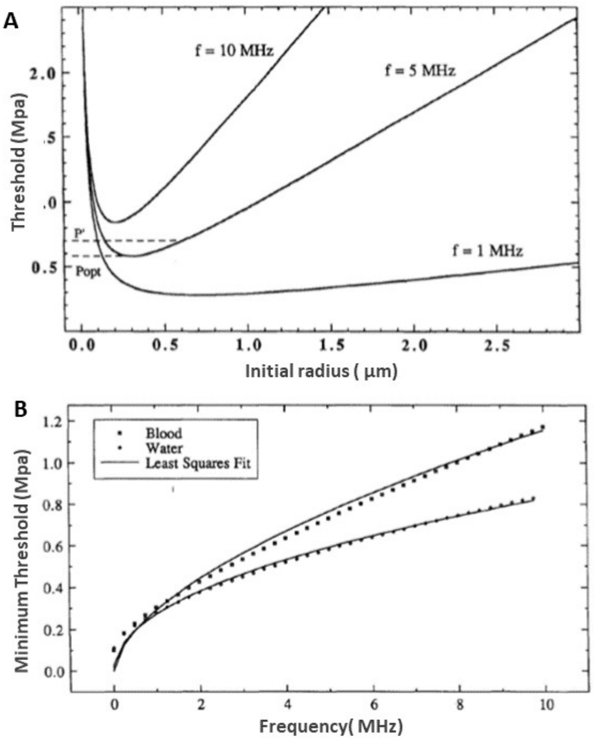

Figure 2.1: **Transition threshold between inertial and non−inertial (stable) cavitation.** Curves are taken from the work of C. Holland and R. Apfel reported in [229]. **A.** Plot of the cavitation threshold in water as a function of initial nucleus radius for three insonification frequencies. **A.** Curve of minimum cavitation threshold, P_{opt}, in water and in blood assuming all nuclei sizes are present. Solid lines represent a least squares fit to the data of the form of Equation *2.1.*

and non−inertial (stable) cavitation is plotted, based on Apfel and Holland calculation. It illustrates that the acoustic pressure amplitude required for a bubble to undergo inertial cavitation is dependent with the initial radius of that bubble. In particular, it was found that the minimum pressure needed for bubble to expand increases not only with decreasing bubble size because of surface tensions but also with increasing size due to inertial and viscous effects, as shown in Figure 2.1A.

The pressure profile shows thus a minimum, named P_{opt}, for a certain bubble size whose dependence from the insonification frequency is given by:

$$P_{opt} = cf \tag{2.1}$$

where P_{opt} is in MPa, f is the central frequency of the US wave in MHz and c is a constant that equals 0.13 for blood and 0.06 for water. A curve of P_{opt} vs f is reported in Figure 2.1B.

The theory that yields to the thresholds of pressure and frequency were found with the assumption of short pulse (a few acoustic cycles), isothermal growth, adiabatic collapse and finally incompressible fluid [230].

The theory of Apfel and Holland has given rise to a measure called the "mechanical index (MI)" which can be used to indicate the likelihood of exceeding the threshold required to bubble cavitation.

For a given sound field in a liquid, the MI can be defined as:

$$MI = \frac{PNP[MPa]}{\sqrt{f}[MHz]} \tag{2.2}$$

where PNP is the Peak Negative Pressure of the US wave (MPa), reduced by 0.3 dB $cm(Hz)^{-1}$ to account for the difference between in−water and in−tissue acoustic attenuation and $\sqrt{f}$ is the central frequency of the pressure wave.

The mechanical index is also a valuable number used to estimate the intensity of cavitation bio−effects. It combines the information on amplitude and frequency such that, below a threshold (MI<1.9, the upper limit indicated in FDA recommendations as potentially hazardous [231]) direct tissue damage by thermal and mechanical loads are prevented [232].

At low mechanical index (*i.e.* MI<0.1), MBs oscillate linearly and scatter the acoustic signal at excitation frequency. Increasing the MI (0.1<MI<0.5) stable cavitation still persists but bubbles response become non−linear. In this regime bubbles significantly displace the surrounding liquid inducing acoustic microstreaming (previously introduced in Chapter 1, Sec. 1.3.1) which pattern depends on the bubble oscillation mode and primarily varies with the applied frequency. The extremely high viscous shear stress near the surface of the bubble due to the creation of circulating eddies around it, may induce shear stresses all around the cellular membrane.

At higher MI (0.5<MI<1.9), inertial cavitation occurs usually accompanied by shock waves, micro−jet and free radical generation. The combination of these effects is usually correlated with cells membrane perforation and increased vascular permeability [233], as explained in Chapter 1, sec. 1.4. However, it has been shown that also cavitation at low MI can increase cells−membrane and blood vessel wall permeability [234]. The use of stable rather than inertial cavitation could be successful in order to achieve endothelium permeability enhancement avoiding or reducing irreversible damage to blood vessels and surrounding cells.

Even if a brief summary of cavitation mechanisms has been already given in Chapter 1, Sec.1.3, this chapter will be devoted to a short introduction to the physics of bubble dynamics. The theoretical tools and the physical principles behind cavitation and US−driven MBs are then briefly recalled, selecting the important aspects and parameters used for drug delivery applications. Starting from a free water/air interface MB at equilibrium in a quiet liquid we then observe its dynamic response if the equilibrium condition is perturbed by an acoustic pressure wave, finally considering also a MB coated by a stabilizing shell.

Bubble translation due to the acoustic radiation force, called primary Bjerkness force and the dynamic interaction with neighbouring bubbles, provoked by the Secondary Bjerkness force, are also mentioned.

2.1 Quiet free gas bubble

2.1.1 Surface tension

Before getting into the details of bubble cavitation theory, we will mention the forces at play for a quiet spherical bubble, when $R_b = 0$ and $R_b = R_{b,0}$, in an infinite volume of liquid at ambient condition with constant and uniform p_0 , T_0.

Increasing the interface's area between two media requires energy in order to bring molecules from the bulk to the interface. Without a compensating force, an interface therefore has a natural tendency to decrease. In the case of the bubble, the compensating force is an overpressure in the bubble, known as Laplace tension:

$$p_b = p_0 + \frac{2\sigma}{R_{b,0}} \tag{2.3}$$

where p_0 is the liquid ambient pressure, $R_{b,0}$ is the bubble radius and σ is the surface tension. This overpressure is worthless for large bubble but increases when $R_{b,0}$ approaches the value $\frac{2\sigma}{p_0}$ from above. For instance, for an air bubble in water at atmospheric pressure ($\sigma = 0.072Nm^{-1}$, $p_0 = 101$ kPa), $\frac{2\sigma}{p_0}$ is 1.45 μm so that the effect of surface tension becomes important in this range of radii. This is precisely the order of magnitude of the bubbles involved in cavitation, so that one can suspect that surface tension will play an important role.

2.1.2 Bubble ambient radius

We consider a bubble containing a given mass m_g of incondensable gas and liquid's vapour, in equilibrium with the latter at T_0, so that the partial pressure of vapour is the equilibrium saturation pressure $p_{v,eq}(T_0)$. The pressure p_b inside the bubble is then made of two contributions: the vapour and the gas pressure, respectively $p_{v,eq}(T_0)$ and $p_{g,eq}$. We seek the radius $R_{b,0}$ of this bubble in mechanical equilibrium. Assuming the gas inside the bubbles behaves ideally, therefore using the law of perfect gases to express $p_{g,eq}$, the liquid pressure is can written as:

$$p_0 = p_{v,eq}(T_0) + \frac{m_g}{M_g}\frac{\mathbf{R}T_0}{\frac{4}{3}\pi R_{b,0}^3} - \frac{2\sigma}{R_{b,0}} \tag{2.4}$$

where $\mathbf{R}$ is the universal constant of gas and M_g the molar mass of the incondensable gas in the bubble. The solution of this cubic equation yields the bubble ambient radius $R_{b,0}$. Simplifications of the equation are possible, neglecting $p_{v,eq}(T_0)$ if $T_0 \ll T_{boiling}$ as well as the surface tension term for $R_{b,0} \gg \frac{2\sigma}{R_{b,0}}$. However, any variation in the liquid pressure, *e.g.* due to the application of an external sound field, will therefore result in a change of the gas pressure inside the bubble. Consequently, a corresponding variation in m_g, and/or T and/or R, *i.e.* the mass, temperature or volume of the bubble will occur.

2.1.3 Mechanical Stability: The Blake Threshold

Equation *2.4* gives the radius of a bubble in mechanical equilibrium for a given liquid ambient pressure p_0. We consider now a small quasi−static perturbation in the size of the bubble from $R_b = R_{b,0}$ to $R_b = R_{b,0}(1+\epsilon)$ with $\epsilon \ll 1$ due to a decrease of liquid pressure to $p = p_0 - p_a$. Two cases can be distinguished, leading completely different bubble response: (i) the partial pressure of the gas remains the same at $p_{g,eq}$, (ii) the mass of gas in the bubble and its temperature, T_b, remain the same.

The first case is possible only if the perturbation acting on the bubble is so slow that the mass has the time to diffuse in the liquid. As a result, the partial pressure of gas is maintained at the value fixed by the concentration of gas dissolved in the liquid and the bubble grows. The timescales associated with both mass and heat transfer are very slow compared with the length of a typical US pulse (1-2 μs). Therefore, if the perturbation is generated over a short length of time, gas diffusion cannot take place. This results in the second case, much more attractive for the scientific community since nearly all practical engineering situations or technological applications involve pressure variations whose characteristic timescale is much smaller than the one of mass diffusion. In such situation, the bubble volume can easily change, altering the liquid pressure p_0. The magnitude of the bubble wall shift will be determined primarily by the initial radius of the microbubble $R_{b,0}$ and by the amplitude of the applied pressure.

Assuming a polytropic transformation for the gas, the evolution of R can be obtained implicitly by

$$p_{,eq}(T_0) + (p_0 - p_{v,eq}(T_0) + \frac{2\sigma}{R_{b,0}})(\frac{R_{b,0}}{R})^{3\gamma} - \frac{2\sigma}{R} = p_0 - p_a \tag{2.5}$$

where γ is the polytropic constant for the gas evolution (from 1 for isothermal processes to 1.4 for adiabatic processes). Figure 2.2 is obtained by using equation

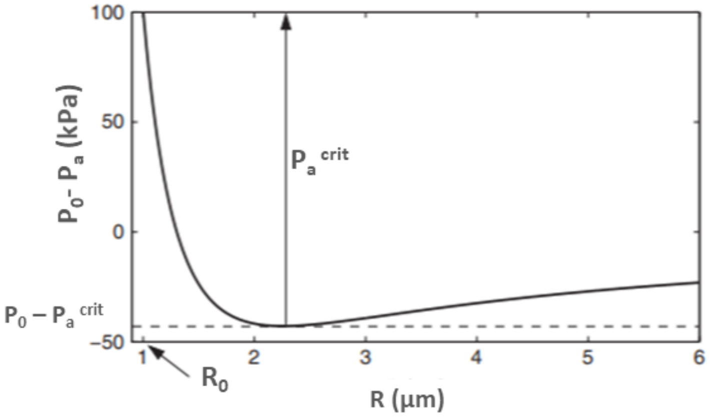

FIGURE 2.2: The curve is taken from the work of Louisnard et al. reported in [235]. It represents the evolution of the bubble equilibrium radius R when the liquid pressure $p_0 - p_a$ is decreased, for a 1-μm bubble in ambient conditions

2.5 and it shows the variation of the equilibrium radius $R_{b,0}$ as a function of the liquid pressure $p = p_0 - p_a$.

For bubbles with $R_{b,0}$ below a critical value and liquid pressures p larger than a critical threshold, a new equilibrium for the bubble is reached, so that it will be smaller in size but stable. Likewise, if p is decreased the bubble will become larger but again stable. On the other hand, if the external pressure is decreased to a value smaller that $p_0 - p_a^{crit}$, there is no possible stable equilibrium radius R. Beyond this pressure limits, surface tension cannot counteract the liquid pressure reduction and the bubble exists in an unstable condition. In this regime, the liquid starts to flow outward and any slight decrease in p_0 will result in explosive cavitation expansion regardless of whether p_0 is further decreased or not.

The model that predicts the thresholds for which a controlled bubble growth turns into a transient dynamic was developed by Blake and the critical pressure and radius took his name: Blake radius R_B and Blake pressure P_B [236, 237]. The Blake values are extremely sensitive to the mass of gas contained in the bubble. The larger the amount of gas molecules, the smaller the critical radius R_B and the higher the critical liquid pressure P_B.

To obtain the Blake pressure, is assumed that $p_{v,eq}(T_0)$ can be ignored and that surface tension dominates in the quasistatic regime which amounts to $p_0 \ll \dfrac{2\sigma}{R_0}$.

Under these approximations the Blake threshold pressure is conventionally defined as:

$$P_B = p_0 + 0.77\frac{\sigma}{R_{b,0}} \tag{2.6}$$

The present treatment can be used only to predict the onset of the explosive bubble growth without any description of the subsequent bubble wall evolution. When the pressure changes experienced by the bubble are no longer quasistatic (*i.e.* acoustic field in a liquid), a more detailed analysis taking into consideration the bubble dynamics and acoustic forcing frequency must be performed.

2.2 The forced spherical single bubble

When a bubble, surrounded by liquid, is subjected to the oscillating pressure waves of an acoustic field, it reacts by undergoing a volume oscillation. The liquid next to the bubble wall will also be set into motion and so influences the bubble dynamics. Thus, to fully describe the response of a MBs to US excitation it is necessary to consider the inertia of the surrounding liquid. The following section derives the theoretical equations that describes this motion starting from the governing equation of spherical bubble dynamics in an incompressible medium. For a Newtonian fluid, the governing equation reduces to the famous Rayleigh˘Plesset equation [238], a remarkable example of a solution of the Navier˘Stokes equation in spherical coordinates, which characterizes the radius of an oscillating bubble in a time varying pressure field.

2.2.1 The Rayleigh-Plesset Equation for a free gas bubble

In order to examine the dynamics of the bubble, it's necessary to develop an approximate non−linear equation of motion, starting from the conservation equations for an incompressible Newtonian fluid:

$$\rho_L[\frac{\partial u}{\partial t} + (\mathbf{u}\cdot\nabla)\mathbf{u}] = -\nabla p + \mu_L\nabla^2\mathbf{u} \tag{2.7}$$

$$\nabla \cdot \mathbf{u} = 0 \tag{2.8}$$

where $\mathbf{u}$ is the liquid velocity, ρ_L the liquid density and μ_L its viscosity.

Moving away from the equilibrium conditions, described in Sec.2.1, due to the superimposition of the acoustic pressure $p_a(t) = p_a sin(\omega t)$, results in a liquid pressure at a point remote from the bubble equal to:

$$p_\infty(t) = p_0 + p_a(t) \tag{2.9}$$

where p_0 is the hydrostatic pressure at equilibrium. Consequently, the bubble radius will change. A schematically view is given by Figure 2.3.

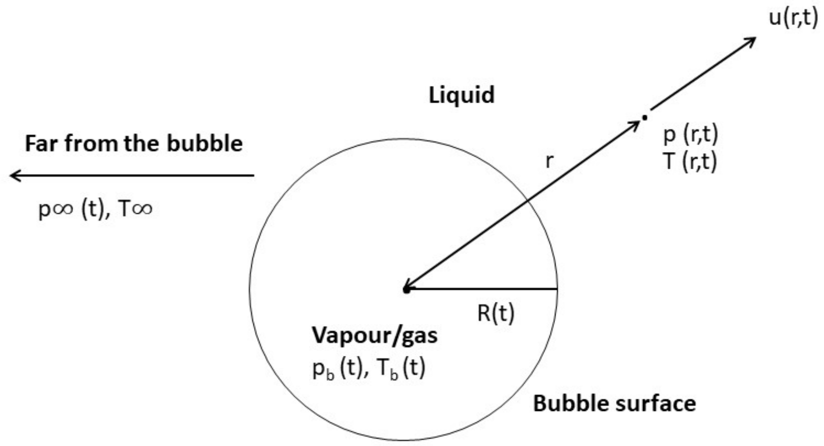

FIGURE 2.3: **Schematic of a spherical bubble in an infinite liquid.**

As indicated in Figure 2.3 radial position within the liquid is denoted by the distance r from the centre of the bubble.

To simplify the problem, some assumptions about the system are made. Firstly, the liquid density ρ_L and dynamic viscosity μ_L are assumed constant and uniform. Bubble interface deformations are considered only spherical and the mass transport across the interface is neglected. Therefore, if the liquid surrounding the bubble is incompressible, then as the volume of the bubble increases, the volume of the liquid around the bubble will have to increase the same amount and at the same rate. Under these conditions, the mass conservation equation for liquid in spherical coordinates becomes:

$$r^2 u(r,t) = R^2(t)\dot{R}(t) \tag{2.10}$$

$$u(r,t) = \frac{R^2(t)}{r^2}\dot{R}(t) \tag{2.11}$$

where $u(r,t)$ is the velocity of liquid in r at instant t and $u(R,t) = \dot{R}(t)$ is the velocity of the liquid at the bubble interface. If the bubble remains spherical all the time, it's possible to rewrite the equation of motion *2.7* in the r direction as follows

$$\rho_L[\frac{\partial u}{\partial t} + \mathbf{u}\frac{\partial u}{\partial r}] = -\frac{\partial p}{\partial t} + \mu_L[\frac{1}{r^2}\frac{\partial}{\partial r}(r^2\frac{\partial u}{\partial r}) - \frac{2u}{r}] \tag{2.12}$$

Replacing equation *2.11* in equation *2.12* and integrating from $r = R$ to $r \to \infty$ it turns into:

$$\frac{p(R) - p_\infty}{\rho_L} = R\ddot{R} + \frac{3}{2}\dot{R}^2 \tag{2.13}$$

This simplified equation of motion was developed by Besant in 1859 [239] and equates the acceleration of the bubble wall to the pressure balance across it.

To complete the analysis, dynamic boundary conditions are necessary in order to include the effects of viscosity and surface tension. In this regard, considering a control volume of a small, infinitely thin lamina containing a segment of interface (Figure 2.4), the forces at play are the bubble pressure pointing outward p_b and the liquid pressure at the interface $p(R)$, the surface tension $\frac{2\sigma}{R}$ and the viscous terms $4\mu_L\frac{\dot{R}}{R}$, pointing inward.

With no mass transport across the interface and refer to equation *2.3* the net force acting on this volume per unit area must be zero

$$p(R) = p_b - 4\mu_L\frac{\dot{R}}{R} - \frac{2\sigma}{R} \tag{2.14}$$

Substituting *2.16* in *2.13* the equation of motion for the spherical bubble is finally obtain:

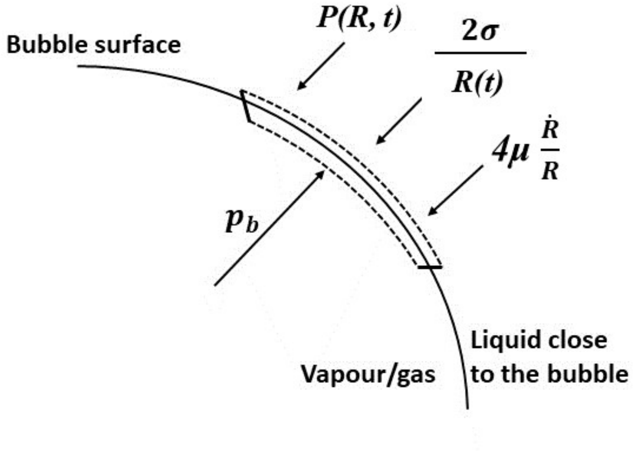

Figure 2.4: **Portion of the spherical bubble surface.**

$$\frac{p(R)-p_\infty}{\rho_L} = R\ddot{R} + \frac{3}{2}\dot{R}^2 + 4\nu_L\frac{\dot{R}}{R} + \frac{2\sigma}{\rho_L R} \tag{2.15}$$

where $\nu_L = \dfrac{\mu_L}{\rho_L}$ is the cinematic viscosity.

The resulting equation is commonly referred to as the Rayleigh−Plesset equation [240–242] although Lauterborn [243] suggested it should be more correctly termed the Rayleigh−Plesset−Noltingk−Neppiras−Poritsky (RPNNP) equation. It is a second order, nonlinear differential equation describing the response of a spherical ideal gas bubble to a time−varying pressure field.

Considering this frame, we seek now the natural frequency of the bubble ω_0 using the Rayleigh−Plesset equation. For sufficiently small amplitudes, the non-linear contribution -the second term in Equation *2.15*- can be dropped, and the equation of bubbles oscillation becomes that of a linear forced oscillator, *i.e.* if the bubble is driven sinusoidally, it will respond sinusoidally (Figure 2.5A). The bubble contracts and expands spherically and stably around its equilibrium radius as it experiences the compression and rarefaction cycles of a passing acoustic wave. The maximum expansion typically does not exceed twice the equilibrium radius and occurs when bubble is exposed at its resonance frequency. In such condition, the bubble behaves as a spring and mass system in simple harmonic motion. The stiffness is provided by the vapour and/or gas within the bubble that upon compression provide a force that resists the compression. The inertia is mainly provided by the liquid surrounding the bubble that moves with the bubble wall. The oscillating system will then have a natural resonant frequency ω_0 which depends on the equilibrium radius of the bubble.

By taking $R_b = R_{b,0}(1+\epsilon)$ with $\epsilon \ll 1$, equation*2.15* reduces to:

$$\ddot{\epsilon} + b\dot{\epsilon} + \omega_0^2\epsilon = \frac{p_a(t)}{\rho R_0^2} \tag{2.16}$$

Where b is the mechanical resistance related to the dissipation.

Substituting $\epsilon(t) = \epsilon e^{i\omega_0 t}$, that confers an oscillatory dynamic to the bubble radius, yields to the natural frequency:

$$\omega_0 = \sqrt{\frac{1}{\rho_L R_{b,0}^2}[3\gamma(p_0 + \frac{2\sigma}{R_{b,0}}) - \frac{2\sigma}{R_{b,0}}]} \tag{2.17}$$

From Equation *2.17*, the Minnaert frequency is found for large bubble where surface tension effects can be neglected:

$$\omega_0 = \frac{1}{\rho_L R_{b,0}}\sqrt{\frac{3\gamma p_0}{\rho_L}} \tag{2.18}$$

M. Minneart was the first to hypothesize radial oscillations of large air bubbles within the liquid to explain the sound emitted when liquid water is in motion [244]. He found the spherical air bubble resonant frequency in water at ambient condition to be inversely proportional to its radius, according to the relation $f_r\dot{R}_(0) \cong 3ms^{-1}$. For f=20 kHz, the resonant radius is 150 μm, while for f = 1MHz, it drops down to 3 μm. This is an approximate result that assumed the liquid to be incompressible and inviscid, moreover it neglects surface tension making the formula less accurate for smaller bubbles.

With increasing US excitation pressure, the amplitude of the bubble oscillations increases and becomes nonlinear, with the bubble expanding more than it contracts over each cycle (Figure 2.5B). Equation *2.18* is then no longer strictly valid and the frequency at which the amplitude of oscillation is maximized becomes dependent on pressure [245, 246]. Under these conditions the bubble will still undergo repetitive oscillations, but periodicity may only be observed over several cycles [247].

Eventually with increasing pressure the periodic nature of the oscillations is lost (Figure 2.5C). These may become chaotic and the bubbles undergo violent collapse, releasing a shock wave and often fragmenting into smaller bubbles. In this regime, the motion of the bubble is highly nonlinear, and the collapse is dominated by the inertia of the surrounding liquid medium.

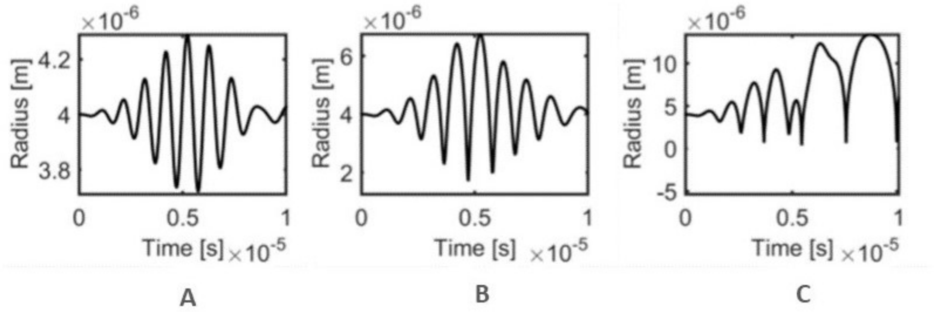

FIGURE 2.5: **Image taken from [248]**. Examples of various oscillation modes: **A.**Linear **B.**Nonlinear **C.**Inertial collapse.

2.2.2 Coated microbubbles dynamics

A gas bubble will never be completely stable due to the pressure acting on its surface from the interfacial tension and the gas concentration gradient between the bubble core and the surrounding liquid, therefore it will naturally tend to dissolve in water as described by Epstein-Plesset model [249]:

$$\dot{R} = -DHRT \frac{1 - s + 2\dfrac{m_w \gamma}{\rho K_0 T R}}{1 + 2\dfrac{m_w \gamma}{\rho K_0 T R}} \frac{1}{R} \tag{2.19}$$

where D is the gas diffusivity, H Henry's constant for the gas and **R** the ideal gas constant and m_w the molecular weight of the gas inside the bubble. The dissolution rate depends on the gas saturation fraction of the liquid, $s = \dfrac{C}{C_s}$, that is the ratio of dissolved gas to saturation concentration.

Ordinary gas/water interfaces have a considerable surface tension, implying that, according to Young-Laplace equation *2.3*, the pressure inside micron sized bubbles may raise to large values. Since air is easily soluble in biological liquids, ordinary bubbles, are fast to dissolve, unless properly stabilised. Stability may be increased with a larger saturation fraction, a smaller surface tension ($\sigma \rightarrow 0$), and/or smaller gas diffusivity and solubility. Since saturation level cannot be modified, bubble lifetime is enhanced by decreasing surface tension through suitable coating and by reducing gas diffusivity and solubility using large molecular weight inert species.

As described in Chapter 1, Sec.1.5, all commercially MBs used for biomedical applications are normally encapsulated for different purposes, thus the effect of the coating must be considered in any model describing their behaviour. Typically, they consist of heavy molecular weight inert gas, such as SF_6, C_3F_8 or C_4F_10, coated with a lipid, polymer, sugar or protein layer.

Encapsulated MBs were first modelled by De Jong et al. [250]. The model was based on equation *2.15* and was developed to describe the oscillations of albumin coated bubble such as Albunex®. In his equation, the effect of the encapsulation was described in terms of shell elasticity and shell friction parameters, demonstrating experimentally that the shell surrounding Albunex® behaves as a layer of elastic solids [251]. Some years later, Church [252] derived a model for a MB coated with a viscoelastic solid shell of finite thickness and it was later shown by Hoff et al. that de Jong et al.'s model was equivalent to Church's model in the limit of an infinitely small shell thickness [253]. Since then many models have been defined to investigate the influence of the coating shell on the bubble's vibration [254–256].

Recently, Marmottant et al. [257] has proposed a new model for phospholipid monolayer coated bubbles going beyond the assumption of small bubble surface deformations adopted in other models. In practice, insonifying MBs produces oscillations with large variations in surface area. Referring to Langmuir-Blodgett measurements [258] for dynamic surface tension of a flat monolayers, Marmottant et al. formulated a new concentration dependant surface tension. His model proposed a variable effective surface tension at the bubble wall that varies along three regimes. These regimes depend on the bubble area, $A = 4\pi R^2$, with R the bubble radius (Figure 2.6).

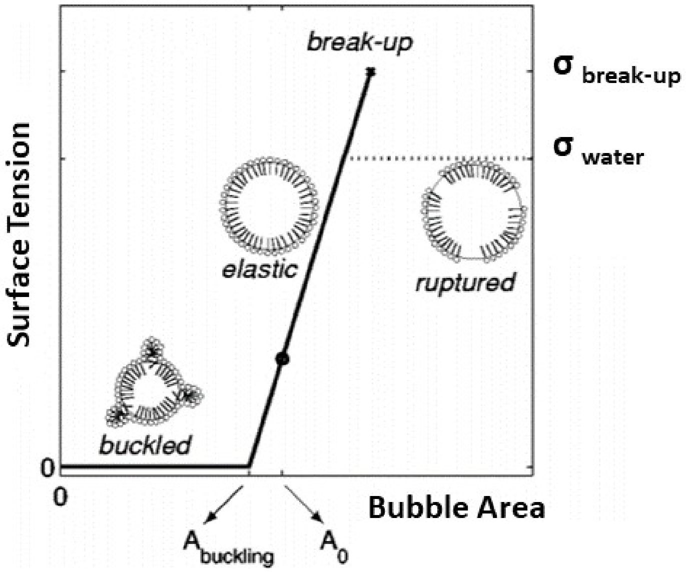

FIGURE 2.6: **Model for the dynamic surface tension of a monolayer coated bubble (continuous line)**. Image taken from [257]. The coating has a fixed number of lipid molecules, which corresponds to a monolayer at equilibrium (when area is A_0). The tension saturates to the water value σ_{water}(broken line) after the break-up tension has been reached ($\sigma_{break-up} > \sigma_{water}$).

The model only need three parameters to describe the effective surface tension: the buckling area of the bubble, $A_{buckling}$, below which the surface buckles, an elastic modulus χ that gives the slope of the elastic regime and the critical break-up tension, $\sigma_{break-up}$, that predicts for which bubble area the coating rupture occurs. When this limit is reached, the maximum surface tension saturates at σ_{water} (73 mN/m). These three regimes can be expressed as follows:

$$\sigma(R) = \begin{cases} 0, & \text{if } R \leq R_{buckling} \\ \chi(\frac{R^2}{R^2_{buckling}} - 1), & \text{if } R_{buckling} \leq R_{break-up} \\ \sigma_{water}, & \text{if } R \geq R_{break-up} \end{cases} \tag{2.20}$$

The phospholipid molecules, naturally adsorbed at the interface, shield the water from the air, reducing the surface tension σ to a value lower than that of pure water. Since surface tension depends on the surface concentration of molecules [259], when the compression of the monolayer decreases the area available per molecule, the effective surface tension decreases sharply. Further compression leads to an unstable situation where the monolayer buckles out of plane, while the surface tension nearly vanishes. In contrast, a slow expansion separates molecule from each other and surface tension rises. A monolayer made from pure lipid will show phase changes from a 2-Dimensional solid state, to a liquid and eventually gaseous state, where surface tension is close to that of water.

A fast expansion, such as the one triggers on a bubble by an ultrasonic pressure pulse, does not allow much time for any phase change and the monolayer breaks at a critical tension $\sigma_{break-up}$ exposing bare gas interfaces to the liquid. After break-up the surface tension relaxes to σ_{water}. The break-up tension can be higher than σ_{water} since any polymer component let more cohesion to the shell and shifts the break-up to higher tension.

In the middle condition, that is the elastic regime, the surface tension is a linear function of the area and the monolayer behaves as if it is composed of a thin solid and elastic material. The value of the elastic modulus can incorporate the presence of any solid-like shell material that sustain a tensile stress, such as the polyethyleneglycol polymer in SonoVue® contrast agent bubble. During the oscillation, the dynamical surface tension will vary, since it is a function of the bubble area and therefore of the bubble radius. Including the effective surface tension $\sigma(R)$ in the Rayleigh-Plesset equation *2.15* for the free gas bubble, combined with the polytropic gas law and the boundary condition, Marmottant et al obtained the equation of motion for a phospholipid-coated bubble:

$$\rho_L(R\ddot{R}+\frac{3}{2}\dot{R}^2) = [p_0+\frac{2\sigma R_0}{R_0}](\frac{R}{R_0})^{-3\gamma}(1-\frac{3\kappa}{c}\dot{R})-\frac{2\sigma(R)}{R}-\frac{4\mu\dot{R}}{R}-\frac{4\kappa_s}{R^2}-p_0-p_a(t) \tag{2.21}$$

This equation is identical to a free gas bubble equation, except from the effective surface tension $\sigma(R)$ term and the shell dilatational viscosity κ_s representing the frictions in the shell.

The effective tension model drastically changes the dynamics of the bubble. At small acoustic amplitudes, corresponding to small bubble vibration amplitudes within the elastic state, the model provides a linear radius response to the pressure, with symmetric expansion/compression cycles, similar to the Rayleigh-Plesset model with constant surface tension. The linearization of the equation leads to a damped oscillator equation

$$\ddot{x} + 2\xi\dot{x} + \omega_0^2 x = \frac{p_a(t)}{\rho R_0^2} \tag{2.22}$$

with x a small quantity and the damping coefficient $\xi = \frac{2\mu}{\rho_l R_0^2} + \frac{2\kappa_s}{\rho_L R_0^3} + \frac{3\kappa_s[P_0 + \frac{2\sigma(R_0)}{R_0}]}{2c\rho_L R_0}$.

Then, the resonant frequency can be simply written as

$$\omega_0^2 = \frac{3}{\rho_L R_0^2} K_V \tag{2.23}$$

where K_V is the compression modulus of the bubble. As is shown in Figure 2.7, the compression modulus is much higher when the bubble is in the elastic state, compared to a free gas bubble. In the free bubble state, this equation provides the Minneart frequency, as expected. So, bubbles in the elastic state have a much

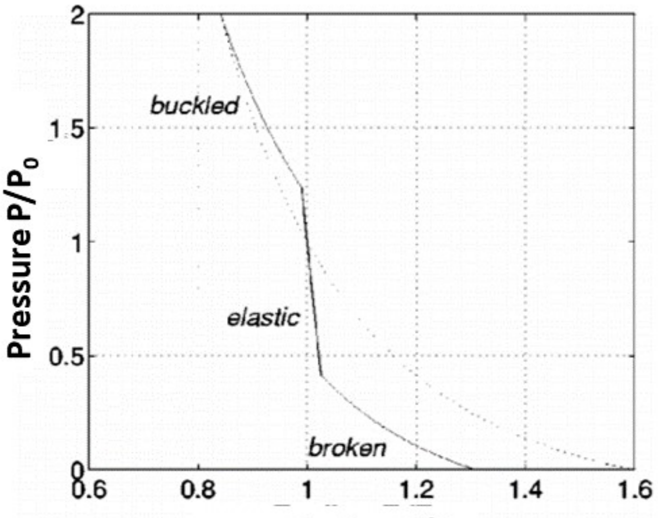

FIGURE 2.7: **Ambient pressure vs equilibrium radius for a coated bubble (continuous line) and a free gas bubble (dotted line)**. Image taken from [257].

higher resonance frequency than free or buckled bubbles, because their compression modulus is higher.

Under large acoustic pressure amplitudes, the bubble will experience an original non-linear response. It will likely buckle in its compression phase with large compressive deformations, making it vanish any surface tension. The radius response curve displays an asymmetry known as "compression only" behaviour [260], due to the rigidity of the coating shell that can hardly expand. An eventually break of the bubble shell, upon vary large amplitude of the acoustic pressure leads the bubble to revert to the classical Rayleigh-Plesset dynamics. High-frequency image recordings with lipid coated microbubbles reveal the existence of such asymmetric oscillations validating the model as shown in Figure 2.8 .

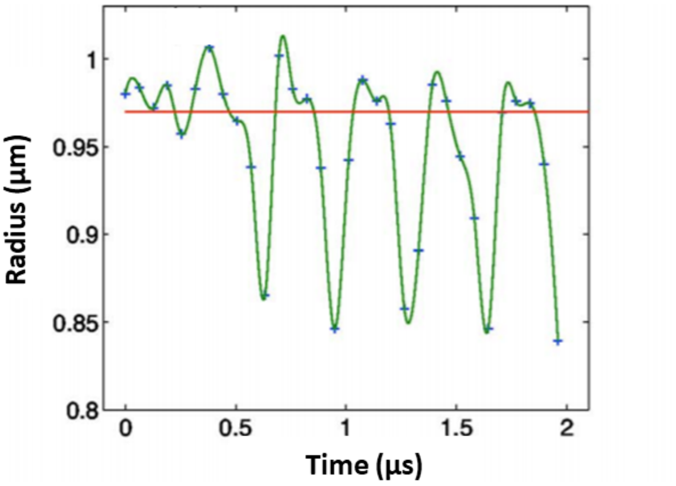

FIGURE 2.8: Image taken from [257]. Experimental recording of the radius of a SonoVue® bubble vs time, with the fast framing camera Brandaris (beginning of a 2.9 MHz pulse with an acoustic pressure of 130 kPa).

2.3 Primary and Secondary Bjerknes forces

An air bubble that exists, undisturbed and un-forced in a water tank experience a force balance between the volume of air inside the bubble, the hydrostatic pressure and the surface tension between the gas and the liquid. When the bubble is subjected to a pressure wave created by a traveling ultrasound field, inertial forces and ultrasound pressure waves are introduced, and the original forces become unbalanced by the introduction of these perturbances. When the lower pressure of the acoustic wave hits the bubble surface, it begins to expand due to the now lower pressure in the water just outside the bubble wall. As the bubble expands, it's wall push the water away from the centre of the bubble. This moving mass of fluid adds strong inertia to the dynamics of the bubble due to the large density ratio between the liquid and the gas inside the bubble. As the pressure reaches its minimum value for a given oscillation, the inertial forces from the water around the bubble are still expanding the bubble outward. As the peak of the pressure wave passes the bubble, the volume does not immediately begin to decrease because the liquid inertia around the bubble is still trying to expand it. This creates a delay (or phase lag) between the pressure fluctuations and the bubble's volume oscillations. The same is true with different magnitudes for the contraction phase. Under this condition the bubble experiences a translational force originates from the phase difference between the driving pressure and the bubble volume oscillations.

This phenomenon was first observed by Vihelm Bjerknes in 1906, who proposed the equation which describes the force acting in the direction of a traveling pressure wave on an air bubble, also known as primary Bjerkness force [264, 265].

Based on the law of kinematic buoyance and is analogous to the Archimedean law, Bjerknes proposed that "any body which participates in the translatory motion of a fluid is subjected to a kinematic buoyancy equal to the product of the acceleration of the translatory motion multiplied by the mass of water displaced by the body" [264].

It is possible to apply this statement directly to obtain an analytical expression for the mentioned force. The position of a particle of an oscillating fluid can be represented by

$$\xi(t) = \xi_0 + \xi_1 sin(\omega t) \tag{2.24}$$

where ξ_0 is the mean position and ξ_1 is its maximum displacement. The mass of the fluid displaced by an air bubble can be expressed simply as

$$M(t) = \rho V(t) \tag{2.25}$$

If the Bjerkness statement is applied directly, the force is given by

$$F'_B t = \ddot{\xi}(t) M(t) = \frac{\partial \mathbf{u}}{\partial t} \rho V_(t) \tag{2.26}$$

where $\mathbf{u}(t)$ is the fluid particle velocity. It is convenient to express the force in terms of the acoustic pressure $p_a(r,t)$ rather than the particle velocity. Consequently, to first order in p_a and $\mathbf{u}$,

$$\rho \frac{\partial \mathbf{u}}{\partial t} = -\nabla p_a(r,t) \tag{2.27}$$

The time averaged Bjerknes force on an air bubble, oscillating radially in a sound field, expressed in the form that is commonly used is then

$$F'_B(t) = -\left\langle V(t) \nabla p_a(r,t) \right\rangle \tag{2.28}$$

The passing US wave induces a pressure gradient acting upon the bubble surface, resulting in an instant force proportional to the product of the pressure gradient by the bubble volume. Averaged over a full cycle, the resulting net force has a non-zero value in the direction of the sound propagation, and the bubble is correspondingly accelerated in the same direction. In a case of a standing wave, the bubbles translate to nodes or anti-nodes of the acoustic field, depending on the phase difference between the bubble volumetric oscillation and the pressure wavefield. For details, the reader is referred to the large amount of literature, *e.g.*, Refs. [102, 264–266].

The velocity of a freely floating microbubble can reach values up to order of meters per second in case of resonant microbubble in water [266], compensated by the duty cycle of the pulses. For example, in case of 10% duty cycle, the bubble average velocity can reach up to 0.1 m/s, which can compete with regular blood flows in medium and small-sized vessel.

Beside the generation of the primary Bjerkness force, an ultrasonic wave may impact a different type of acoustic radiation force on microbubbles. A second Bjerkness force is generated between two vibrating microbubbles due to the pressure gradient in their re-radiated ultrasonic field. The expansion and contraction of microbubbles generates a force due to the relative acceleration between the fluid and pulsating body, which can attract or repel other microbubbles [264, 267]. The classical expression of the mutual interaction between bubbles was derived by V. Bjerkness father, C.A. Bjerkness, in 1868.

The Bjerkness theory is based on the following assumptions: (i) the surrounding medium is an ideal incompressible fluid; (ii) the gas within the bubbles obeys the adiabatic law; (iii) the spacing between the bubbles is much larger than their radii, so that the shape deviations of the bubbles from sphericity can be neglected; (iv) the incident wave is weak enough so that nonlinear oscillations are negligible. When these conditions are met, the Bjerkness theory is in agreement with experiments [265, 268] and the secondary radiation force, calculated according to the volume pulsation of bubbles, is written as:

$$F_B''(t) = \langle F_{12} \rangle - \frac{\rho}{4\pi d^2} \left\langle \dot{V}_1 \dot{V}_2 \right\rangle \tag{2.29}$$

From equation above, a negative force implies attraction and a positive one repulsion. The sign of the secondary Bjerkness force is directly related with the bubble resonance. If the driving frequency is in between the two resonant frequencies of the individual bubbles, they repel each other; otherwise mutual attraction occurs. However, the attractive and repulsive bubble behaviour is not always predictable in a MBs clouds. Experimental findings show that the mutual interaction among pulsating bubbles can cause the formation of stable bubble clusters due to the sign-reversal of secondary Bjerkness force [104, 105]. MBs can attract each other regardless of their sizes and form stable aggregation pattern, also referred as a “bubble grape” [269, 270], consisted of several bubbles noticeably larger than resonance size. This phenomenon, which cannot be explained using traditional natural-frequency analysis and Bjerkness theory, is tried to be explained by various researchers with different theories based on higher order harmonic emission from bubbles, multiple scattering or phase relation of the pulsations between the neighbouring bubble [270–273].

Chapter 3

Materials and Methods

In the first chapter of this thesis, the most important aspects of bio-cavitation have been discussed highlighting the strong interplay between oscillating bubbles and the possible cellular and molecular responses that may occur in different spatial and temporal scales. Several experimental studies have been mentioned to provide a state of the art of cavitation as a tool for endothelial permeabilization, facilitating the delivery of drugs to the targeted tissue. The physics of US-driven MBs was then introduced in Chapter 2 reporting the acoustic parameters used for drug delivery applications. The theoretical tools were given with the aim of understanding the physical laws governing the processes. In particular, the dynamic of a free gas bubble in a free liquid was compared with the one of stabilized MBs, considering also a confined system, *e.g.* constrained vessel.

The following chapter is intended to provide materials and methods used during the three years of thesis in order to carry out the experimental research. After describing the fabrication technique for the microfluidic devices, the cell culture and cell seeding protocols, adopted to reproduce the microvasculature on-a-chip, are reported. Fluorescent imaging techniques - exploited to validate the seeding protocol and establish the *in vitro* blood vessel integrity - and the protocols developed to stain cells within the microfluidic device are reported. We then describe the acoustic/optical set-up and the experimental procedures carried out to evaluate and quantify the blood vessel permeability and the effect of US-driven MBs on endothelial junction's morphologies. Finally, methods developed to post-process images are reported.

3.1 Microfabrication technique: Soft Lithography

Micro- and nano- fabrication techniques have revolutionized the pharmaceutical and medical fields as they offer the possibility for highly reproducible fabrication of miniature structures with complex geometries and functionalities, for the study of chemical, biological or physical processes at the cellular scale, including novel drug delivery systems. Typically, the sizes of features in these devices range from several micrometres to a few hundred micrometres and the amounts of fluid that are manipulated inside these devices are typically in the picolitre to nanolitre range. The most used technique to fabricate microfluidic devices is Soft Lithography. It can be viewed as a complementary extension of photolithography also called optical lithography or UV lithography. Basically, it uses light to transfer a geometric pattern from a photomask to a photosensitive (that is, light-sensitive) chemical photoresist deposited on a substrate (wafer).

Originally, standard photolithography, was mainly developed to deal with semiconductors used in the microelectronics industry [274]. Soft lithography, however, extends the possibilities of conventional photolithography applications. Unlike photolithography, soft lithography can process a wide range of elastomeric materials, *i.e.* mechanically soft materials. This is why the term "soft" is used. For instance, soft lithography is well suited for polymers, gels, and organic monolayers. Most devices, used in combination with cell biological research, are made of the silicone rubber polydimethylsiloxane (PDMS) because of its useful properties including low cost, biocompatibility, low toxicity, chemical inertness, as well as mechanical flexibility and durability.

Soft lithography technology is based on rapid prototyping and replica moulding [275] which means that the devices are elastic replicas of a stiff, re-usable mould. The mould is usually made of silicon with micrometre-size structures produced by building on top of the plate with the epoxy-based, photo-crosslinkable polymer

SU-8. The process starts from the design of the microfluidic networks, conceived using Computer Aided Design (CAD) software and printed on a high-resolution mask to be used as photomask in contact photolithography. The dissolution of the unpolymerized photoresist produces a positive relief, with the desired structures, on a silicon wafer, that serves as moulding master. Once the master is available, a small series of microdevices can be cheaply obtained by replica moulding.

The use of microfluidic technology in constructing sealed channels, for biological application, offers several potential advantages. First, smaller amounts of cells and reagents are needed per experiment. Secondly, low flow rates can be used to exert physiological levels of shear stress. Moreover, because of the small dimensions of microfluidic channels, fluid flow is fully laminar, meaning that the flow patterns are completely predictable and turbulent mixing does not occur. Third, the thin, planar and transparent microfluidic set-up is easily combined with bright field (BF) and Immunofluorescence (IF) microscopy, allowing the monitoring cells behaviour for long periods and with high magnification. It worth mentioning that, cells cultured inside microfluidic devices need to be subjected to a constant flux of fresh medium. Due to the small volumes in the cell-covered devices, static conditions are prohibitive since nutrients would be depleted quickly, and waste products would increase to undesirable concentrations. Besides, in *in vivo* physiological conditions, all cell types need a flux of nutrients to eliminate cells discarded material. Accordingly, the flow conditions into microfluidic devices mimic this process more closely than *in vitro* culturing in conventional wells-plates.

In this thesis we used a novel commercially available microfluidic chip, originally developed as a model of blood brain barrier-on-chip device [223, 224]. It presents several favourable features for replicating the functions of *in vivo* micro vasculatures and quantifying the cavitation-enhanced endothelium permeability. Among them, the real-time measurements and the possibility to reproduce physiological flow rate are key point.

In order to increase the resolution of molecular images acquired with confocal fluorescence microscopy, soft lithography was used to fabricate a homemade version of the original mould, bonded on a microscope slide (0.17 mm) instead of a conventional one, *i.e.* 1 mm thickness. In the followings, the commercial network design and the master fabrication steps used are listed. Combined with a 3-D perfused cell culture, the custom system allowed for a finer visualization of shear stress-induced actin filaments rearrangement in VECs.

3.1.1 The commercially available microfluidic network

The commercially microfluidic device is produced by SynVivo (Alabama, USA) and consists of a polydimethylsiloxane (PDMS) microfluidic chip plasma bonded to a glass slide of 1mm thickness, as shown in Figure 3.1A.

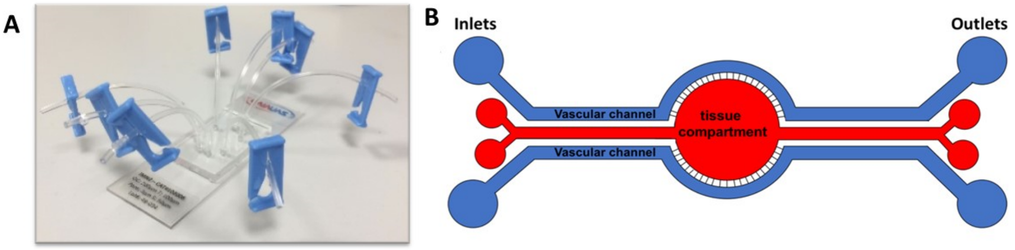

FIGURE 3.1: **Microfluidic network**. **A.** Image of the microfluidic device in PDMS, assembled on a glass slide with plastic tubes through which, each individual vascular channel and the tissue compartment, can be accessed. **B.** Sketch of the device's geometry showing the tissue compartment (red) surrounded by two independent vascular channels (blue) through a membrane of pores.

PDMS is an optically transparent polymer very easy to handle and used in many biological *in vitro* models. Indeed, it is compatible with biological assay since it is impermeable to water but at the same time permeable to gases. Thus, a sufficient transfer of CO_2 to the cells is allowed. The schematic illustration of the device is sketched in Figure 3.1B. The device consists of a central circular tissue compartment (1575 μm width, 100 μm height) encircled by two independent vascular channels (200 μm width, 100 μm height), where VECs can be seeded to reproduce the three-dimensional morphology of *in vivo* blood vessels. An interface consisting of a series of radial pores (3 μm x 3 μm x 100 μm, width x height x length), spaced every 50 μm along the length of the vascular channels, separates the vessels from the tissue compartment. The device also allows different co-culture: cells can also be cultured into the tissue compartment, with a 3-D structure, in order to mimic the targeted tissue. A relevant example is the complex biological micro-environment formed when tumour cells are seeded into the tissue compartment near the vascular channel. Such *in vitro* disease model allows for immunological research related to cell-cell interaction in tumours [203, 276].

3.1.2 Master fabrication steps

To perform PDMS soft lithography, a rigid mould that contains patterned relief structures on the surface is needed. The most used mould is the epoxy resin SU-8 negative photoresist. "Negative" refers to a photoresist whereby the parts exposed to UV light become cross-linked, while the rest remains soluble and can be washed away during development. The SU-8 mould fabrication process, shown in Figure 3.2, can be divided into 4 main steps that are: wafer pre-treatment, photoresist spinning and soft baking, exposure and post-exposure treatment, development and hard baking. As seen in previous section, the geometry of the commercial network, include two different highs, one characteristic for the channel

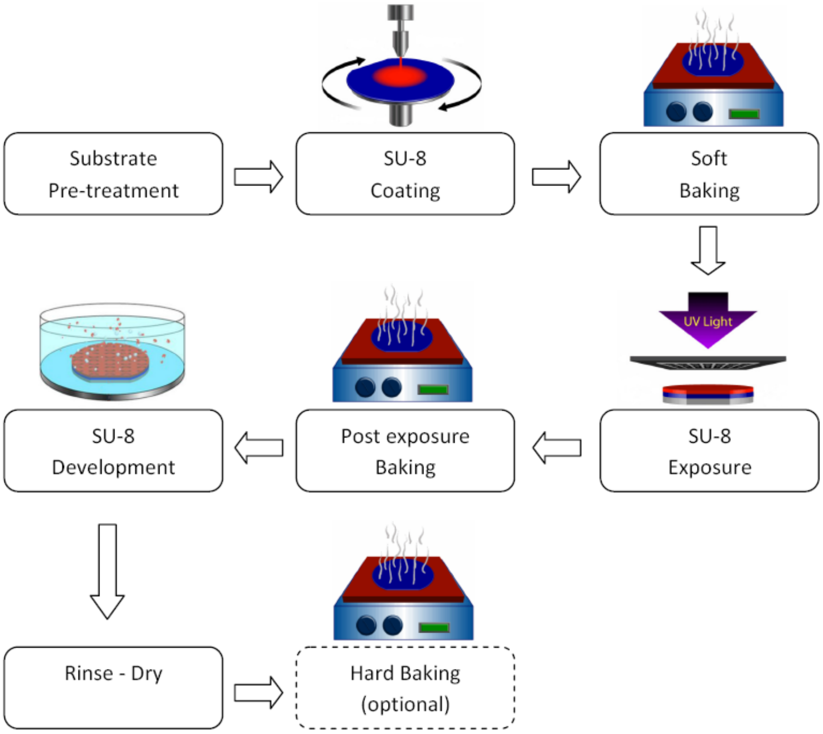

FIGURE 3.2: **Sketch of the SU-8 mould fabrication process**. Image taken from [277].

(100 μm) and one specific for the pore's membrane (3 μm). To enable lithography with such resolution, a double exposure Lithography process has been used. All the steps, explained below, will refer to the first fabrication process performed to obtain an initial patterned relief of 3 μm. Once the hard baking, as last step, is made, all the passages will be repeated to obtain the final relief, increased up to 100 μm.

Substrate Pre-treatment Physical contaminants such as dust particles can hinder the lithography process by preventing light from exposing the photoresist or by disturbing the surface uniformity of a coated photoresist. Chemical contaminants may also react with various materials used in the lithography process, creating unwanted effects. A silicon wafer is the most commonly used platform for microfabrication and a variety of cleaning methods can be used to prepare it for lithography process. Here, a Piranha solution is used to clean the silicon substrate immersing the wafer in a mixture of $H_2SO_4 : H_2O_2$ (1:3) for 20 minutes. The piranha solution is highly oxidative and removes metals and organic contamination from the wafer surface. After this step, the substrate is washed with distilled water and carefully dried with compressed air since the presence of water compromises the adhesion between the photoresist and the wafer.

Resist Spinning and Soft Baking To create the SU-8 photoresist layer, which is later moulded, we use a spin coater. The spin coating is probably the most used technique to create a photoresist layer of a desired thickness and consists in putting a puddle of liquid photoresist onto the wafer that is held by a vacuum chuck on a rotated spinner. The wafer is then spun in one or more steps at precisely controlled speeds to let the centrifugal force causes the liquid to flow to the edges, allowing for the formation of a uniform film. The rotation speed, the acceleration and the SU-8 photoresist viscosity will define the thickness of the SU-8 photoresist layer. Due to the particular geometry of the network, which is characterized by a membrane of pores of 3 μm in high, 97 μm less than the vascular channel, a double resist spinning is needed in other to obtain two different high for the photoresist layer.

We use SU-8(3005) (MicroChem, Newton, MA) that is spun firstly at 500 rpm with an acceleration of 100 rpm/s for 5 seconds and then at 3000 rpm for 30 seconds with an acceleration of 300 rpm/s, in order to obtain a first thickness layer of 3 μm. After the exposure and development steps with subsequent hard baking procedure a new spinning process is performed to increase the thickness of the incomplete relief up to 100 μm, before replica moulding. The procedure is slightly different with the SU-8(3050), that is spun at 500 rpm with an acceleration of 100 rpm/s for 5 seconds and then at 1000 rpm for 30 seconds with an acceleration of 300 rpm/s. The quality of the resist coating determines the density of defects transferred to the device under construction. After spin coating, the resist still contains up to 15% solvent and may contain built-in stresses. The wafer is therefore soft baked (pre-baked) at 65°C for 2 minutes and then at 95°C for 30 minutes to remove solvents and stress, and to promote adhesion of the resist layer to the wafer.

Exposure and Post-exposure Treatment The aim of the exposure is to initiate the cross linkage by the activation of the Photo Active Components (PACs) in some parts of the photoresist, depending on the photomask design. This activation changes the local properties of the resin which, after baking, is soluble or not into a solvent. Since the SU-8 is a negative photoresist, it means that the part exposed to the UV light become hard and the other part dissolves during the development. Here we use a UV exposure box (UV-KUB3, Kloe, FR), in contact mode with two complementary photomasks (Figure 3.3).

A first exposure is performed after depositing the 3 μm SU-8 layer, to obtain the positive relief of the pore's membrane (Figure 3.3A,C). Here, UV exposure parameters are set at 50% power for 13seconds. After development passage and subsequent hard baking, a new resist spinning step is performed to obtain a 100 μm SU-8 layer. A second exposure treatment is then made to cross-link the complementary structural features of the microfluidic device, using a photomask aligner (Figure 3.3B,D). For this step, UV exposure parameters are set at 55% power for 20seconds. It is useful mentioning that the exposure wavelength of the SU-8 is 365 nm.

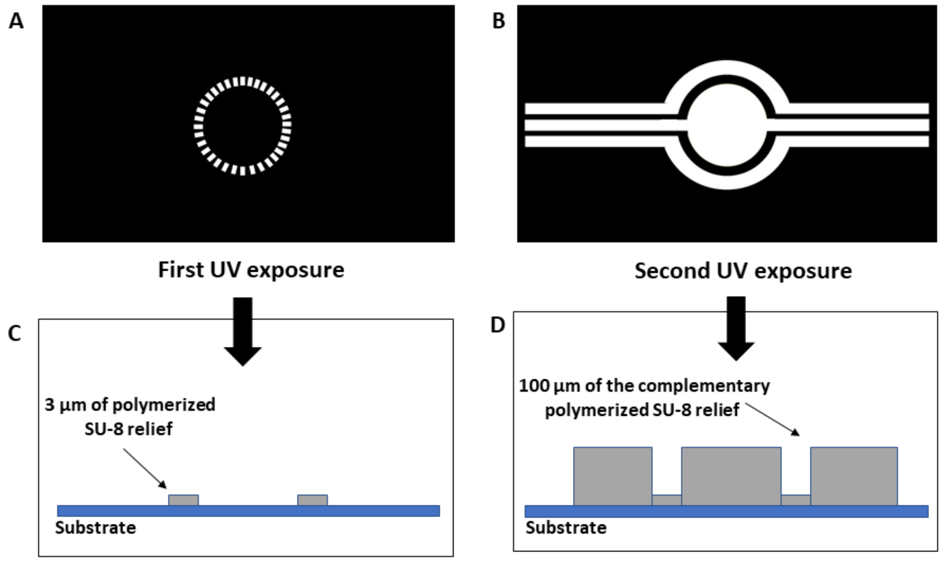

FIGURE 3.3: **Sketch of the two complementary photomasks**. **A.** Photomask caracteristic of the 3 μm pores membrane. **B.** Complementary structural features that, after the second resist spinning, let the UV to cross-link the resin up to 100 μm.

Post-exposure treatment is often desired because the reactions initiated during exposure might not been finished. The second photoresist bake is called Post Exposure Bake (PEB). The UV exposure enables the activation of the photoactive components in the SU-8 photoresist, but it needs energy to continue the reaction; this bake brings that energy. As for the soft bake, the most delicate issue is the mechanical stress inside the SU-8 photoresist: heating and cooling down must be performed slowly to minimize it. The heating ramp is the same as in the soft bake: a first plateau at 65°C is kept for 2 minutes then a second at 95°C for 10 minutes only, instead of 30 minutes.

Development and Hard baking The development is the step where the non-linked SU-8 photoresist is diluted in solvent. The SU-8 can be developed thanks to the SU-8 developer mainly composed of Propylene glycol monomethyl ether acetate (PGMEA) (MicroChem, Newton, MA). During the development process, for both exposure photoresist passages, the substrate covered with the exposed SU-8 photoresist and at room temperature (RT) is immersed for at least 3 minuntes into the SU-8 developer. Therefore, selective dissolving of resist takes place and the pattern is revealed on the substrate. Unwanted residual photoresist sometimes remains after development. Thus, Post-baking is performed to remove residual solvents and anneal the film to promote interfacial adhesion of the resist, which is weakened by developer penetration. The wafer is therefore washed with Isopropyl alcohol, dried with compress air and post-baked once again with the same heating ramp; from 65°C for 2 minutes to 95°C for 4 minutes. The third and last photoresist bake is called "Hard bake" and is the last optional step of the process. At the end of the process a lot of stress, capable of cracking the surface or even delaminating the layer, remain inside the SU-8 photoresist. Hard baking suppressed these strengths improving the hardness of the film and increasing its resistance to subsequent deposition steps. The Hard bake is performed at higher temperatures (105°C) and for longer times (*e.g.* 1hour) than soft baking or prebaking. After that, the SU-8 master mould is finally ready.

Replica moulding In order to obtain the sealed PDMS channels, a last step namely replica moulding, is necessary. This process consists in shaping the flexible polymer using the SU-8 master mould. The PDMS solution is then poured onto the complete patterned SU-8 mould, heated up to allow the solidification by crosslinking, and peeled off from the mould. The polymerized PDMS surface is activated with oxygen plasma and bonded to a microscope glass slide with a plasma cleaner (PDC 002-CE, Harrick Plasma, USA) using a plasma power of 27 W at pressure of 680 mTorr. Holes can be punctured to reach the closed channel structure and tubing can be connected to manipulate fluid inside the channels. The bonding process creates a tight seal between the PDMS and the glass, so that fluids and cells remain confined to the micro channel. Indeed, when the microchannels are properly sealed, fluids can be pumped in at pressures as high as ∼350 kPa without failure [278]. Once the master-mould has been created, producing new microfluidic devices by this method takes only a few hours. Because the materials are cheap, microfluidic devices can be discarded after every experiment.

3.2 Realization of the blood vessel-on-a-chip

In pharmaceutical field, *in vitro* realistic models mimicking the microvasculature are needed to allow the study of functioning mechanisms involved in drug permeation to the target of interest as well as the screening of new pharmaceuticals.

The *in vitro* system, proposed in this experimental work, consists of an artificial 3-D tight endothelial barrier, that provides a platform for the study of microbubbles cavitation efficacy which temporarily enhances the *in vitro* blood vessel permeability. Here, we report the procedure for culturing specific cells (*i.e.* Human Umbilical Vein Endothelial Cells, HUVECs) into the vascular channels of the microfluidic device previously introduced. The perfused shear stress protocol, developed to let the cells express the physiological features of a mature *in vivo* endothelium, is also mentioned.

3.2.1 Cell-line

HUVECs were purchased from Lonza (Walkersville, MD, USA). The culture medium is the endothelial basal medium-2 (EBM-2) supplemented with the endothelial growth medium (EGM-2) Bullet Kit from Lonza (Walkersville, MD, USA). Cells are grown in treated 75 cm^2 polystyrene culture flasks and maintained in humidified atmosphere at 37°C and 5% CO_2. The culture medium is changed every 2 days and cells are used up to the 5th passage to ensure the expression of key endothelial protein components. Once the cells reach the desired confluence ($85 - 90\%$), they are washed twice with Dulbecco Phosphate Buffered Saline (PBS) (Sigma Aldrich, Missouri, USA) and detached using Trypsin EDTA solution (Sigma-Aldrich, Missouri, USA) for 40seconds at 37°C in 5% CO_2. The latter is an enzyme that cleaves peptide chains, here used to break down proteins responsible for cells adhesion and detach the HUVECs from the flask's surface. In few seconds cells detach and a Trypsin Neutralizing Solution (TNS) (Sigma-Aldrich, Missouri, USA) is added to the flask to neutralize the effects of trypsin. Afterwards, the cell suspension is collected and centrifuged at 1400 rpm for 7 minutes at Room Temperature (RT) and the supernatant is discarded. Finally, cells are resuspended in filtered culture medium at an average concentration of 10^8 cells/ml.

3.2.2 Cell-seeding protocol

The protocol used to seed HUVECs into the microfluidic device was adapted from [194, 223]. A sketch of the main experimental passages is shown in Figure 3.4.

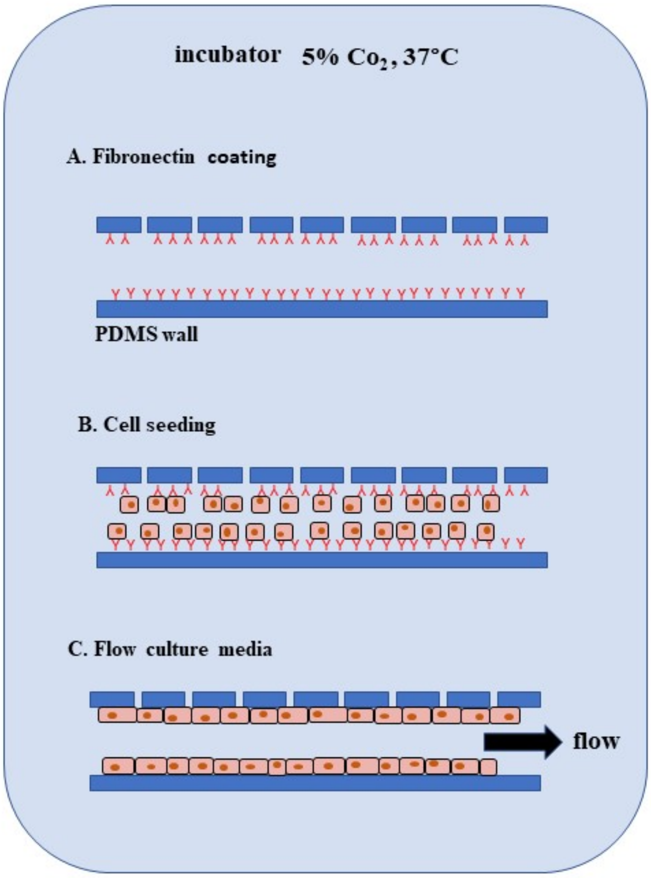

FIGURE 3.4: **Main Steps of cells seeding protocol**. **A.** PDMS wall functionalization with fibronectin protein in order to promote the adhesion of HUVECs to the substrate. **B.** HUVECs injection until reaching a proper concentration $(60 - 70\%$ confluence). **C.** Application of a physiological flow rate to reach the characteristic elongated phenotype of VECs in *in vivo* capillary.

To form a 3-D endothelial monolayer into the PDMS channels, the device is first degassed, washed with PBS and then functionalized to favour HUVECs adhesion by perfusing the channels with the fibronectin (200 μg/ml) (Sigma-Aldrich, Missouri,USA) at 37°C and 5% of CO_2 for two hours (Figure 3.4A). Fibronectin is a glycol-protein of the extracellular matrix (ECM) involved in vascular development. It binds to cellular membrane receptor proteins, called integrins, favouring HUVECs adhesion to the surrounding ECM.

Once detached from the flask using the procedure explained in the Subsec. 3.2.1, HUVECs are introduced in the vascular channels with a programmable multiple syringe pump (PhD ULTRA Syringe Pump, Harvard Apparatus, Massachusetts, USA). The input and output Tygon tubes (Saint Gobain PPL Corp, Pennsylvania, USA) are clamped only when HUVECs reached the desired confluence ($60-70\%$) into the channel (Figure 3.4B). The device is placed into a CO_2 incubator at 37°C for 4 hours, to let the cells bind the fibronectin and attach to the channel inner walls in static condition. After incubation, each inlets tubing is immersed in a reservoir of culture medium placed inside the incubator. Instead, the outlet of each vascular channel is connected to a 1 mL empty syringe (Fisher Scientific, Pennsylvania, USA) using Tygon tube. Syringes are mounted on the multiple syringe pump, next to the incubator, that withdraws the syringe's piston and thus pulls the liquid from the reservoir into the channels (Figure 3.4C). Placing the reservoirs inside, rather than outside the incubator, ensures that the culture media temperature is already at 37°C before entering the vascular channels, reducing cells stress induced by temperature changes and allowing for a uniform temperature along the channel. In the following, the shear stress application protocol developed to obtain a mature endothelium under physiological flow condition is described.

3.2.3 Shear stress application

To orient the cells and reach the full maturation of cell-cell junctions under physiological shear flow, the vascular channel is connected to a multiple syringe pump using Tygon tubes as explain above. The withdraw rate is ramped up to 0.5 μl/min over 24 hours. The ramp up mode allows for the cells to gradually adapt to the fluid flow changes. After an overnight, the culture medium inside the reservoirs is refreshed and pulled into the channel at a flow rate up to the desired one (0.5, 25 μl/min depending on the experiments). Indeed, in order to examine the state of the endothelium at different stages, quasi static (0.5 μl/min) or physiological flow conditions (25 μl/min) are kept for additional 2 days to achieve full junction maturation.

The average wall shear stress associated with the flow rate applied can be calculated using the following equation:

$$\tau = 6\frac{Q\mu}{w^2h} \tag{3.1}$$

with τ the shear stress in $dyne/cm^2$, Q the flow rate in μl/min, μ the dynamic viscosity in Pa·s, w and h the width and height of the channel in m. The derivation of Equation *3.1* can be found in Appendix A. The dynamic viscosity of the medium at 37°C is approximately the one of water and was set at $8 \cdot 10^{-4} Pas$. Inserting a flow rate of 0.5μl/min, and 25 μl/min, according to the dimension of the channels, the resulting average shear stress on the wall is estimated to be approximately 0.2 and 10$dyne/cm^2$, respectively. All shear stress experiments were performed in an incubator at 37°C and 5% CO_2.

Once the resembling blood vessels are ready, cells in the vascular channels are either stained with different markers (refer to the following section) or used for endothelium *in vitro* experiments (as explained in the following Sec.3.4).

3.3 Cells staining into the microfluidic device

Cells distribution, confluence and viability inside the vascular channel are crucial aspects to validate the protocol and establish the *in vitro* blood vessel that mimics the *in vivo* one. Moreover, to investigate on the bioeffects induced by MBs behaviour on inter endothelial junctions and cytoskeleton organization, imaging technique are needed. In this contest, fluorescence microscopy is a useful technique.

Upon appropriate staining protocols, the device is placed on the stage of a microscope (Olympus iX73FluoView 1200). Images in BF yields approximative information mainly regarding the cells shape and their confluence, while IF staining protocol combined with confocal microscopy allows also for qualitative and quantitative analysis of several parameters, *e.g.* cells viability, cells cytoskeleton rearrangement and cellular junctions openings. With this purpose, several fluorescent markers can be used depending on the specific target of the analysis. In some cases, when a protein of interest is intracellular (inside the cells), it is necessary to fix and permeabilize the cells in order to allow the passage of the fluorescent antibody. This procedure is not required when the protein of interest is expressed on the cells surface.

In the following, the protocols developed for staining the cells with Calcein (live staining) and different antibodies (immunofluorescence staining), are described.

3.3.1 Live cell staining

Calcein AcetoxyMethyl(AM) is a widely used cell-permeant dye which can be transported through the cellular membrane into live cells, assessing the viability of most eukaryotic cells. Once entered the living cell, the non-fluorescent hydrophobic Calcein AM is converted to a green-fluorescent hydrophilic Calcein after acetoxymethyl ester hydrolysis by intracellular esterase. This allows for the qualitative or quantitative analysis for cells viability by fluorescence microscopy since the fluorescent Calcein is well-retained into the cytoplasm. Calcein has excitation wavelength at 495 nm and emission at 515 nm. It is thus excited with a 488 nm laser and acquired using a $530 - 30$ nm filter.

After shear stress application (see subsec.3.2.3), the microfluidic device is disconnected from the syringe pump and the cell-covered channels are washed with PBS using the syringe pump set at 0.5 μL/min for 30minutes to remove debris and prepare the cells for Calcein staining. Afterwards, the Calcein AM (Thermofisher Scientific) diluted in PBS up to the desired molarity (100 μM) is injected at a flow rate of 0.5 μL/min for 1hour in the incubator. Finally, the channel is washed again with PBS at the same flow rate for 15 minutes to remove the unbound reagent and placed on the microscope stage for images acquisition. Wide-field fluorescence images of different portions of the endothelium are acquired using a 20X magnification objective, with the CoolSNAP MYO CCD camera (TeleDyne, Photometrics, AZ), and successively stitched together to reconstruct the whole channel.

3.3.2 Immunofluorescence staining

IF staining is a widely used technique in biological research and utilizes fluorescent labelled antibodies in order to detect specific target antigens. Here, IF staining is used to investigate endothelium state through experiments at different stages (*i.e.* maturation, ultrasound excitation, MB irradiation and eventual recovery) evaluating Von Willebrand protein, focal adhesion, changes in F-actin stress fibres organization and VE-cadherin protein.

For staining protocol, incubations and washings into the microchannels are performed at 0.5 μl/min flow rate unless otherwise stated. After shear stress application (see subsec.3.2.3), the microfluidic device is disconnected from the syringe pump and the channels are gently washed for 30minutes in PBS flow to remove debris and prepare the cells for antibody staining. Cells inside the channels are then fixed in 4% paraformaldehyde(PFA) for 15minutes at RT in static conditions and permeabilized for 5 minutes in 0.2% Triton X-100 (Sigma-Aldrich, Missouri, USA). The letter passage is an essential key for fluorescence imaging since the proteins, investigated in this study, are intracellular proteins and it is necessary to permeabilize the cells before staining them to allow the antibody entry. Cells are then blocked with 30 minutes flow of 3% bovine serum albumin (BSA) to prevent non-specific binding of antibodies. Immediately after the latter passage, the cells are co-immunostained, according to the experiments, with antibodies against Von Willebrand Factor (rabbit monoclonal antibody [EPSISR15] Alexa Fluor®647 conjugated, abcam, diluted 1:40 in 3% BSA), vinculin (mouse monoclonal antibody unconjugated, diluted 1:400 in 3% BSA, Sigma-Aldrich), VE-cadherin (mouse monoclonal antibody unconjugated, 5 μg/ml in 3% BSA, Thermo Fisher Scientific) and actin filaments (Phalloidin-Atto488, 30 μl/ml in 3% BSA, Sigma Aldrich) for 60 minutes in the dark. After washing, fluorescent secondary antibodies (AlexaFluor®647 or highly cross-adsorbed CFTM594 conjugate anti-mouse antibodies, at 2 μg/ml and 6 μg/ml in PBS respectively) were added for 60 minutes, still in the dark at RT. Nuclei were stained with DAPI (Thermo Fischer Scientific). Finally, the channels are washed with PBS and placed on the microscope stage. Depending on the experiment, cells were stained before

US exposure to assess endothelial maturation; immediately after US exposure to evaluate the effect of oscillating microbubble on inter-endothelial junctions and 15 and/or 45 minutes after US exposure to address endothelium integrity recovery under flow conditions. Wide-field fluorescence images of different portions of the endothelium, at the desired excitation wavelengths, are acquired using a 20X magnification objective, using the MYO CCD camera and successively merged and stitched together to reconstruct the whole channel.

3.4 Experimental set-up and procedures

After validating the protocol and establishing the *in vitro* blood vessel, the commercial bio-inspired device is used for cavitation-enhanced endothelium permeability *in vitro* experiments. In particular, the vascular membrane permeability and MBs dynamics in the near proximity of the endothelial wall are both monitored thanks to a dedicated experimental set-up, integrating the *in vitro* blood vessels and the unfocused transducer within a water-filled and temperature-controlled costume chamber, located on the microscope stage (Figure 3.5).

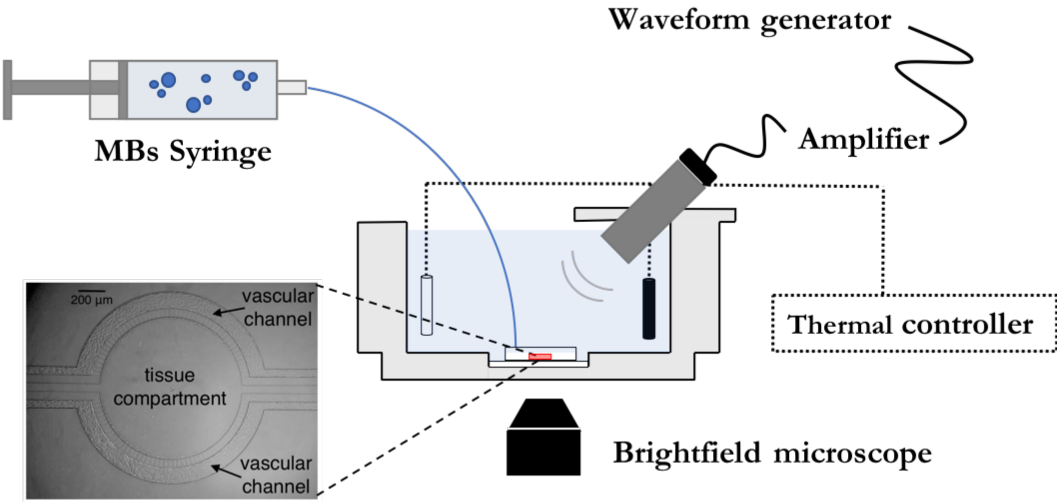

FIGURE 3.5: **Sketch of the ultrasound chain**. It shows the dedicated insonication chamber, the microfluidic chip placed at the chamber bottom (enlarged view on the bottom left of the image), the thermal control to keep the biological system at 37°C, the piezo transducer generating the US at 1 MHz and the MB injection syringe.

3.4.1 Microbubbles

SonoVue® MBs (Bracco Research, Geneva, Switzerland), filled and stabilized with sulphur hexafluoride (SF_6) and coated with a phospholipid monolayer shell [163], are used in this study. The bubbles suspension is reconstituted in 5 ml of 0.2% NaCl solution ($2-5\cdot10^8$ microbubbles/ml) according to the manufacturer's instructions. The preparation is diluted to a concentration of $2-5\cdot10^7$ microbubbles/ml in culture media to reach the desired cell-bubble ratio (1:1) [62, 279]. Then, the bubble solution is injected into the vascular channel with the syringe pump, as later explained in subsec. 3.4.3. With a size ranging between 2-8 μm and a mean diameter of 2.5 μm, microbubbles were small enough to avoid vascular channel obstruction.

3.4.2 The insonication chamber design

Building the experimental set-up implied the fulfilling of several physical and biological conditions. Indeed, because of the variations within the near acoustic field (see Appendix B), it can be difficult, in this region, to accurately evaluate the pressure driving MBs dynamics inside the vascular channel. The transducer, immersed in water to guarantee US propagation, had to be positioned far from the sample within a distance that falls in the far acoustic field. This is obtained thanks to the transducer calibration as discussed later and allows the control over the pressure inside the vascular channel. Also, for a simultaneous emission of the US and observation of the vessel, the piezo had to be placed such that the microscope light could pass undisturbed from the source to the device. Finally, the sample must be kept at 37°C to ensure physiological conditions for the endothelial vessel.

In order to meet these conditions, a devoted insonication chamber was first designed with the software Rhinoceros (see Figure 3.6A) and then realized with a 3-D printer using Grey Photoreactive Resin (FormLabs, Massachusetts, USA) (Figure 3.6B). To guarantee precise control over the transducer alignment, the chamber is provided with a dedicated housing on top of the insonication chamber that holds the US emitter with an inclination of 45° and at 35 mm from the microfluidic chip. At the bottom of the chamber, where the device is placed, a plexiglass window allows for optical acquisition.

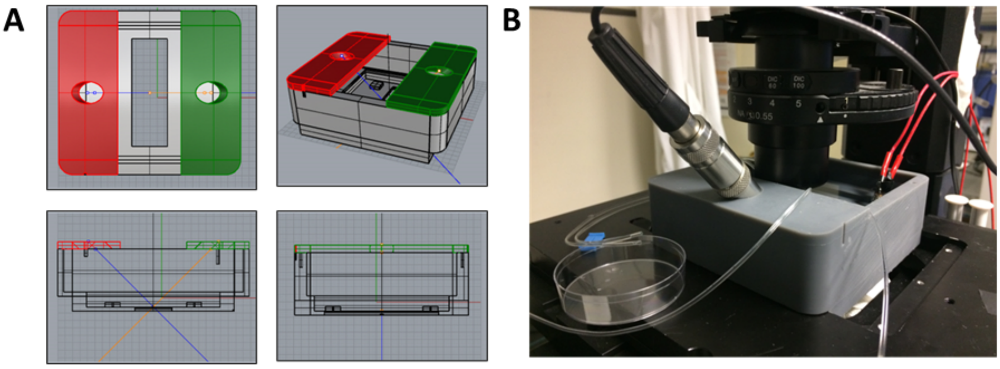

Figure 3.6: **Insonication costume chamber.** **A.** Different views of the chamber sketch drawn with Rhinoceros software. **A.** Picture of the chamber realized with 3-D printer and mounted on the microscope stage. The US emitter was mounted on the top of the chamber with an inclination of 45° at a distance of 35 mm from the microfluidic chip.

The 1MHz-centre-frequency transducer (V303-SU, Parametric) with 0.5 inches (13 mm) diameter was firstly calibrated using a needle hydrophone, see Figure 3.7A. The transducer was immersed in a tank filled of degassed water. After finding the maximum pressure in the X-Y plane, a scan along the axial direction allows to determine the distance N between near and far field. As shown in Figure 3.7C, the solid line at 25mm remarks the boundary between the two distinct fields (N) for two driving voltages, 80mV and 140mV respectively. This founding was in agreement with the theoretical value calculated with the equation shown in Appendix B. In far field, the acoustic field in the plane XY was reconstructed (Figure 3.7B). It is worth noting that the lateral resolution ensures a uniform US exposure over the two channels.

In order to evaluate the amount of ultrasound absorbed by the thickness of the PDMS during the experiment, the device was placed at the right distance from the transducer, resulting in the 13

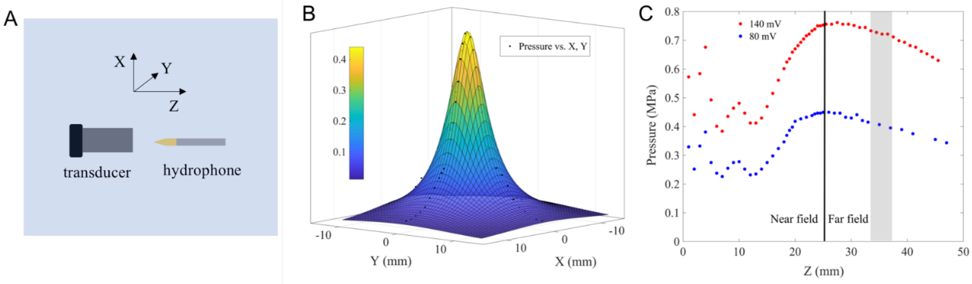

FIGURE 3.7: **US emitter calibration. A.**sketch of the calibration set-up. **B.** Example of pressure distribution on the cross-plane X-Y at 80mV driving voltage and axial position Z=30mm. C. The two plots provide maximum cross-plane pressure vs axial distance Z measured from the transducer for two driving voltage, 80mV and 140mV, respectively. The solid line at Z=25mm highlights the boundary between near and far field. During insonication experiments, the microfluidic chip is located at the bottom of the insonication chamber within the shade range of distances (∼35mm).

3.4.3 Acoustic and optical set-up

Ultrasound bursts are generated using a signal generator (Tektronix AFG3022c, USA), amplified by a 50-dB power gain amplifier (ENI 240L) and monitored with an oscilloscope (Tektronix TBS1064, USA). The amplified electrical signal is sent to the unfocused transducer which transmits the US signal within the custom insonication chamber filled with deionized water. The chamber is then positioned on the confocal microscope stage for real-time acquisition with an EMCCD camera (Evolve®512 Delta). Phase contrast imaging is performed to monitor vessel integrity and microbubble dynamics. The device is stably placed at the bottom of the chamber. Culture medium (plus 2.5% HEPES as a buffer solution to keep the cell's physiological pH stable) is injected into both vascular channels at the same flow rate that is varied according to the experiments (0.5 or 25 μl/min). The system is then allowed to adapt to the new conditions for 30 minutes while kept at 37°C by a PID thermal controller (Figure 3.5). Cells are monitored with a time-lapse, acquiring one image per minute with an exposure time of 300 ms. Sonovue® MBs are finally injected at 1 μl/min into a single vascular channel and exposed to sine-wave bursts with 1MHz central frequency, 500 cycles, 0.1% Duty Cycle(DC), corresponding to 500μs Pulse Duration(PD) and 20Hz Pulse Repetition Frequency(PRF) for 30 seconds. Since the channel free of MBs is far from the other one around 1,5 mm, such configuration allows for a comparison of the acoustic mechanical effects with those amplified by MBs within the same sample and almost at the same acoustic pressure. In fact, from the piezo calibration, at 1.5 mm distance from the maximum peak, the pressure amplitude is reduced only by the 14%.

Two different insonication conditions were performed, with the emitter transducer driven at 80 mV and 140 mV, respectively corresponding to 0.4 and 0.72 MPa Peak Negative Pressure(PNP), 5 and 7 W/cm^2 intensity level. Time-lapse imaging at 10fps with 10ms exposure time was used to visualize bubble flow.

In order to evaluate the endothelium immediately after bio-effects of the ultrasound exposure, the device is removed from the insonication chamber and transported under the biological wood. It is then washed with PBS and perfused with 4% PFA to prepare the cells for antibody staining (see subsec.3.3.2). Alternatively, the device is removed from the insonication chamber, placed in the incubator and perfused with the same flow culture condition for 15 or 45 minutes prior to be fixed with 4% PFA and stained for integrity's recovery evaluation.

3.4.4 Permeability assay

The experimental method used to quantify the tightness of the artificial endothelial barrier is here described. Using the same experimental protocol described in Subsec. 3.4.3 the device is placed into the acoustic insonication chamber and then analysed in different conditions (*i.e.* free cells, seeded with HUVECs or in presence of irradiated MBs). The vascular channel is perfused with culture medium (plus 2.5% HEPES) at the appropriate flow rate (25 μl/min) and allowed to adapt to the new conditions while kept at 37°C by a PID thermal controller for 30 minutes. The inlet of the vascular channel is then connected to a Hamilton syringe filled with a fluorescent dye (Texas Red-dextran 40 kDa, Thermo Fisher Scientific, 5% diluted in culture medium, starting from a stock concentration of 10 mg/mL). Due to the high molecular weight of the dextran, it well mimics the pharmaceutical macromolecule that fails to diffuse across the endothelial barrier. The fluorescence dye is then injected into the vascular channel at a flow rate of 1 μl/min and monitored under the confocal microscope. This flow rate allows for the passive diffusion of the fluorescent dye through the membrane of pores with or without HUVECs lining the PDMS side walls. For the quantification of endothelial permeability in presence of MB-irradiated by US, a slight change to the protocol is made. The Tygon tube, connected with the fluorescence-filled syringe is immersed in an Eppendorf where SonoVue® are diluted at the proper concentration within a solution made of Texas-red 5% in culture medium. The solution is then pulled through the Tygon tube for a total volume of 20 μl and injected into the vascular channel at the same flow rate of 1 μl/min. The tiny volume of MBs ensures their presence within the channel only for the first minutes of the experiment, when US are emitted, then allowing the fluorescence dye to freely flow into the vascular channel for the rest of the time.

As the fluorescent dextran accumulates in the central circular tissue compartment in a time-dependent manner, its permeability across the endothelial monolayer is estimated thanks to a time-lapse acquisition over two hours with an exposure time of 300 ms and a frame rate of 1 image per minute. The intensity evolution of the fluorescence signal within the tissue compartment is detected using the EMCCD camera with a 2X magnification objective.

3.5 Image analysis

3.5.1 Actin filaments remodelling

Changes in actin filaments organization, in particular for the F-actin stress fibres, under different experimental conditions (*i.e.* maturation, USMB excitation and eventual recovery) are assessed by using PhalloidinAtto488 staining. Actin filament density ($n°/\mu m$) along the smaller axis of cell is determined by performing line scan tool in ImageJ software. Lines, along which the intensity of PhalloidinAtto488 fluorescence is measured, are drawn in individual cells, perpendicular to the F-actin stress fibres (Figure 3.8).

This procedure was repeated for 30 cells randomly chosen along the vascular channel. After correction for background fluorescence, the resulting fluorescence intensity profiles are analysed for the number of peaks above a proper baseline and

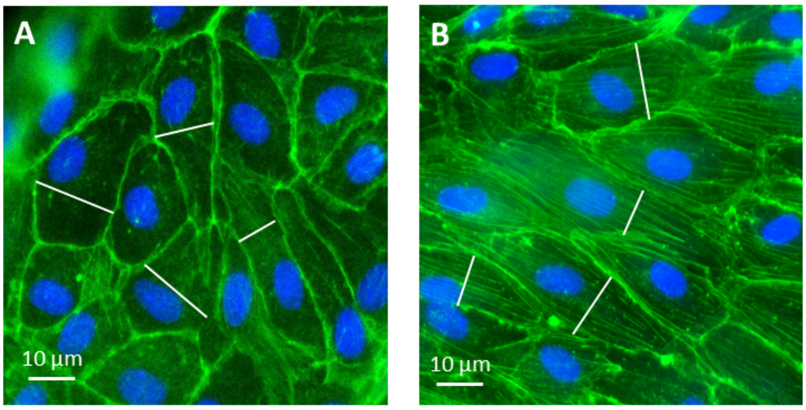

Figure 3.8: **Actin filaments remodelling analysis using line scan tool.** Representative fluorescence images of HUVECs stained for F-actin stress fibres (green) using PhalloidinAtto488 staining protocol at different condition,*i.e.* maturation and USMB excitation,A and B respectively. Nuclei are stained with DAPI (blue). Note examples of lines drawn for quantification of the number of F-actin stress fibres along the width of the cell.

using a Gaussian filter with σ settled at 1.5. In this way, two neighbouring top values are considered two separate peaks only when the distance between them is equal or higher than 0.3 μm. Dividing the number of peaks by the length of the line the density of F-actin stress fibres along the width of the cell is then obtained and measured for all the 30 cells randomly selected. A mean density is finally obtained.

3.5.2 Cells directionality

For streamwise directionality evaluation of cells seeded into the microfluidic devices, under appropriate flow condition, a Fast Fourier Transform on the acquired fluorescence images (2-D FFT) is performed with ImageJ software, adopting a method previously used for determining directionality in collagen fibres [280]. Briefly, images of 3 distant locations of the vascular channel are acquired with the 20X magnification objective at both flow culture condition (0.5 and 25 μl/min), to visualized actin filaments stained with phalloidinAtto488. In Figure 3.9A an image is shown as an example. Subsequently, a 130 μm x 130 μm image crop from the middle of the channel for each location, are selected to perform the analysis, limiting wall effects (Figure 3.9B). Cropped images are then automatically

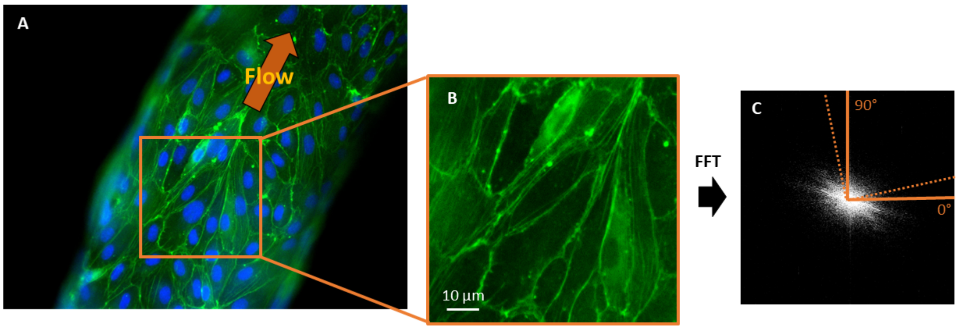

Figure 3.9: **Actin filaments directionality by frequency domain analysis. A.**One of the three 20X magnification location of the endothelium grown into the microfluidic channels and then fixed and stained for actin filaments using phalloidinAtto488 (green).**B.** 130 μm x 130 μm image crop taken from the middle of the channel in order to avoid wall effects.**C.** Corresponding fast Fourier transform (FFT) that convert the spatial domain into the frequency domain of the original micrograph.

transformed from the spatial domain to the frequency domain by performing an automated bidimensional Fourier transform in ImageJ (Figure 3.9C).

In the frequency domain, obtained by performing the 2-D FFT of the original image, the fluorescent micrograph of cells actin cytoskeleton is decomposed into a pattern of interfering directional waveforms of different intensity, frequency and direction. Since low pixel intensity and high frequency represent the fine details in the spatial domain, the transformed image is equalised to increase the contrast and exclude fine signals from the analysis of global directionality of fibres. Thus, the remaining high amplitude and low frequency waveforms represent the general structures in the spatial domain. By analysing the pixel intensity for each direction in the frequency domain image, information on the directionality of structures in the original spatial image, *i.e.* F-actin stress fibres oriented in the direction of the flow, are obtained. This is made by simply dividing the FFT transformed image in 18 slices with a central angle of 10° and measuring the total pixel intensity for each slides. An angle histogram of waveform direction is then plotted. The higher the peak in the histogram, the more aligned structures are present in the spatial image.

Finally, the resulting values are normalized to the total pixel intensity.

3.5.3 Permeability measurements

Quantification of permeability(P) is performed by analysing the dye intensity change, due to the fluorescent accumulation into the tissue compartment (see subsec. 3.4.4 for the experimental procedure), as a function of time using ImageJ software. Adopting the same method reported in [223], the permeability coefficient is determined using the following expression:

$$P = \frac{1}{I_{VC,0}} \frac{V}{S} \frac{dI_{TC}}{dt} \tag{3.2}$$

where $I_{VC,0}$ is the fluorescent intensity in the vascular channel (assumed to be constant), I_{TC} is the averaged fluorescence intensity in the tissue compartment and $\frac{V}{S}$ is the ratio of the tissue compartment volume to the exchange surface.

The derivation of Equation *3.2* can be found in Appendix C. Considering that the permeability obtained with Equation *3.2* is an apparent permeability, associated with both the endothelial barrier and the PDMS porous membrane, one can isolate the effective permeability of the endothelium, P_{cell}, using

$$\frac{1}{P_{cells}} = \frac{1}{P} - \frac{1}{P_{cells-free}} \tag{3.3}$$

where P is the apparent permeability and $P_{cells-free}$ is the permeability of an empty device.

3.5.4 Gap Evaluation

In order to monitor vascular integrity, IF microscopy is here exploited following VE-Cadherin protein labelling clustered at cell-cell border. Confocal images of different portions of the endothelium are acquired using a 20X magnification objective and successively stitched together to reconstruct the whole channel. Intercellular gaps are firstly identified by inspection using the ImageJ software, creating a rectangular Region of Interest (ROI) enclosing the gap at its centre. The channel image is then post-processed by using the list of ROIs. Image histograms within each ROI are equalised in order to increase the contrast and better identify the gap. Binarization is then obtained with a threshold method using the same cut-off value for all ROIs. Finally, the gap area is quantified counting the black pixels of the central connected blob in each binarized image. An example of ROIs with the detected gaps is reported in Figure 3.10.

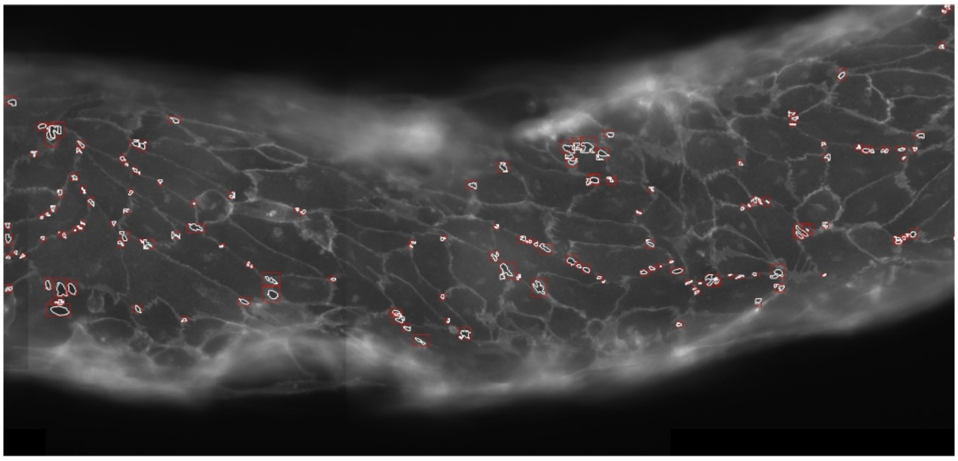

FIGURE 3.10: **Identification of gaps at cell-cell border.** Portion of endothelium showing the region of interest (ROI) in red and the gaps in white.

A histogram average of three samples for the investigated conditions (*i.e.* maturation, ultrasound excitation, MB irradiation and eventual recovery) showing the distribution of number of gaps Vs gap area, is made in order to obtain statistically valid results.

3.5.5 Statistical analysis

Statistical analysis was performed by unpaired t-tests, 99% confidence interval, using GraphPad Prism software. Comparisons between samples were considered to be statistically significant if *$p<0.05$, **$p<0.01$, ***$p<0.001$. All data are represented as means +/- SD.

Chapter 4

Experimental results and discussion

4.1 The assessment of endothelial barrier

To maintain the structural and functional integrity of blood vessels, which allows leakage of solutes and small molecules but limits the diffusion of larger molecules, vascular endothelial cells (VECs) lining vessel walls are evolved to form a size-selective barrier, consisting of specialized protein complexes called inter-endothelial adherent junctions. Not only do these junctions link the cells together, they also generate intracellular signalling and permit junctions remodelling in response to various external and internal stimuli. A main structural and regulatory molecule in endothelial junctions is vascular endothelial cadherin (VE-cadherin) that connects VECs to each other and is known to be a key component in controlling endothelium barrier function and permeability [15, 16], providing the junction backbone of the endothelium. This protein is clustered at cell-cell contacts and anchors to the actin cytoskeleton to form a dynamic protein complex whose configuration rapidly adapts to the functional state of the cell [278, 280]. Actin is the most abundant protein of the cytoskeleton. It comprises about the 10% of the total endothelial protein. Actin filaments (F-actin) polymerize from actin monomers (globular or G-actin) forming filaments between 5-7 nm and mostly appear as components of super structured protein assemblies. It plays an essential role in a cell's ability to generate and sense forces, both internally and with the outside environment [280]. This is an important aspect for many cellular processes such as the mobility and contraction of cells during cell division and migration as well as the formation and remodelling of cell-cell junctions in order to maintain endothelial integrity. Indeed, it is generally proposed that control of cell adhesion, barrier function, cell migration and angiogenesis, the physiological process through which new blood vessels form from pre-existing vessels, critically depend on the direct and indirect interaction of VE-cadherin with actin filaments, as both structures are remodelled under certain conditions [137, 281].

As already explain in Chapter 1, sec.1.6, microfluidic devices, designed to reproduce physiological shear condition, represent the unique platform able to reproduce the *in vivo* functioning of the endothelium.

Here, we present our *in vitro* endothelium model firstly showing the phenotypic characteristic of a monolayer composed of Human Umbilical Vein Endothelial Cells (HUVECs), *i.e.* confluency and maturation of adherent junctions, achieved with traditional culture system. Afterwards, we present some qualitative results concerning the assessed 3D reconstitution of the vascular tissue into the microfluidic device as well as its permeability function. A particular attention has been given to the role of physiological shear stress exerted on cells surface as a crucial aspect for a proper endothelium maturation and functional behaviour.

4.1.1 *In vitro* phenotype of endothelial cells in static condition

The morphology of HUVECs cultured *in vitro* drastically changes as they go from sub-confluence to confluence condition in order to provide the formation of a continuum endothelial monolayer with developed adherens junctions, namely the cobblestone phenotype [282]. After reaching the confluence state, even though they move much less, cell's and junction's morphology continue to change, as a dynamic structure, becoming more uniform in size and shape, as cell density increases.

The maturation of a confluent HUVECs layer, with established barrier function, is here confirmed by immunofluorescence microscopy at different culture stages, using immunolabeling visualization of VE-cadherin protein (Figure 4.1). We found

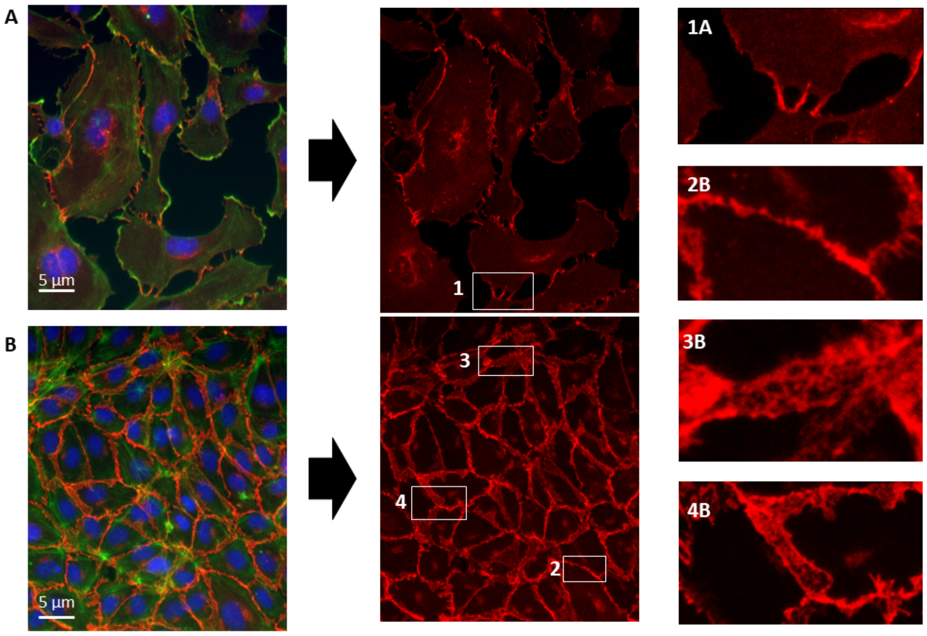

FIGURE 4.1: **Heterogeneity of endothelial junctions in HUVECs conventional cultures.** IF microscopy of sub confluent (**A**) and confluent (**A**) HUVECs stained with anti VE-Cadherin (red), PhalloidinAtto488 for actin filaments (green), and DAPI for nuclei (blue), at 1 day and 3 days of culture, respectively. Cropped areas show the diverse super-structural organization of VE-Cadherin junctions (central panels). These include interrupted patterns (**1A**), linear junctions (**2B**), reticular (**3B**) and plaque-like structures (**4B**).

that a complete HUVECs monolayer, characterized by adherent's junctions developed between neighbouring HUVECs, is obtained within 3 days of static culture in conventional wells-plates.

During the initial phase (sub-confluent conditions, Figure 4.1A cells grow, reproduce and tend to connect to each other through the plasma membrane. In these conditions, cells are larger, and their perimeter is longer than under confluent conditions (Figure 4.1B). The VE-cadherin pattern is discontinuous and formed by multiple short linear elements projecting normally from the cell border toward the neighbouring one (cropped area 1A). Once cell contact is achieved, VE-cadherin clusterization takes place, providing a well-established, resting confluent state whit cells assuming a polygonal shape. At this stage, VE-cadherin labelling exhibits a wide heterogeneity of morphologies ranging from linear, reticular or plaque-like structures (cropped areas 2,3,4B) as expected of a tight cobblestone monolayer

[282]. Under this condition, vascular stability, e.g. contact inhibition of growth, endothelial integrity and reduced loss of cells, are observed as discussed in [283].

During endothelium maturation, cell migration is coordinated by a complex of proteins that localize to adhesion sites of cell–matrix interaction, namely the focal adhesions (FAs) [284]. These sub-cellular structures are devoted to anchor VECs to the underlying substrate. Adhesion is modulated by the engagement and clustering of transmembrane adhesion receptors, such as integrins. The key function of integrins is the recruitment of proteins that link the adhesion receptor to the actin cytoskeleton [285]. While many proteins are involved, vinculin, a cytoplasmic protein enriched at both cell–cell and cell–matrix adhesions, is one of the best characterized. Vinculin regulates adhesion by directly binding the actin cytoskeleton and the cell surface to the underlying substrate [286], stimulating actin filaments polymerization and remodelling. By signalling cascades, vinculin transmits mechanical signals from the extracellular environment, allowing VECs to change shape and move in response to these signals [287]. In the absence of vinculin, cell–matrix and cell–cell adhesion is dramatically impaired, indicating that vinculin plays a critical role in vascular functionality.

We examined the formation of focal adhesion in HUVECs after 3 days of culture into pre-treated culture wells-plates. When cultured under these conditions, cells show a readily visible signal projection at plasma membrane edge, indicating that they have attached to the flat surface of the pre-treated plate (Figure 4.2).

4.1.2 Vessel-on-a-chip characterization

As the vasculature is involved in various fundamental physiological phenomena and is closely related to the inefficiency of many clinical therapies since it acts as a barrier for drug delivery, it is imperative that substantial research is conducted on characterizing the vascular functionality and investigate the mechanism behind its enhanced permeability.

The vascular channel in our system is illustrated in Figure 4.3 showing a composite brightfield picture of the endothelium reconstructed from several high-resolution images (20X magnification, 1940x1460 px). HUVECs are seeded into

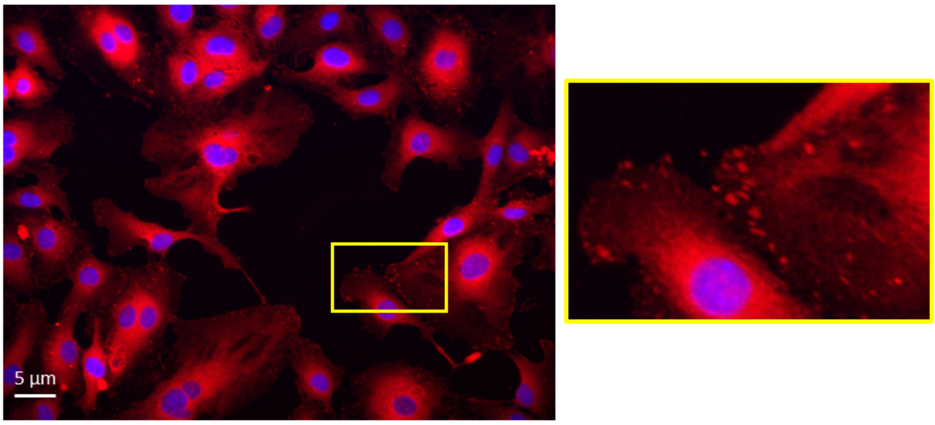

FIGURE 4.2: **Vinculin localization in HUVECs.**Wide-field fluorescence signal projections of vinculin (red) in HUVECs grown on a flat pre-treated culture dish. Nuclei are stained with DAPI (blue).

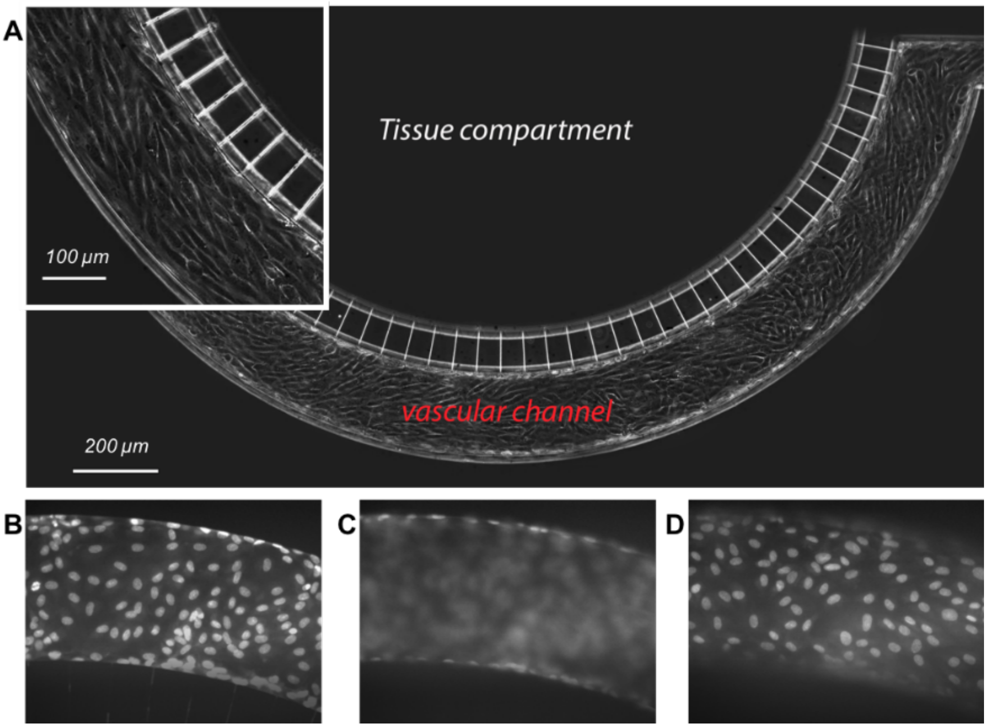

FIGURE 4.3: **Vessel-on-a-chip.** **A.** Brightfield image of HUVECs cultured in the vascular channel at physiological flow rate. The inset highlights the elongation of cells in the direction of flow. **B-D** Confocal fluorescence images of cell nuclei acquired with the confocal microscope after DAPI staining. Bottom (**panel B**, middle (**panel C**) and top (**panel D**) planes of the vascular channel.

the vascular channel as explained in Chapter 3, subsec. 3.2.2. In order to obtain a compact endothelium, the initial cells density is a crucial step. In our experiments, an initial confluence of $60 - 70\%$, optimized for HUVECs, is sufficient to obtain, after 3 days, a tight endothelium all around the PDMS wall. During maturation, the endothelium structure develops from an initial disorganized configuration to a compact endothelial layer, reaching a $90 - 95\%$ confluence inside the channel. At the final stage, the uniform endothelial layer forms a complete lumen in the channel with individual cell exhibiting the characteristic structural reorganization, whit their long axis in the direction of flow, *i.e.* from left to right.

Confocal fluorescence stack images of cell nuclei stained with DAPI, Figure 4.3B-D corresponding to three planes at the bottom, middle and top of the channel, respectively, show that the cells completely line the entire channel walls. In order to better appreciate the meaning of panel C one should recall that what is shown is a fluorescence image of a plane of the endothelial monolayer in the middle of the channel, where cells and corresponding nuclei are present only on the lateral walls of the channel. This confirms that the endothelium is perfectly adhered all around the channel section.

Staining with Calcein AM, a cell-permeant dye, confirms also cell viability (Figure 4.4). The cells exhibit a cobblestone-like configuration and are homogeneous for green fluorescence staining in the cytoplasm. Anti-Von Willebrand Factor antibody, a glycoprotein produced uniquely by VECs, is finally used as a specific endothelial cell marker (Figure 4.4, inset) since it is known that its antigen is heterogeneously distributed throughout the vasculature [288]. This analysis establishes that a uniform, three-dimensional *in vitro* endothelial barrier is formed throughout the channel section, reproducing and resembling the structure of a physiological capillary vessel.

4.1.3 The role of the physiological shear stress

Formation of stable junctions is not sufficient for a functional endothelium. The endothelial physiology is affected by numerous chemical, biological and physical factors. One of these factors is the fluid shear stress exerted on the endothelium by

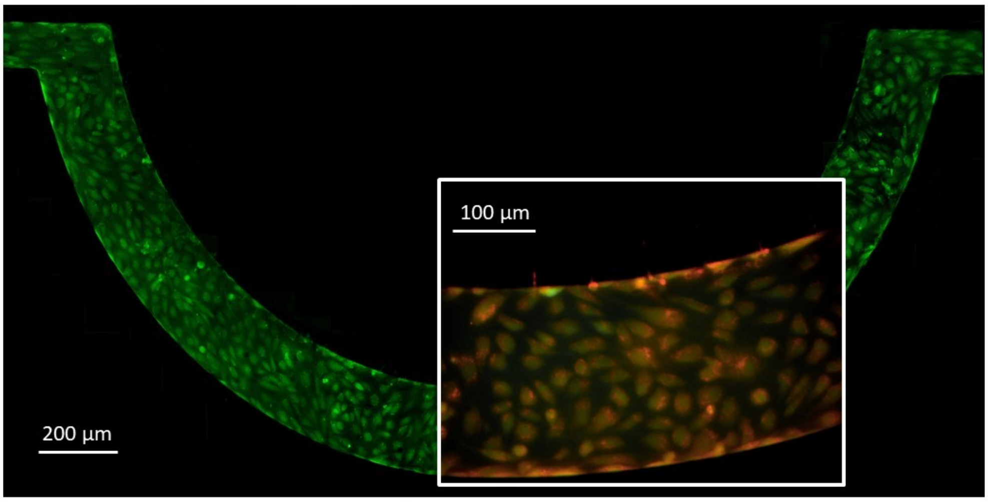

Figure 4.4: **Evaluation of cells viability.** Green fluorescence images of Calcein AM-stained HUVECs cultured inside the microfluidic device. The inset shows the fluorescence signal (red) of von Willebrand factor.

the blood flowing over its surface. When subjected to shear stresses, VECs show a varied response. The most striking one is the change in morphology, which is accompanied by extensive cytoskeletal remodelling and maturation of intercellular adherens' junction [191]. The shear stress on the cells in microvasculature under physiological conditions, typically ranging between $1-12 dyne/cm^2$ [188, 225, 226], is crucial to achieve an endothelium phenotype characterized by streamwise cell elongation and actin-mediated stabilization of junction proteins at cell-cell borders.

In conventional culture system there is a lack in reproducing such an important physiological stimulus. Without any shear applied, cells grow in a polygonal shape with no directionality and VE-cadherin forms an irregular overlapping network (see Figure 4.1). On the other hand, the microfluidic device used in this thesis, produced with soft lithography and bounded on a microscope coverslip (see Chapter 3, subsec. 3.1.2), allow us to incorporate the appropriate shear rate for a complete understanding of the role of shear stress in promoting barrier functions.

Here the goal is to investigate on the morphological changes of a continuum resting endothelial monolayer inside the PDMS channel, with the characteristically junction pathways mentioned here in subsec. 4.1.1, when applying different flow rate. HUVECs are then cultured inside the vascular channels and are subsequently subjected to different flow rates, namely low flow (0.5 μl/min) and high flow condition (25 μl/min), corresponding to a shear stress of 0.2 (nearly static) and 10 $dyne/cm^2$ (physiological level) respectively, chosen according to the channel dimensions (see Chapter 3, subsec. 3.2.3). After 3-days of culture, the vascular channels are detached from the syringe pump and are flushed with 4% paraformaldehyde (PFA) to fix the cells. Cells are then stained with phalloidinAtto488 and anti VE-Cadherin antibody for assessing the actin-mediated stabilization of junction proteins at cell-cell border (for protocol details see the Material and methods section). By monitoring changes in IF signal of actin cytoskeleton labelling at both culture conditions we also perform fast and automated image analysy methods to measure alignment and rearrangement of actin filaments as an output parameter.

Vessel-on-a-chip phenotype

IF signals of actin filaments and VE-Cadherin protein for both culture condition (0.5 - 25 μl/min), are shown in Figure 4.5.

What we found is that, increasing the shear stress exerted upon cellular surface up to the physiological level (10 $dyne/cm^2$), actin filaments remodelling does not simply induce passive changes of HUVECs shape and directionality, but is also relevant for junction formation and stabilization, promoting VE-cadherin clusterization at junction sites.

Under low flow rate, F-actin stress fibres are visible within the plasma membrane of the cell (Figure 4.5A, central panel) and VE-cadherin forms an almost irregular overlapping network (Figure 4.5A, right panel). At higher flow rate, actin filaments reorganized in a more stable configuration, called circumferential actin bundles (Figure 4.5B, central panel). VE-cadherin, driven by actin filaments, remodels into an overall linear pattern clearly sustained by actin bundles along the circumferential perimeter of the cell (Figure 4.5B, right panel), strengthening the

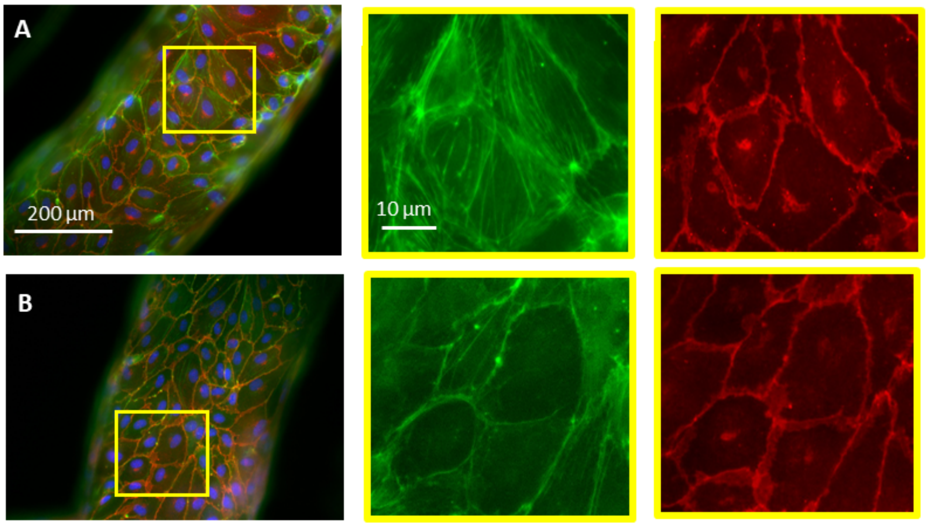

FIGURE 4.5: **Endothelium maturation**. Wide-field fluorescence images of the endothelium at $90-95\%$ confluence obtained at different flow rate. **A.** Low flow rate of 0.5 μl/min; **B.** High flow rate of 25 μl/min. **Left column**: overlay of fluorescence images showing cell nuclei (blue, DAPI), actin filaments (green, PhalloidinAtto488), cell junctions (red, VE-cadherin). **Middle column**: inset showing F-actin stress fibres. **Right column**: inset showing VE-cadherin junctions. Same scale bar is chosen for A and B (left column) and for middle and right panels.

barrier function [289]. Indeed, the circumferential actin bundles that promote and sustain cell-cell contact are characteristic for an intact resting mature endothelium *in vivo*, while stress fibres preferentially appear when endothelium become activated by internal or external stimuli, *e.g.* under inflammatory conditions and wound healing, conditions that are generally associated with cell proliferation and migration [135, 281]. In the next subsection will be elucidate such actin-driven junction stabilization process by using line scan analysis method to quantify the number of F-actin stress fibres through the cell body.

As explained in subsec. 4.1.1 focal adhesion (FAs) not only provide structural support for endothelial cell-matrix adhesion but are also signalling complexes that transmit information from the local environment allowing cells to migrate and respond to mechanical stimuli [287]. Cells lacking key proteins of FAs, such as vinculin, become more mobile and less stiff [290]. In our model, we observed that in presence of the extracellular matrix protein fibronectin, which was used to coat the channel walls, a sufficiently intense shear stress can also promote the formation of focal adhesions, leading to an overall confluent and well attached endothelium. This is supported by a visible immunostaining signal of vinculin protein on endothelial cell's surface grown into the PDMS channel at the physiological flow rate of 25 μl/min (Figure 4.6A) which firmly confirm the adhesion of the cell's basal layer to the PDMS channel wall. As shown in Figure 4.6B, immunostaining for vinculin within focal adhesion is instead absent in HUVECs cultured under low flow condition (0.5 μl/min), confirming that an appropriate flow rate is crucial also for the proper adhesion of HUVECs to the substrate.

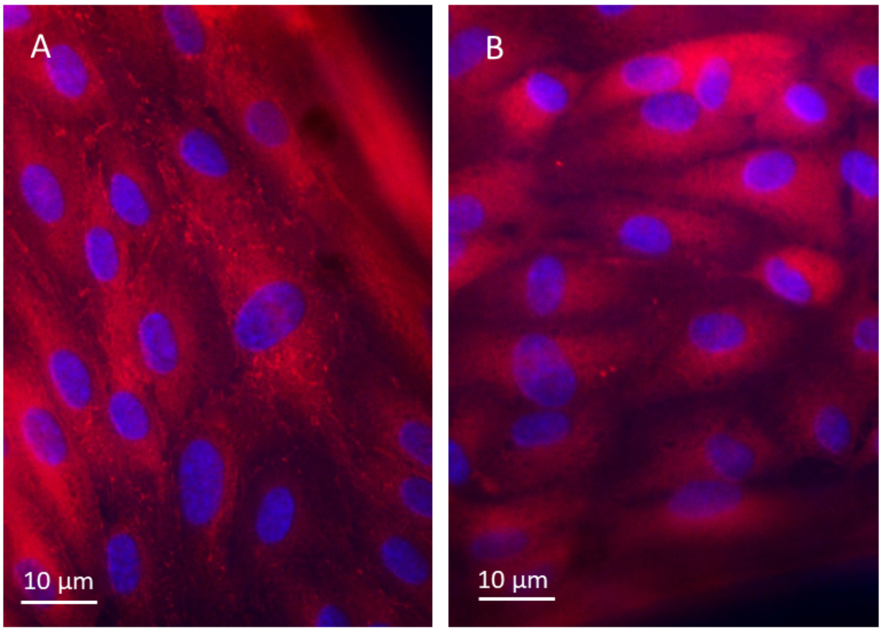

FIGURE 4.6: **Immunostaining of Vinculin within Focal Adhesion sites in HUVECs-on-a-chip** Fluorescence signal projections of vinculin (red) in HUVECs grown under (**A**) physiological flow condition (25 μl/min) or (**B**) low flow condition (0.5 μl/min). Nuclei are stained with DAPI (blue).

Actin filaments remodelling for junction stabilization

Using line scan analysis method with ImageJ software, a quantfication of F-actin stress fibres through the cell smaller axis is obtained in order to evaluate the influence of physiological shear stress in actin filaments remodelling for junction stabilization. Figure 4.7 shows the histogram, obtained as explain in Chapter

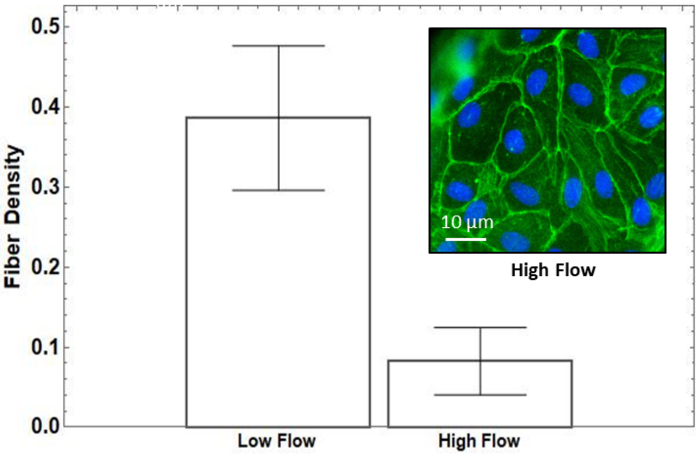

FIGURE 4.7: **Filaments actin remodelling under different flow culture condition.** Mean number of F-actin stress fibres per μm cell width. Error bars are also indicated. Inset shows representative fluorescence image of HUVECs exposed to a physiological flow rate of 25 μl/min and stained for F-actin stress fibres (green).

3, sec 3.5.1, that compares the mean F-actin stress fibres density, *i.e.* number of fluorescence peak per μm, obtained with the two flow culture conditions here investigated. By determining F-actin stress fibres density along cell width, it was found that higher shear stress caused a decrease of fibres density within the cell, suggesting a substantial rearrangement of actin filaments into the plasma membrane. Indeed, when the shear stress is increased up to the physiological level of shear stress (10 $dyne/cm^2$), actin filaments reorganize in bundle structures along the circumferential perimeter of the cells (inset in Figure 4.7) and the fibres density substantially halved compared with the lower shear stress of 0.2 $dyne/cm^2$. These findings indicate that the endothelium cultured under low flow condition is an active endothelium whose configuration is still unstable and does not guarantee a functional endothelium barrier.

Cell streamwise alignment

Following the analysis explained in Chapter 3, subsec. 3.5.2, the streamwise directionaly of cells cultured into the microfluidic device, at different flow culture condition, is evaluated (Figure 4.8A-B).

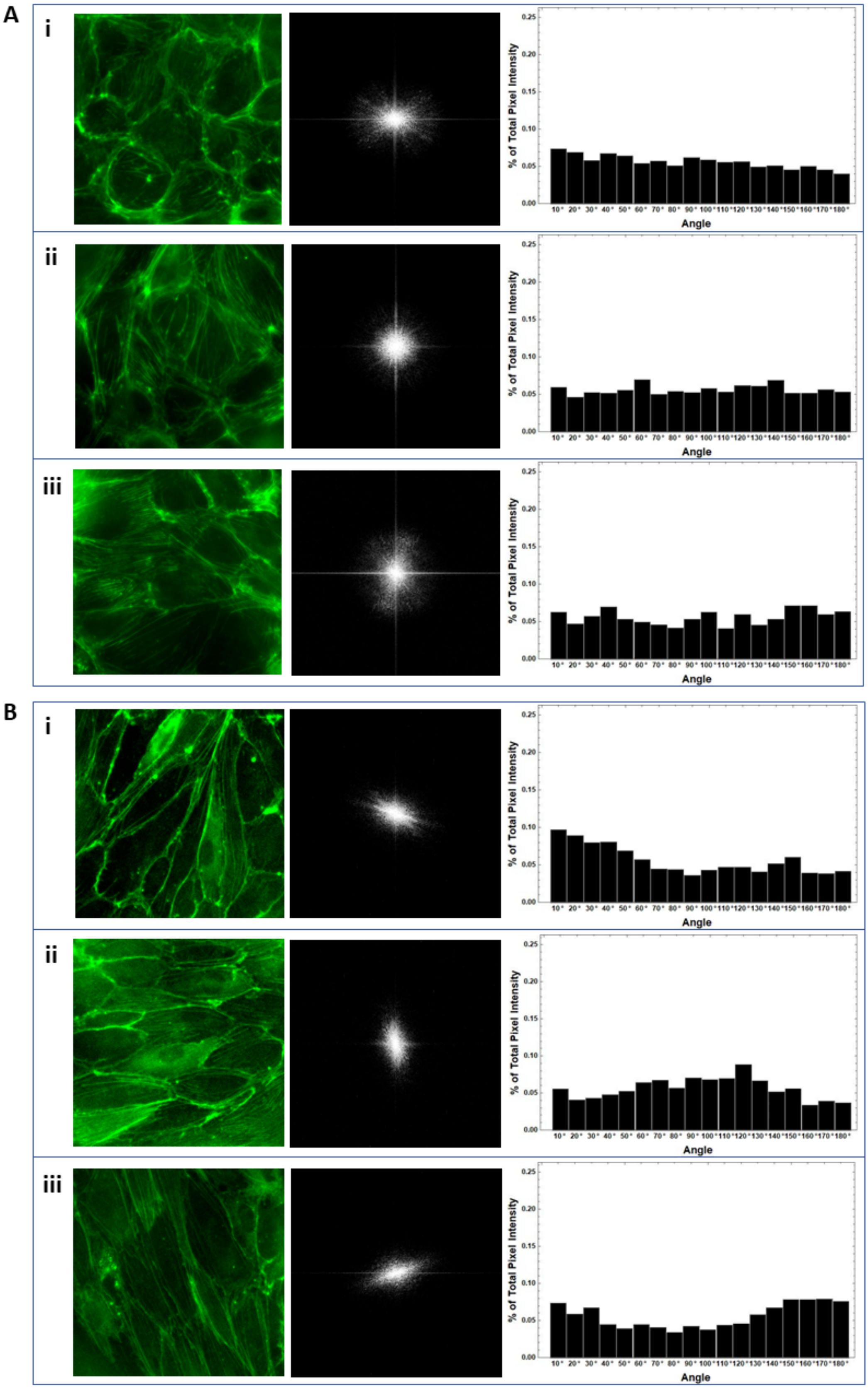

FIGURE 4.8: **Frequency domain analysis for cells streamwise alignment.** **A**. low and **B.** physiological flow culture conditions at three different location along the vascular channels (i, ii, iii). **Left column:** 130 μm x 130 μm spatial image taken from the middle of the channel stained with PhalloidinAtto488 for actin filaments (green). **Middle column:** Corresponding frequency domain obtained with the Fast Fourier transform. **Right column:** angle histogram composed of eighteen 10-degree categories.

The 2-D FFT method works by converting the fluorescent micrograph of actin cytoskeleton (spatial domain) into an interference pattern of directional waveforms with different amplitude, frequency and direction (frequency domain) (Figure 4.8A-B, central panels). In the frequency domain, each pixel represents a single wave of intensity in the original, spatial image. The distance of a pixel to the centre of the image gives the frequency of the waveform it represents (low frequency waveforms are closer to the centre). The orientation of the pixel with respect to the centre of the image gives the direction of the relative waveform. If the fluorescent micrograph contains a lot of structures with a specific direction, then there must be an over-representation of high amplitude intensity waveforms with the same direction. So, by analysing the pixel intensity for each direction (10-degree slices) in the frequency domain image, information on the directionality of structures in the original micrograph can be deduced. An angle histogram for each location of the endothelium cultured at quasi static and physiological condition is plotted in the right panels of Figure 4.8A-B respectively.

Cells grown at quasi static flow condition appear to be disorganized in a polygonal shape with no directionality. This spatial morphological aspect is highlighted by the FFT pattern in the frequency domain, where the distribution of pixel intensity is homogeneously dispersed around the centre of the image and is similar for each location along the vascular channel. The corresponding angle histograms are almost flat meaning that there is not any specific direction in the original fluorescence micrograph. On the other hand, under higher flow rate, cells tend to be orientated with the direction of the flow. This is shown in all three locations selected, where the higher peak in the angle histogram represents the preferential directionality, coherently with the curvature of the vascular channel.

Based on all these data, an exposure shear stress of 10 $dyne/cm^2$, the physiological one, is chosen for all further experiments.

4.1.4 Permeability measurements of the *in vitro* endothelial barrier

The endothelial membrane tightness is evaluated through the experimental procedure explained in Chapter 3, subsec 3.4.4. Being optically clear, the microfluidic device used here is suitable for real-time monitoring and direct measurement of endothelium permeability. Using a Harvard syringe pump, a fluorescence dye (Dextran Texas Red, 40 kDa) is injected into the vascular channel at a flow rate of 1 μl/min. In such condition, the fluorescent dye passively diffuse from the vascular channel to the tissue compartment, through the membrane of pores. As the fluorescence dextran accumulates into the tissue compartment in a time-dependent manner, permeability is estimated by measuring over time the change of the fluorescence signal with a time-lapse acquisition, settled at 1 image per minute, for a total of 120 images captured at an exposure time of 300 ms. In line with the theory (refer to Appendix C), the calculation of permeability is performed considering the intensity of the vascular channel saturated to a constant value. For this reason, the first 20 images, corresponding to the time necessary to reach saturation are discarded before calculating the permeability value.

To optimize the method for the quantification of permeability into the chip, permeation of the 40 kDa Dextran across the membrane pores is first evaluated for a cell-free microfluidic device. Afterwards, the permeability of the cell-free device was compared to the average permeability of 8 endothelium cultured into the microfluidic device at the physiological flow rate of 25 μl/min in order to statistically estimate the tightness of the biological barrier.

In Figure 4.9, the difference in fluorescence dye accumulation into the tissue compartment during time-lapse acquisition is reported for the two separates cases, *i.e.* without cells (Figure 4.9A) and with cells cultured into the channel (Figure 4.9B). As expected, a significant decrease over time of the fluorescence dye diffusion in presence of the biological barrier is observed, meaning that fluorescence's dextran extravasation into the tissue compartment is hampered by the formation of adherent junctions connecting neighbouring cells.

Typical curves of permeability experiments are presented in Figure 4.10A. For

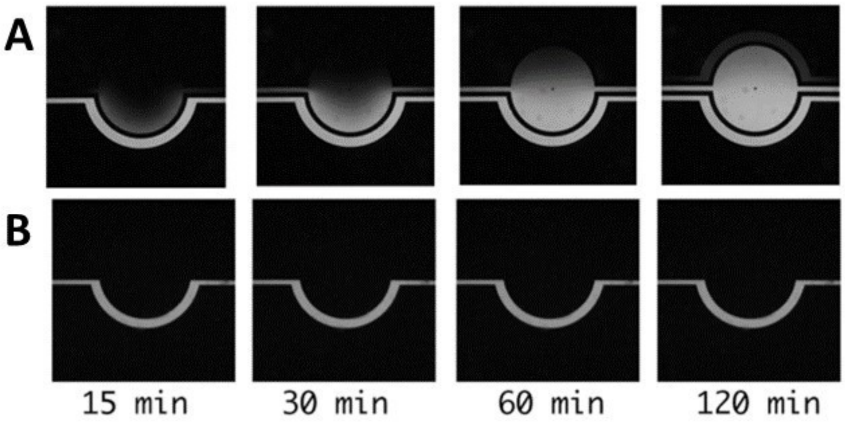

FIGURE 4.9: **Real-time fluorescence diffusion.** Images of the passage of Dextran Texas Red from the vascular channel to the tissue compartment for a cell-free device (**A**) and a cell-covered device (**A**) after 15, 30, 60, 120 minutes from the start of the flow.

both conditions, with (red curve) and without cells (blue curve), the normalized tissue compartment fluorescence intensity increases linearly with time. The slope of each curve is used to calculate the apparent and the effective permeability to dextran using respectively Equation *3.2* and *3.3* mentioned in Chapter 3 subsec. 3.5.3. Again, as expected, the estimated permeability value, averaged for 8 cell−seeded device experiments, is equal to $8.02 \cdot 10^{-8}$ cm/s, 3 order of magnitude lower than the control, *i.e.* cell−free device, that in our case is $1.25 \cdot 10^{-5}$ cm/s (Figure 4.10B).

4.2 Cell-cell junctions opening and recovery upon cavitation

In previous section, we introduced our *in vitro* model optimized to reproduce vascular geometry and simulate the appropriate range of hydrodynamic forces, *e.g.* shear stress, to achieve the essential functionality. The assessed vascular system was then used as an *in vitro* platform to elucidate the mechanism of cavitation-induced actin filaments rearrangement followed by gap formation at cell-cell borders. All the experiments here reported are performed in a microfluidic device

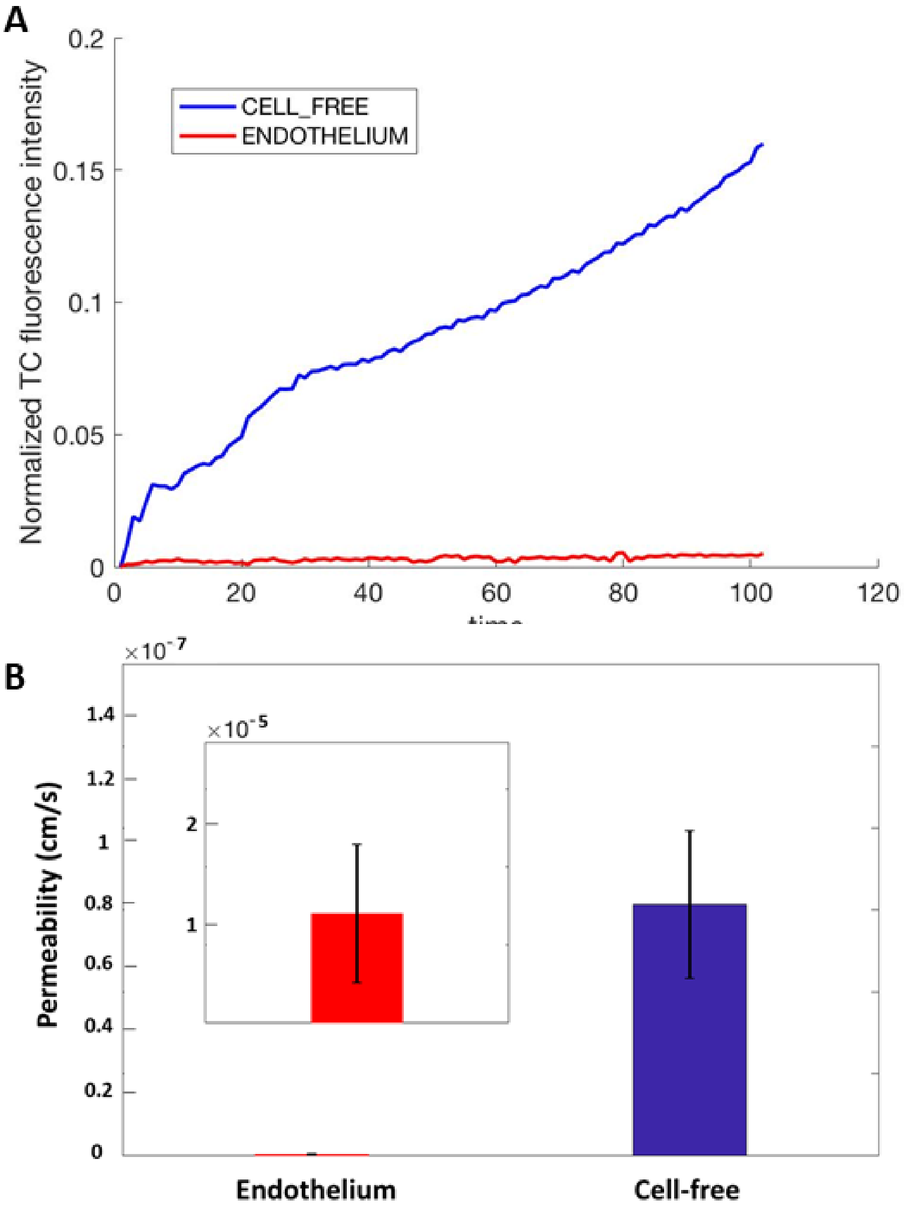

FIGURE 4.10: **Permeability measurements. A.** Example of the typical curves of permeability experiments. Comparison of normalized tissue compartment fluorescence intensity in a cell-free device (blue curve) and in a cell-covered device (red curve) for a single experiment. **B.** Permeability coefficient histograms. Error bars indicating SD are also reported

where HUVECs are grown under physiological shear stress (10 $dyne/cm^2$) unless otherwise stated, in order to guarantee barrier function established by junction stabilisation along the edge of the cell. MBs are injected into the channel and irradiated by low intensity US (0.4 and 0.72 MPa) at 1 MHz to force stable acoustic cavitation. The pressure amplitude has been indeed chosen to be below the threshold of inertial cavitation, that in our condition (Sonovue® MBs, irradiated at 1 MHz, with a pulse length PL=500 μs, pulse repetition frequency PRF = 20 Hz, total pulse number 600, fluid speed of 0.83 mm/s) is 0.82 MPa as reported in [291]. The effect of the stress exerted by MBs oscillation on the endothelium is identified by immunofluorescence staining of VE-Cadherin junctions and actin filaments to monitor the induced morphological changes. The efficacy of US at different intensity, both with and without MBs, is monitored and quantified in a highly reproducible manner at different stages of the irradiation process. With a view toward clinical application, the endothelial layer integrity recovery under different irradiation condition is also precisely quantified.

4.2.1 Microbubbles injection and US exposure

After endothelium maturation, the microfluidic chip is transferred to the custom insonication chamber, which is placed on the microscope stage, as described in Chapter 3, Subsec. 3.4.3. After 30 minutes under physiological flow condition to let the cells adopt to the new system, Sonovue® MBs are injected into the vascular channels and activated by US. The insonication protocol consists of a sequence of bursts at 1 MHz formed by 500 cycles repeated every 50 ms for a total duration of 30 s with 0.1% duty cycle (DC). As the bubble residence time over a region of the endothelium during insonication is important to induce the expected bioeffects, the perfusion rate upon US exposure is transiently reduced to 1 μl/min, corresponding to a flow velocity injection of 0.83 mm/s. Reducing the flow rate results in a more faithful reproduction of the bubbles dynamics in capillaries, where the physiological flow velocity is in the range of 0.5-1.5 mm/s [292].

Figure 4.11A shows MBs distribute homogeneously along the channel which

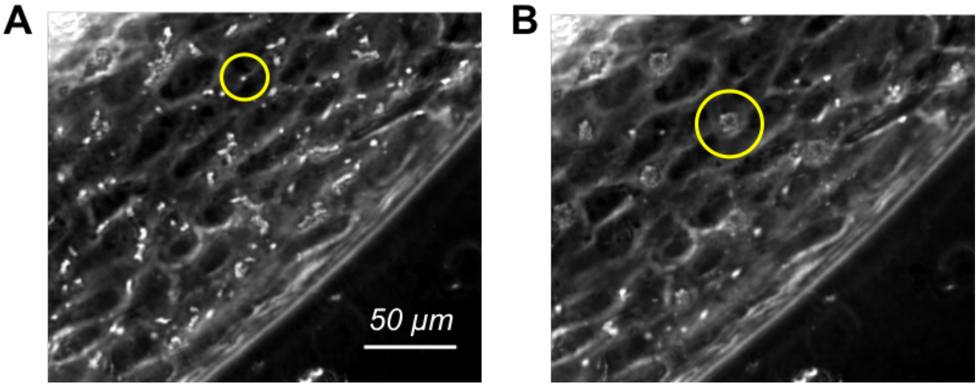

Figure 4.11: **Brightfield images showing a portion of the vascular channel with injected microbubbles. A.** MBs transported by the flow before irradiation. **B.** MB cluster formed under US-induced radiation forces. The yellow circles highlight a single bubble (A) and a cluster of bubbles (B), respectively. Same scale bar is chosen for A and B.

tend to approach the upper endothelial wall, due to buoyancy. Time-lapse imaging reveals that US radiation forces initially slow down the MBs and eventually lead to their agglomeration (see yellow circles in Figure 4.11B), resulting in spaced bubble clusters, in agreement with [269].

4.2.2 Acoustic Pressure-induced bioeffects

The efficacy of US at different intensity, namely 0.4 and 0.72 MPa Peak Negative Pressure (PNP), with and without MBs, is evaluated by monitoring the alteration of intercellular junction morphology. For this purpose, an image analysis of stained VE-cadherin (see Chapter 3, Sec. 3.3) has been developed and performed to identify the gaps present on the endothelial monolayer (located at cell-cell borders) and to quantify gaps number and their area in terms of pixels (1 pixel = $0.22 \cdot 0.22 \mu m^2$ in our imaging system). VE-cadherin was stained within 4 minutes after the end of irradiation to allow time to extract the sample from the insonication chamber and inject paraformaldehyde into the vascular channels under the biological hood. Figure 4.12A shows a regione of one vascular channel used as control with the main features already discussed here in Subsec. 4.1.1. Intercellular gaps for samples irradiated with US at 0.72 MPa PNP with no MBs and with MBs, respectively, are shown in Figure 4.12AB-C. As indicated by white arrows, local disruptions

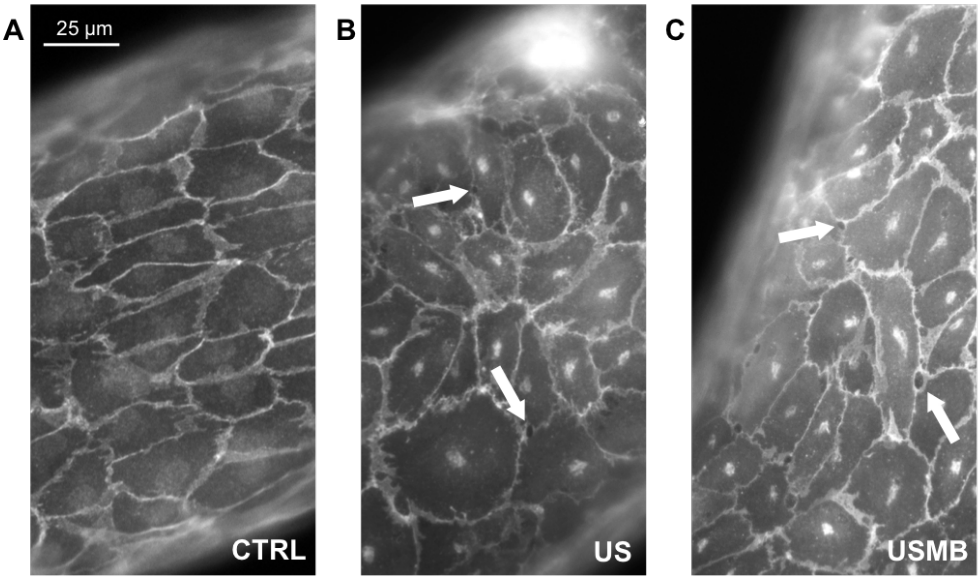

Figure 4.12: **Wide-field fluorescence images of VE-cadherin.** The samples are grown at the physiological flow rate of 25 μl/min to form a confluent rest endothelium. **A.** Untreated sample (CTRL). **B.** Ultrasound irradiated sample (US). **C.** Bubble injected ultrasound irradiated sample (USMB). The acoustic pressure is 0.72 MPa corresponding to piezo driving voltage of 140 mV. Irradiation protocol: duration 30 s, 500 cycles, frequency 1 MHz. Arrows highlight typical intercellular openings. Same scale bar is chosen for A, B and C.

of cell-cell contacts, corresponding to VE-cadherin reorganization, arise after US exposure, either acting directly on the cells, or combined with the oscillating MBs.

Histograms showing the distribution of gaps number vs gap area, averaged for 3 samples each investigated conditions (*i.e.* control, US excitation, USMB irradiation) at both pressure 0.4 and 0.72 MPa, are plotted in Figure 4.13, respectively. From the histograms, the main effect of US and USMB is the increase of gaps number, as shown by the shape of the distribution which, to a first approximation, is almost unaltered with respect to the control. The total opened area is illustrated in the insets. These findings indicate that US alone at the lower acoustic pressure, 0.4 MPa, has no substantial effect on the endothelium integrity. Increasing the acoustic pressure up to 0.72 MPa, acoustic forces alone lead to a significant increase in total opened area. The overall effects are amplified by the presence of MBs into the vascular channel. The total opened area grows, compared to US alone, by 130% at 0.72 MPa while is mildly over the US at 0.4 MPa. However, for both conditions, the increase of USMB total opened area is significant, compared

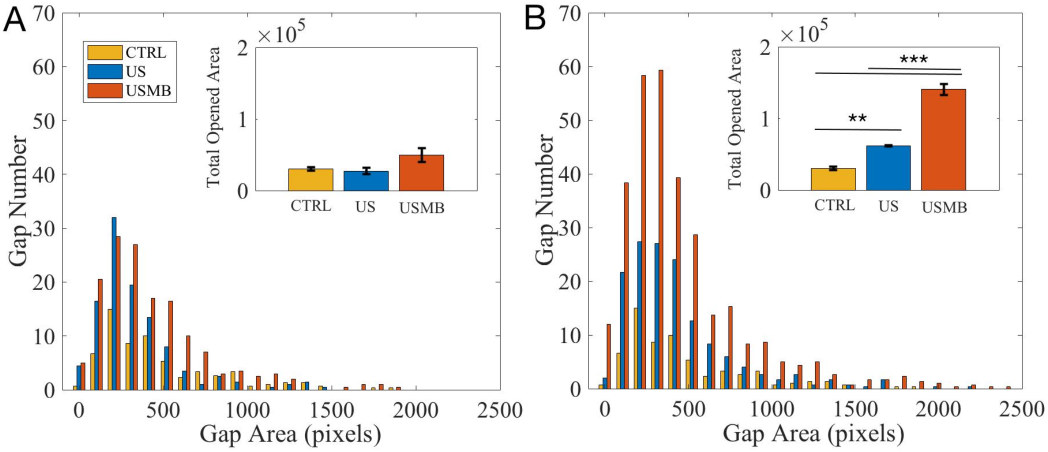

FIGURE 4.13: **Junction opening.** Number of gaps vs gap area. Comparison between untreated samples (CTRL), ultrasound irradiated samples (US) and bubble injected ultrasound irradiated samples (USMB). Area expressed in pixel where 1 pixel = $0.225 \cdot 0.225 \mu m^2$. **A.** Irradiation pressure 0.4 MPa. **B.** Irradiation pressure 0.72 MPa. CTRL vs US p=0.0053, CTRL vs USMB p=0.0004 and US vs USMB p=0.0007. The insets report for each case the total gap area over the entire vascular channel. Irradiation protocol: duration 30 s, 500 cycles, frequency 1 MHz.

with the control. Statistical significance is indicated by asterisks.

In Subsec. 4.1.3 of this Chapter we demonstrated that inter-endothelial junctions are stabilized by linkages to circumferential actin bundles which, under physiological flow condition, rearrange into a more stable configuration in support of newly junction development. By evaluating actin filaments organization into the cell, using phalloidinAtto488 staining protocol immediately after USMB exposure, we also observed that, in presence of MBs exposed to US at 0.72 MPa PNP, individual F-actin stress fibres rearrange and mainly gather at the centre of the cells (inset Figure 4.14)compared to the untreated sample where F-actin stress fibres are organized along the sides of the cells (see inset Figure 4.7.

After quantification using line scan analysis method, the histogram that compare the mean fibre density are obtained for the two conditions (Figure 4.14C). This result reinforces our statement, that after USMB exposure, an increased number of intercellular gaps appear, indicating an actin-driven changes in junction architecture with a consequent enhanced endothelial permeability.

In order to investigate on the relation between the bubble residence time and the induced bioeffect, as introdeced in Subsection 4.2.6., we explore other MBs flow

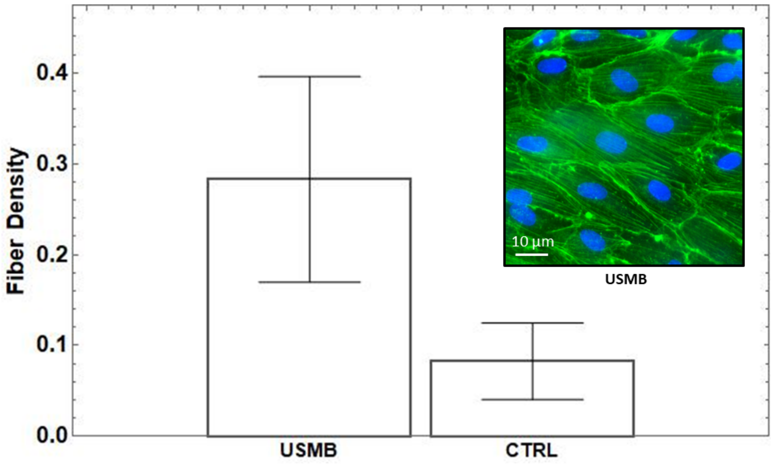

FIGURE 4.14: **Actin filaments remodelling after USMB exposure.** Mean number of F-actin stress fibres per μm cell width. Error bars are also indicated. Inset shows representative fluorescence image of HUVECs stained for F-actin stress fibres (green) 4 minutes after the application of USMB. Nuclei are stained in blue. Irradiation protocol: duration 30 s, 500 cycles, frequency 1 MHz, 0.72 MPa.

rates injection, namely 3, 5, 25 μl/min (Figure 4.15). The experiments, conducted at the maximum acoustic pressure of 0.72 MPa, highlight that the target effect, is obtained at the smaller flow rates, while at the fastest speed the residence time of the bubble is apparently insufficient to produce the desired bioeffect.

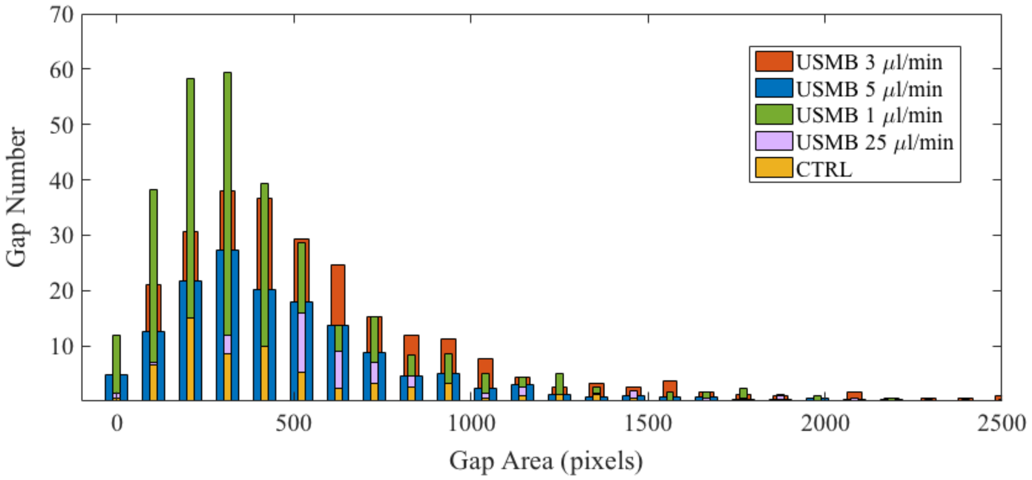

FIGURE 4.15: **Gap area histograms.** Comparison between different flow rate bubble injection during US experiment at the irradiation pressure of 0.72 MPa.

As previously verified, endothelium maturation under appropriate shear stress conditions is essential to achieve a physiological barrier. Figure 4.16A highlights

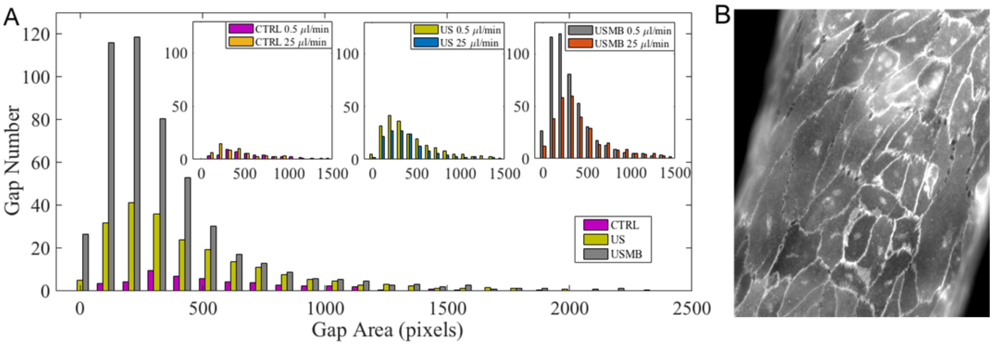

Figure 4.16: **Junction opening in the endothelium cultured at 0.5 μl/min. A.** Gap area histogram comparison between US alone and US irradiated MBs. The insets compare this flow rate with the physiological one (25 μl/min) for the control case (left), US alone (middle) and US irradiated MBs (right). **B.** VE-cadherin wide field fluorescence image of a portion of endothelium after US exposure in presence of MBs.

the effect of cavitation on an unstable endothelium cultured at a flow rate of 0.5 μl/min (shear stress of 0.2 $dyne/cm^2$). The figure shows the gap area distribution for 3 different condition: the control case, under simple US irradiation and when irradiation is applied in presence of MBs. Surprisingly, the comparison of the untreated samples with those cultured at physiological shear stress indicates that endothelium morphology is substantially the same (Figure 4.16A leftmost inset). Also, the gap area distribution for the irradiated endothelium with no MBs is similar to that found at physiological shear stress (Figure 4.16A middle inset) with the latter having a gap number and total gap area slightly larger. The rightmost inset, however, demonstrates that irradiated MBs produce a substantially massive effect on the endothelium cultured under almost static conditions, with a readily visible gap distribution increased in number, compared to the endothelium grown under relevant physiological condition. Figure 4.16B shows the fluorescence image of gaps formed in the endothelium cultured at 0.5 μl/min after MBs irradiation. These findings indicate that the unstable endothelium obtained with low flow rate culture condition is more prone to gap formation, particularly in presence of MBs. In other words, the sensitivity of the endothelium to US irradiation and MBs cavitation is significantly dependent on the culture conditions. This observation is consistent with our findings presented in SubSsec. 4.1.3, where the appropriate flow rate is found crucial also for the proper adhesion of HUVECs to the substrate.

4.2.3 The recovery of endothelial monolayer integrity

In the previous section, we found that low intensity US significantly affect endothelial monolayer integrity when MBs are present, by promoting the formation of intercellular gaps between cells. This is accompanied by actin filaments organisation over the centre of US exposed cells. Here we investigate endothelium restoration process to recover endothelial integrity by closure of gaps after US irradiation protocol.

Immediately after US exposure, the sample is placed into the incubator and perfused with the physiological shear stress of 10 $dyne/cm^2$. After 45 minutes under this condition, the microfluidic device is fixed and stained for VE-Cadherin proteins and actin filaments.

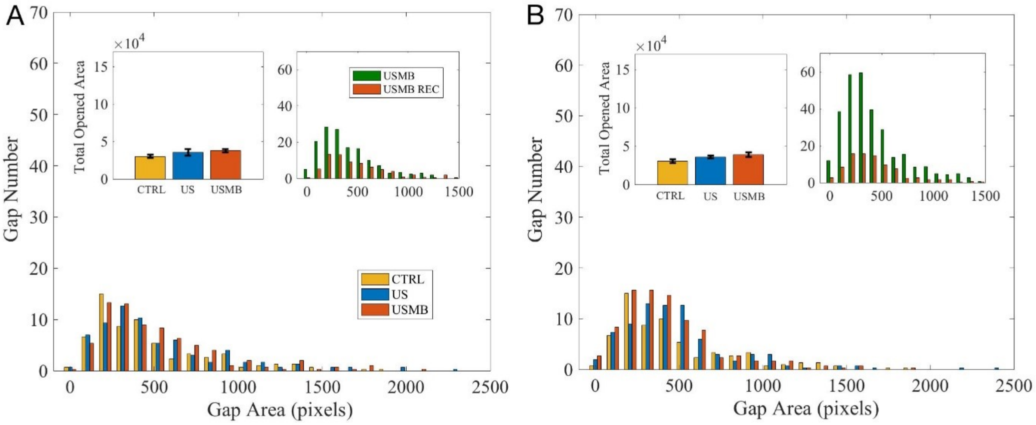

FIGURE 4.17: **Junction recovery.** Number of gaps vs gap area 45 minutes after US irradiation. Comparison between untreated samples (CTRL), ultrasound irradiated samples (US) and bubble injected ultrasound irradiated samples (USMB). **A.** Irradiation pressure 0.4 MPa. **B.**Irradiation pressure 0.72 MPa. The inset in the top left of each panel reports the total gap area in pixels. The inset at the top right compares data immediately after USMB irradiation and 45 minutes later. The irradiation protocol is the same as Figure 4.13.

As shown in Figure 4.17A-B for 0.4 and 0.72 MPa irradiation pressure, respectively, endothelium integrity is completely recovered, with gap area distributions reducing to control with no significant different between US and USMB values for both pressures. These findings indicate that the opened intercellular spaces totally close back after irradiation, confirmed by the total opened area measured after 45 minutes that highly reproduces the untreated sample (insets on the left of Figure 4.17A-B). The two insets on the right of Figure 4.17A-B provide the comparison of gap area distributions for USMB just after irradiation and after 45 minutes recovery, pointing out that the cells can overcome the USMB-evoked cellular bioeffects even at the higher irradiation pressure.

After quantification of F-actin stress fibres, it was also found that the fibres density returned to the control level when the cells are fixed 45 minutes after US exposure (Figure 4.18), indicating that the gaps closure is accompanied by the remodelling of actin filaments into the more stable circumferential actin bundles, supporting junctions stabilization.

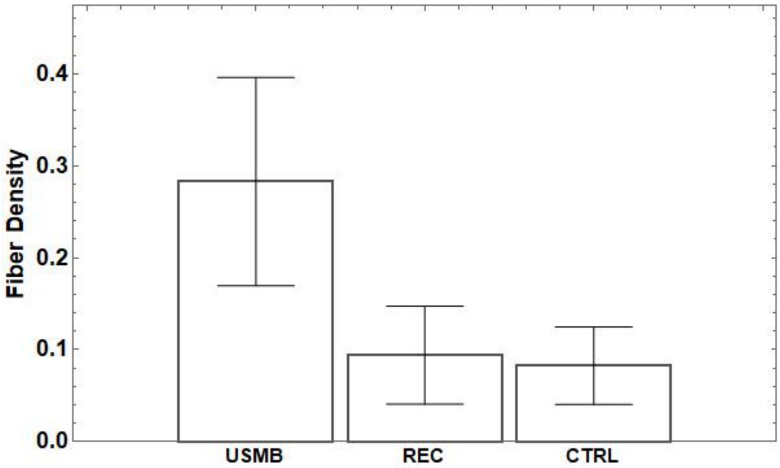

FIGURE 4.18: **Fibres density comparison. (USMB)** Cells fixed 4 minutes after US irradiation in presence of MBs. Irradiation protocol: duration 30 s, 500 cycles, frequency 1 MHz, 0.72 MPa. **(REC)** Cells fixed after 45 minutes from USMB exposure with the same irradiation protocol. **(CTRL)** Cells exposed to a physiological flow rate of 25 μl/min and used as a control.

In addition, data collected after 15 minutes US exposure at 0.72 MPa in presence of MBs (Figure 4.19) show that the gaps closure is not concluded yet, suggesting that the recovery is still in progress and entirely complete within a time frame of 30 minutes, in agreement with the results of [134].

4.2.4 The enhanced permeability: preliminary results

Using the experimental protocol explained in Chapter 3, Subsec. 3.4.4 and previously used to evaluate the endothelial membrane tightness, preliminary results on

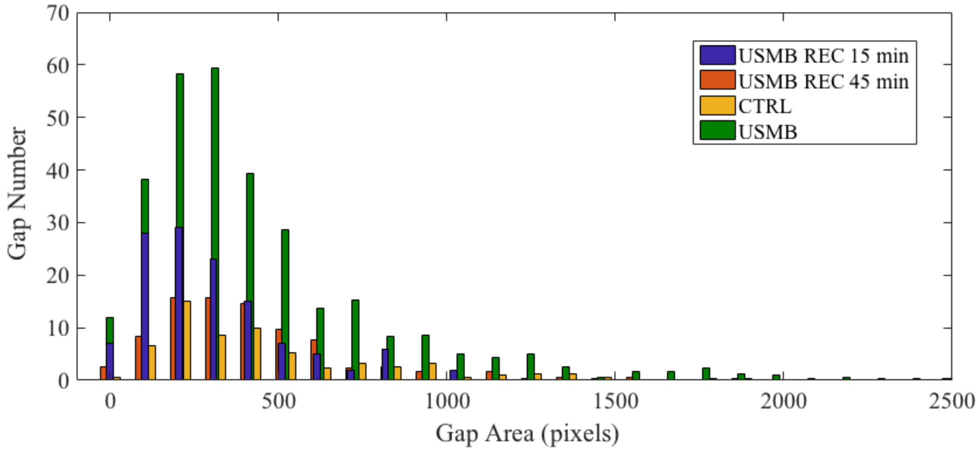

FIGURE 4.19: **Comparison of samples at different time recovery.** The histogram shows the comparison between the untreated sample (yellow profile), bubble injected US irradiated sample (green profile) at 0.72 MPa with an irradiation protocol same of figure 4.13 and recovered samples after 15 (blue profile) and 45 (red profile) minutes from exposure.

cavitation enhanced endothelial permeability are here presented. For the quantification of permeability in presence of USMB, SonoVue® are diluted at the proper concentration within the fluorescence dye solution and injected at 1 μl/min into the cell-covered channel, to let the MBs being stimulated into motion upon US exposure during a time-lapse acquisition. Details on the diffusion experiments are reported in Figure 4.20.

. The figure reports the time evolution over 2 hours of fluorescence intensity diffused in the tissue compartment from the vascular channel across the endothelium. We recall that the vascular channel communicates through a porous membrane with the tissue compartment. From these preliminary results several observations can be made. A residual permeability is present in the control sample, as expected from the gap's distribution in Figure 4.13, but still performs its function as physiological barrier, as seen by comparing with the blue curve (Figure 4.20, comparison between free-cell(blue) and control(red)). When the endothelium is subjected to the MBs oscillation upon US exposure (green curve), gaps at cell-cell border form and the permeability substantially increase with respect to the control. After 60 minutes from the irradiation protocol, the endothelium recovers the permeability profile of the control in line with what has been found with the gap distribution

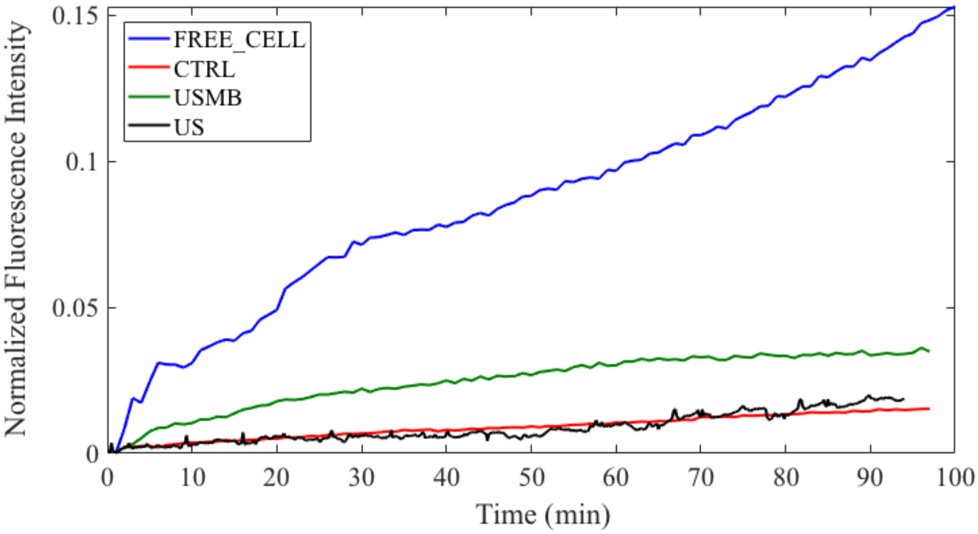

FIGURE 4.20: **Preliminary results of the enhanced permeability upon USMB exposure.** The dye is perfused in the vascular channel and diffuse into the tissue compartment through the porous membrane. Data in blue concern the device with no endothelium (cell-free), data in green, concern the endothelium upon USMB exposure while the black curve indicates the endothelium upon US exposure alone. Finally, data in red represents the control sample, meaning the intact untreated endothelium. Sonovue® MBs are injected into the vascular channel and activated at time t=0 by the same irradiation protocol of Figure 4.13.

analysed after 45 minutes from USMB exposure (see Figure 4.17). Data of fluorescence accumulation into the tissue compartment, collected when the endothelium is exposed only to US (black curve), indicates that US irradiation alone is insufficient to permeabilize the endothelium, meaning that the irradiation level is such that no damage is induced without MBs injection. We like to stress that in gaps evaluation experiment, when quantifying the opened gap area, we do observe a slight direct effect of US alone. This slight difference, although perfectly reproducible (see Figure 4.13) is insufficient to be directly detected in terms of dye diffusion in our system (see Figure 4.20). For this reason, more experiments need to be addressed in order to obtain statistically valid results.

Chapter 5

Conclusions

Cavitation is a central topic in many scientific fields since its destructive power has been revealed. In drug delivery application, MBs activated by controlled intensity US are used as a non-invasive therapeutic strategy to increase the local permeabilization of biological barriers, facilitating drug passage. Different mechanical action may be at work to explain why MBs induce endothelium integrity alteration via a cascade of cellular responses. In the classical view, stable MBs oscillation induce microstreaming and related shear stresses at the vessel wall that are transmitted to the junction, which tight together endothelial cells, while inertial cavitation leads to a more intense forcing through shock wave emitted at bubble collapse and associated micro-jetting. All these mechanical actions may induce the dynamic opening and closure of inter-endothelial junctions by actin cytoskeleton remodelling thus introduce reversable interruption of the endothelial layer continuity. Since now, a crucial issue is the assessment of the biological effects induced by MBs cavitation, which is especially difficult to achieve *in vivo*. From the clinical point of view, potential hazard posed by US irradiation, *e.g.* bleeding, apoptosis and necrosis, is a crucial aspect. Although clinical protocols are not yet available, a rich literature describes promising results in this direction using *in vivo* models. In this contest *in vitro* platforms, designed to mimic vascular geometry and the appropriate range of hydrodynamic forces, have emerged as a significant advancement for drug delivery studies. The platform proposed in this thesis combines the vessel-on-a-chip system with controlled MBs injection and US irradiation providing a new and original methodology for the quantitative understanding of cavitation assisted drug delivery. A long protocol made of cells culture, device surface functionalization and cells seeding under flow condition was developed in order to realize an *in vitro* micro-vessel, reproducing the physiological features of an *in vivo* vasculature. Imaging with immunofluorescence microscopy, for adherent junction (VE-Cadherin) and actin filaments proteins visualization, were used to assess endothelium maturation and functionality validating the protocols. The flow-induced shear stress on the endothelium was found to crucially affects intercellular junction strength, with the physiological level of shear stress determining the proper morphology of VE-Cadherin an actin cytoskeleton. At the final stage of 3 days of physiological culture condition, the continuum endothelial monolayer formed a complete lumen in the PDMS channel with individual cell exhibiting the characteristic junction pathways and structural reorganization, with their long axis in the direction of flow. Using Calcein-AM and vWF staining, the confluence, viability and health of endothelial cells were also investigated. The endothelium permeability was measured by the quantification of fluorescent dye diffusion across the biological membrane revealing that fluorescence's dextran passage was hampered by the formation of adherent junctions connecting neighbouring cells.

The vessel-on-a-chip was then exploited to quantify the effect of stable cavitation on the reversable opening of inter-endothelial junctions. Actin filaments reorganization across the cell body upon USMB irradiation was also monitored. A dedicated water-filled and temperature-controlled custom insonication chamber was designed to host the bioinspired device and allow for the propagation of US waves. After Sonovue® MBs injection into the artificial vasculature low intensity US (0.4 MPa and 0.72 MPa) at 1 MHz was applied to force stable acoustic cavitation. Following VE-Cadherin labelling at different stage of the experiment (*i.e.*US excitation, USMB irradiation and eventual recovery) the response of junctions to USMB was assessed. Although US alone was able to open gaps in the mature endothelium, the presence of MBs excited by US at resonance conditions largely amplified the effect increasing opened gap number. Interestingly, the gap area distribution seemed to be proportional, in number and area, to the magnitude of the applied acoustic field, with the total gap area increasing by 360% when the pressure was increase up to 0.72 MPa respect to the untreated endothelium. These results were reinforced with image analysis of F-actin stress fibres which were found to distribute across the plasma membrane immediately after USMB exposure indicating an actin-driven changes in junction architecture with a consequent enhanced endothelial permeability. An additional observation was that endothelium cultured under insufficient shear stress intensity, lower than the physiological level, was more prone to gap formation, particularly in presence of MBs, suggesting that the sensitivity of the endothelium to US irradiation and MB cavitation significantly depend on the culture conditions. Most important, endothelium restoration process to recover endothelial integrity by closure of gaps was monitored at different time, namely 15 and 45 minutes after USMB irradiation protocol at both pressures. The effect of stable MBs cavitation was found to be transient and completely reversable within a time frame of 30 minutes. Preliminary results of fluorescence dye diffusion across the biological barrier upon USMB irradiation showed that the permeability profile substantially increase with respect to the control and recovers its profile within 60 minutes. However, more experiments need to be addressed in order to obtain statistically valid results. In summary, all the presents results demonstrate how permeabilization can be achieved in controlled and reproducible conditions paving the way to new detailed studies on the physical and biological mechanisms underlaying endothelium integrity alteration. In perspective, artificial platform like the one developed here, may eventually help in streamlining the search for safe administration protocols in clinical application. The proposed approach could be used for preliminary assessment of potential hazards and the prevention of permanent damage to the blood vessel, however preclinical trials and *in vivo* experimentation remain the conclusive safety certification. The present system is open to further developments in different direction. The micro-device could be embedded within a phantom tissue to reproduce the irradiation condition of *in vivo* applications where HIFU (high intensity focused ultrasound) devices are used to reach inaccessible and restricted target regions. Besides, the microsystem could also be optimized including different types of drug carriers and the interaction with a variety of co-cultured tissues, *e.g.* immunological research related to cell-cell interaction in tumours. In conclusion, this work could then be considered as the preliminary starting point for further studies devoted to the development of cavitation-enhanced drug delivery protocols.

Part I

Appentices

Appendix A

Shear stress in fluids

In fluid dynamics, the Navier-Stokes equation together with the continuity equation are the fundamental governing equations of motion for viscous fluids. For an incompressible fluid of constant viscosity, the Navier-Stokes equation is:

$$\rho_L[\frac{\partial u}{\partial t} + (\mathbf{u} \cdot \nabla)\mathbf{u}] = -\nabla p + \mu_L \nabla^2 \mathbf{u} \tag{A.1}$$

And the continuity equation is:

$$\nabla \cdot \mathbf{u} = 0 \tag{A.2}$$

where $\mathbf{u}$ is the liquid velocity, ρ_L the liquid density and μ_L its dynamic viscosity.

Any real fluids (liquids and gases included) moving along a solid boundary will incur a shear stress at that boundary. The no-slip condition for viscous fluids assumes that at a solid boundary, the fluid will have zero velocity relative to the boundary; although at some height from the boundary the flow speed must equal that of the fluid. The region between these two points is named the boundary layer.

For a Newtonian fluid, the shear stress at a surface element, parallel to a flat plate, at the point y is given by:

$$\tau(y) = \mu \frac{\partial u}{\partial y} \tag{A.3}$$

where y is the height above the boundary.

More specifically, the wall shear stress is defined as:

$$\tau = \theta(y=0) = \mu \frac{\partial u}{\partial y}|_{y=0} \tag{A.4}$$

By simplifying and rearranging terms in Navier-Stokes equations, for a fluid flowing between two stationary parallele plates, one can write

$$\frac{d^2u}{dy^2} = \frac{1}{\mu}\frac{dP}{dx} \tag{A.5}$$

where $\frac{dP}{dx}$ is the pressure gradient parallel along the plates.

Integrating twice and applying boundary condition, the equation yields to the parabolic velocty distribution

$$u = \frac{1}{2\mu}(\frac{dP}{dx})[(\frac{h}{2})^2 - y^2] \tag{A.6}$$

By integrating over the height of the chamber, h, and refering to equation A.3, we can express shear stress between stationary parallel plates as a function of volumetric flow of the fluid, Q, as

$$\tau_{wall} = \frac{6\mu Q}{bh^2} \tag{A.7}$$

where τ_{wall} is the shear stress at the plate where the endothelial cells are located. This equation is used to determine the magnitude of shear stress within the microfluidic device.

Appendix B

The sound filed

The sound field generated by a flat piezoelectric transducer is divided into two zones; the near field and the far field. The near field is the region directly in front of the plane transducer surface where the pressure amplitude goes through a series of maxima and minima, due to the finite edge of the piezoelectric crystal that produces diffraction phenomena [293]. At distance N the pressure variation ends with the last maximum and gradually drops to zero. The far field is the area beyond N where the acoustic pressure shows this behaviour. The location of the last maximum is known as the near field distance (N) and is the natural focus of the transducer. It can be found using the following equation

$$N = \frac{D^2}{4\lambda} \tag{B.1}$$

where D is the transducer diameter and λ the wavelength of the acoustic wave. As the acoustic beam progresses into the far field, its topology becomes much smoother, eventually evolving into a well-defined single main lobe with low-intensity side lobes [293]. Indeed, at the transition distance N, the beam changes its character from nearly collimated edges to a diverging one. This progressive spreading of the beam width for an unfocused transducer is reported in Figure B.1.

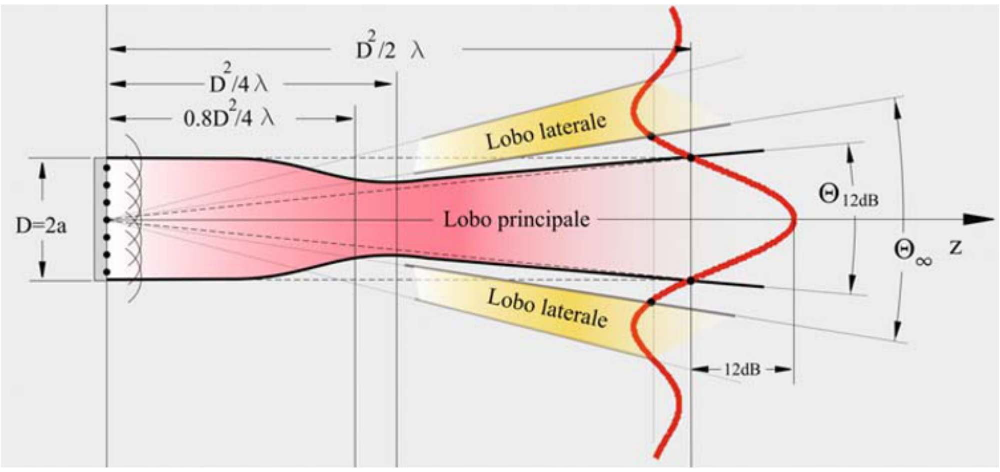

FIGURE B.1: **Characterization of an unfocused transducer.** Identification of near and far field regions by specific experiments conducted by Branca et al. [326]. In the near field, also known as the Fresnel region, the beam is nearly collimated until it approaches the transition distance N. At this point the beam changes its character into a diverging edge.

Appendix C

Permeability of a membrane

We seek here for the expression of the permeability of a porous membrane separating two compartments as the ones represented in Figure C.1. In the following, the vascular channel and the tissue compartments will be called respectively compartment 1 and 2. We refer to the fluorescent molecule that diffuses through the pores as the chemical specie A and water the chemical species B. In general the

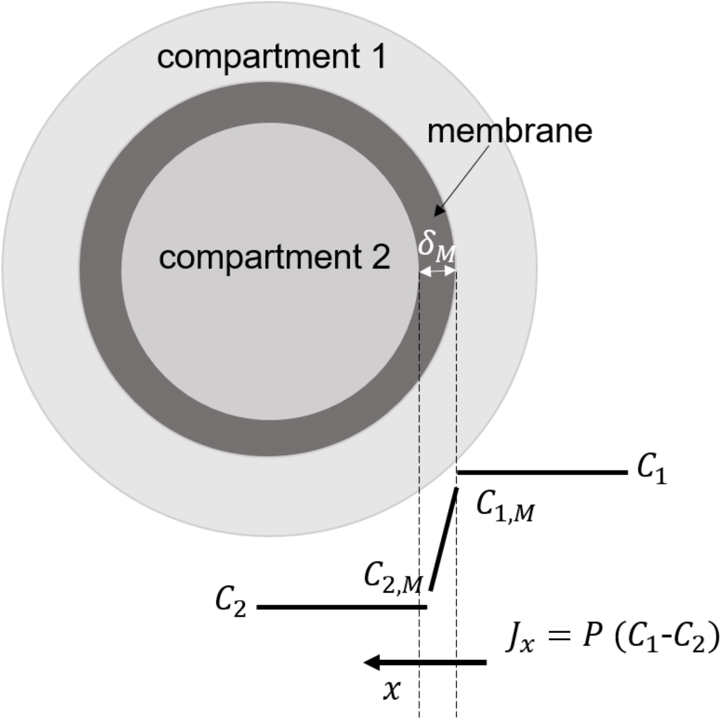

FIGURE C.1: Diffusion of a chemical specie in solution across a porous membrane of thickness δ_M that divides two compartments.

flux of a A across a membrane is given by the Flick's law

$$J_{x,A} = -D_{A,M}\left(\frac{\partial C_A}{\partial x}\right) \tag{C.1}$$

where $J_{x,A}$ is the 'diffusion flux' of chemical specie A in the x direction, $D_{A,M}$ is the diffusion coefficient of the chemical specie A through the membrane M, C_A is the concentration of the component A.

Assuming that the only driving force is the concentration difference and that C_A has a linear profile across the membrane Equation C.1 becomes:

$$J_{x,A} = D_{A,M}\left(\frac{C^M_{A,1} - C^M_{A,2}}{\delta_M}\right) \tag{C.2}$$

with δ_M thickness of the membrane and $C^M_{A,1/2}$ the concentrations of A in contact with the the membrane in compartment 1 and 2 respectively. The latters can be expressed as

$$C^M_{A,1} = K_P C_1 \tag{C.3}$$

and

$$C^M_{A,2} = K_P C_2 \tag{C.4}$$

with K_P the partition coefficient that measures the solubility of the component A inside the membrane and it depends on the chemical nature of the A and M as well. Let's define the permeability coefficient as the ratio between the diffusive flux of a component A through the membrane $J_{x,A}$ and the difference in its concentration in the two compartments $(C_{A,1} - C_{A,2})$:

$$P = \frac{J_{x,A}}{C_{A,1} - C_{A,2}}\,. \tag{C.5}$$

Substituting Equations C.3 and C.4 into Equation C.2, the permeability P reads:

$$P = \frac{D_{A,M} K_P}{\delta_M}\,. \tag{C.6}$$

Considering the formulation presented above, a easy way to calculate the permeability directly from the fluorescent intensity measurements is now derived.

The equation of the mass conservation for the component A in Compartment 2 is

$$V_2 \frac{dC_{A,2}(t)}{dt} = J_{A,x} S_\pi \,, \tag{C.7}$$

where S_π is the exchange surface. Substituting Equation C.5 into Equation C.7, the latter becomes

$$V_2 \frac{dC_{A,2}(t)}{dt} = P S_\pi \left(C_{A,1} - C_{A,2}(t)\right) \,. \tag{C.8}$$

From the integration of Equation C.8 with the initial condition $C_{A,2}(0) = C^0_{A,2}$, one can easily find:

$$C_{A,2}(t) = C_{A,1} - (C_{A,1} - C^0_{A,2}) \exp(-t\zeta) \,, \tag{C.9}$$

with $\zeta = (S_\pi P)/V_2$. Far from the saturation condition (thus for $t \ll \zeta^{-1}$), the concentration profile can be approximated using the first order of the Taylor's series

$$C_{A,2}(t) = C^0_{A,2} + (C_{A,1} - C^0_{A,2}) P \frac{S_\pi}{V_2} t + O\left((t\zeta)^2\right) \tag{C.10}$$

such that Equation C.9 becomes

$$\frac{dC_{A,2}(t)}{dt} = (C_{A,1} - C^0_{A,2}) P \frac{S_\pi}{V_2} \tag{C.11}$$

and

$$P = \frac{1}{(C_{A,1} - CA, 2^0)} P \frac{V_2}{S_\pi} \frac{dC_{A,2}(t)}{dt} \,. \tag{C.12}$$

If the relationship between concentration C and fluorescence intensity I is linear:

$$I(t) = \beta C(t) \,, \tag{C.13}$$

Equation C.12 can be expressed as a function of the fluorescent intensity:

$$P = \frac{V_2}{S_\pi} \frac{1}{\overline{I}_{A,1}(1 - \frac{I^0_{A,2}}{\overline{I}_{A,1}})} \frac{dI_{A,2}}{dt} \approx \frac{V_2}{S_\pi} \frac{1}{\overline{I}_{A,1}} \frac{dI_{A,2}}{dt} \,, \tag{C.14}$$

where the intensity of the fluorescent in the vascular channel is considered constant and equals $\overline{I}_{A,1}$.

Therefore, in order to calculate the permeability coefficient, the first step is to average the intensity of the fluorescent over the tissue compartment $I_{A,2}$ for each image and normalize it to the maximum intensity of fluorescent dextran in the vascular channel $\overline{I}_{A,1}$. After obtaining the curve $I_{A,2}/\overline{I}_{A,1}$ as a function of time, the slope of the curve, $(1/\overline{I}_{A,1})\,(dI_{A,2}/dt)$, is determined and multiplied by the geometric factor V_2/S_π.

Bibliography

[1] V. P. Torchilin, "Drug targeting," *European Journal of Pharmaceutical Sciences*, vol. 11, pp. S81–S91, 2000.

[2] T. M. Allen and P. R. Cullis, "Drug delivery systems: entering the mainstream," *Science*, vol. 303, no. 5665, pp. 1818–1822, 2004.

[3] K. Strebhardt and A. Ullrich, "Paul ehrlich's magic bullet concept: 100 years of progress," *Nature Reviews Cancer*, vol. 8, no. 6, pp. 473–480, 2008.

[4] F. Bosch and L. Rosich, "The contributions of paul ehrlich to pharmacology: a tribute on the occasion of the centenary of his nobel prize," *Pharmacology*, vol. 82, no. 3, pp. 171–179, 2008.

[5] A. S. Hoffman, "The origins and evolution of "controlled" drug delivery systems," *Journal of Controlled Release*, vol. 132, no. 3, pp. 153–163, 2008.

[6] J. K. Vasir and V. Labhasetwar, "Targeted drug delivery in cancer therapy," *Technology in cancer research & treatment*, vol. 4, no. 4, pp. 363–374, 2005.

[7] J. K. Mills and D. Needham, "Targeted drug delivery," *Expert Opinion on Therapeutic Patents*, vol. 9, no. 11, pp. 1499–1513, 1999.

[8] B. Wang, L. Hu, and T. J. Siahaan, *Drug delivery: principles and applications.* John Wiley & Sons, 2016.

[9] E. H. Starling, "On the absorption of fluids from the connective tissue spaces," *The Journal of physiology*, vol. 19, no. 4, pp. 312–326, 1896.

[10] S. Sukriti, M. Tauseef, P. Yazbeck, and D. Mehta, "Mechanisms regulating endothelial permeability," *Pulmonary circulation*, vol. 4, no. 4, pp. 535–551, 2014.

[11] H. Lum and A. B. Malik, "Regulation of vascular endothelial barrier function," *American Journal of Physiology-Lung Cellular and Molecular Physiology*, vol. 267, no. 3, pp. L223–L241, 1994.

[12] Y. Komarova and A. B. Malik, "Regulation of endothelial permeability via paracellular and transcellular transport pathways," *Annual review of physiology*, vol. 72, pp. 463–493, 2010.

[13] E. Dejana, "Endothelial adherens junctions: implications in the control of vascular permeability and angiogenesis.," *The Journal of clinical investigation*, vol. 98, no. 9, pp. 1949–1953, 1996.

[14] D. Vestweber, "Ve-cadherin: the major endothelial adhesion molecule controlling cellular junctions and blood vessel formation," *Arteriosclerosis, thrombosis, and vascular biology*, vol. 28, no. 2, pp. 223–232, 2008.

[15] E. Dejana, F. Orsenigo, and M. G. Lampugnani, "The role of adherens junctions and ve-cadherin in the control of vascular permeability," *Journal of cell science*, vol. 121, no. 13, pp. 2115–2122, 2008.

[16] M. Giannotta, M. Trani, and E. Dejana, "Ve-cadherin and endothelial adherens junctions: active guardians of vascular integrity," *Developmental cell*, vol. 26, no. 5, pp. 441–454, 2013.

[17] E. Vandenbroucke, D. Mehta, R. Minshall, and A. B. Malik, "Regulation of endothelial junctional permeability," *Annals of the new York Academy of Sciences*, vol. 1123, no. 1, pp. 134–145, 2008.

[18] W. M. Pardridge, "The blood-brain barrier: bottleneck in brain drug development," *NeuroRx*, vol. 2, no. 1, pp. 3–14, 2005.

[19] R. Schwartz, D. Chiu, and B. Lubin, “Plasma membrane phospholipid organization in human erythrocytes.,” *Current topics in hematology*, vol. 5, pp. 63–112, 1985.

[20] G. J. Doherty and H. T. McMahon, “Mechanisms of endocytosis,” *Annual review of biochemistry*, vol. 78, pp. 857–902, 2009.

[21] H.-K. Han and G. L. Amidon, “Targeted prodrug design to optimize drug delivery,” *Aaps Pharmsci*, vol. 2, no. 1, pp. 48–58, 2000.

[22] D. Papahadjopoulos, “Liposomes and their uses in biology and medicine,” *Ann. NY Acad. Sci.*, pp. 308–324, 1978.

[23] J. Wang, D. Mongayt, and V. P. Torchilin, “Polymeric micelles for delivery of poorly soluble drugs: preparation and anticancer activity in vitro of paclitaxel incorporated into mixed micelles based on poly (ethylene glycol)-lipid conjugate and positively charged lipids,” *Journal of drug targeting*, vol. 13, no. 1, pp. 73–80, 2005.

[24] R. Langer, “Drug delivery and targeting,” *Nature*, vol. 392, no. 6679, pp. 5–10, 1998.

[25] W. Al-Jamal and K. Kostarelos, “Liposomes: from a clinically established drug delivery system to a nanoparticle platform for theranostic nanomedicine,” *Accounts of chemical research*, vol. 44, no. 10, pp. 1094–1104, 2011.

[26] V. P. Torchilin, “Recent advances with liposomes as pharmaceutical carriers,” *Nature reviews Drug discovery*, vol. 4, no. 2, p. 145, 2005.

[27] F. Yuan, M. Leunig, S. K. Huang, D. A. Berk, D. Papahadjopoulos, and R. K. Jain, “Mirovascular permeability and interstitial penetration of sterically stabilized (stealth) liposomes in a human tumor xenograft,” *Cancer research*, vol. 54, no. 13, pp. 3352–3356, 1994.

[28] G. Kong, R. D. Braun, and M. W. Dewhirst, “Characterization of the effect of hyperthermia on nanoparticle extravasation from tumor vasculature,” *Cancer research*, vol. 61, no. 7, pp. 3027–3032, 2001.

[29] H. F. Dvorak, J. A. Nagy, J. Dvorak, and A. Dvorak, “Identification and characterization of the blood vessels of solid tumors that are leaky to circulating macromolecules.,” *The American journal of pathology*, vol. 133, no. 1, p. 95, 1988.

[30] M. P. Stewart, A. Sharei, X. Ding, G. Sahay, R. Langer, and K. F. Jensen, “In vitro and ex vivo strategies for intracellular delivery,” *Nature*, vol. 538, no. 7624, p. 183, 2016.

[31] M. R. Prausnitz, “Microneedles for transdermal drug delivery,” *Advanced drug delivery reviews*, vol. 56, no. 5, pp. 581–587, 2004.

[32] G. Peruzzi, G. Sinibaldi, G. Silvani, G. Ruocco, and C. M. Casciola, “Perspectives on cavitation enhanced endothelial layer permeability,” *Colloids and Surfaces B: Biointerfaces*, vol. 168, pp. 83–93, 2018.

[33] K. Kooiman, H. J. Vos, M. Versluis, and N. de Jong, “Acoustic behavior of microbubbles and implications for drug delivery,” *Advanced drug delivery reviews*, vol. 72, pp. 28–48, 2014.

[34] E. Unger, T. Porter, J. Lindner, and P. Grayburn, “Cardiovascular drug delivery with ultrasound and microbubbles,” *Advanced drug delivery reviews*, vol. 72, pp. 110–126, 2014.

[35] J. R. Lindner, “Microbubbles in medical imaging: current applications and future directions,” *Nature reviews Drug discovery*, vol. 3, no. 6, p. 527, 2004.

[36] E. C. Unger, T. O. Matsunaga, T. McCreery, P. Schumann, R. Sweitzer, and R. Quigley, “Therapeutic applications of microbubbles,” *European journal of radiology*, vol. 42, no. 2, pp. 160–168, 2002.

[37] K. Ferrara, R. Pollard, and M. Borden, “Ultrasound microbubble contrast agents: fundamentals and application to gene and drug delivery,” *Annu. Rev. Biomed. Eng.*, vol. 9, pp. 415–447, 2007.

[38] Y. Negishi, Y. Endo-Takahashi, and K. Maruyama, “Gene delivery systems by the combination of lipid bubbles and ultrasound,” *Drug discoveries & therapeutics*, 2016.

[39] E. Konofagou, “Optimization of the ultrasound-induced blood-brain barrier opening. theranostics. 2012; 2 (12): 1223–37,” tech. rep., Epub 2013/02/06. doi: 10.7150/thno. 5576 PMID: 23382778.

[40] T. Sun, G. Samiotaki, S. Wang, C. Acosta, C. C. Chen, and E. E. Konofagou, “Acoustic cavitation-based monitoring of the reversibility and permeability of ultrasound-induced blood-brain barrier opening,” *Physics in Medicine & Biology*, vol. 60, no. 23, p. 9079, 2015.

[41] E. Stride and C. Coussios, “Nucleation, mapping and control of cavitation for drug delivery,” *Nature Reviews Physics*, p. 1, 2019.

[42] L. E. Kinsler, A. R. Frey, A. B. Coppens, and J. V. Sanders, “Fundamentals of acoustics,” *Fundamentals of Acoustics, 4th Edition, by Lawrence E. Kinsler, Austin R. Frey, Alan B. Coppens, James V. Sanders, pp. 560. ISBN 0-471-84789-5. Wiley-VCH, December 1999.*, p. 560, 1999.

[43] D. A. Benwell and S. H. Bly, “Sources and applications of ultrasound,” in *Ultrasound*, pp. 29–47, Springer, 1987.

[44] K. Dussik, “On the possibility of using ultrasound waves as a diagnostic aid,” *Neurol Psychiat*, vol. 174, pp. 153–168, 1942.

[45] G. Clement, “Perspectives in clinical uses of high-intensity focused ultrasound,” *Ultrasonics*, vol. 42, no. 10, pp. 1087–1093, 2004.

[46] B. C. of the American Institute of Ultrasound in Medicine, “American institute of ultrasound in medicine consensus report on potential bioeffects of

diagnostic ultrasound: Executive summary," *Journal of Diagnostic Medical Sonography*, vol. 27, no. 1, pp. 3–13, 2011.

[47] S. J. Warden, R. K. Fuchs, C. K. Kessler, K. G. Avin, R. E. Cardinal, and R. L. Stewart, "Ultrasound produced by a conventional therapeutic ultrasound unit accelerates fracture repair," *Physical Therapy*, vol. 86, no. 8, pp. 1118–1127, 2006.

[48] J. E. Kennedy, "High-intensity focused ultrasound in the treatment of solid tumours," *Nature reviews cancer*, vol. 5, no. 4, p. 321, 2005.

[49] D. L. Miller, N. B. Smith, M. R. Bailey, G. J. Czarnota, K. Hynynen, I. R. S. Makin, and B. C. of the American Institute of Ultrasound in Medicine, "Overview of therapeutic ultrasound applications and safety considerations," *Journal of Ultrasound in Medicine*, vol. 31, no. 4, pp. 623–634, 2012.

[50] L. D. Johns, "Nonthermal effects of therapeutic ultrasound: the frequency resonance hypothesis," *Journal of athletic training*, vol. 37, no. 3, p. 293, 2002.

[51] M. Dyson, "Mechanics involved in therapeutic ultrasound," *Phisiotherapy*, vol. 73, pp. 116–120, 1987.

[52] L. Love and F. Kremkau, "Intracellular temperature distribution produced by ultrasound," *The Journal of the Acoustical Society of America*, vol. 67, no. 3, pp. 1045–1050, 1980.

[53] W. L. M. Nyborg, E. B. Surles, *et al.*, "Physical mechanisms for biological effects of ultrasound," 1978.

[54] J. A. Rooney and W. L. Nyborg, "Acoustic radiation pressure in a traveling plane wave," *American Journal of Physics*, vol. 40, no. 12, pp. 1825–1830, 1972.

[55] A. P. Sarvazyan, O. V. Rudenko, and W. L. Nyborg, "Biomedical applications of radiation force of ultrasound: historical roots and physical basis," *Ultrasound in medicine & biology*, vol. 36, no. 9, pp. 1379–1394, 2010.

[56] F. L. Lizzi, R. Muratore, C. X. Deng, J. A. Ketterling, S. K. Alam, S. Mikaelian, and A. Kalisz, "Radiation-force technique to monitor lesions during ultrasonic therapy," *Ultrasound in medicine & biology*, vol. 29, no. 11, pp. 1593–1605, 2003.

[57] S. Mitragotri, "Healing sound: the use of ultrasound in drug delivery and other therapeutic applications," *Nature reviews Drug discovery*, vol. 4, no. 3, p. 255, 2005.

[58] S. Hernot and A. L. Klibanov, "Microbubbles in ultrasound-triggered drug and gene delivery," *Advanced Drug Delivery Reviews*, vol. 60, no. 10, pp. 1153 – 1166, 2008. Ultrasound in Drug and Gene Delivery.

[59] P. Qin, T. Han, C. Alfred, and L. Xu, "Mechanistic understanding the bioeffects of ultrasound-driven microbubbles to enhance macromolecule delivery," *Journal of controlled release*, vol. 272, pp. 169–181, 2018.

[60] Y. A. Pishchalnikov, O. A. Sapozhnikov, M. R. Bailey, J. C. Williams Jr, R. O. Cleveland, T. Colonius, L. A. Crum, A. P. Evan, and J. A. McAteer, "Cavitation bubble cluster activity in the breakage of kidney stones by lithotripter shockwaves," *Journal of endourology*, vol. 17, no. 7, pp. 435–446, 2003.

[61] J. Liu, T. N. Lewis, and M. R. Prausnitz, "Non-invasive assessment and control of ultrasound-mediated membrane permeabilization," *Pharmaceutical research*, vol. 15, no. 6, pp. 918–924, 1998.

[62] K. Kooiman, M. Emmer, M. Foppen-Harteveld, A. van Wamel, and N. de Jong, "Increasing the endothelial layer permeability through ultrasound-activated microbubbles," *IEEE transactions on biomedical engineering*, vol. 57, no. 1, pp. 29–32, 2009.

[63] S. Mehier-Humbert, T. Bettinger, F. Yan, and R. H. Guy, "Plasma membrane poration induced by ultrasound exposure: implication for drug delivery," *Journal of controlled release*, vol. 104, no. 1, pp. 213–222, 2005.

[64] K. Tachibana, T. Uchida, K. Ogawa, N. Yamashita, and K. Tamura, "Induction of cell-membrane porosity by ultrasound," *The Lancet*, vol. 353, no. 9162, p. 1409, 1999.

[65] D. M. Skyba, R. J. Price, A. Z. Linka, T. C. Skalak, and S. Kaul, "Direct in vivo visualization of intravascular destruction of microbubbles by ultrasound and its local effects on tissue," *Circulation*, vol. 98, no. 4, pp. 290–293, 1998.

[66] J. Sundaram, B. R. Mellein, and S. Mitragotri, "An experimental and theoretical analysis of ultrasound-induced permeabilization of cell membranes," *Biophysical journal*, vol. 84, no. 5, pp. 3087–3101, 2003.

[67] B. Krasovitski, V. Frenkel, S. Shoham, and E. Kimmel, "Intramembrane cavitation as a unifying mechanism for ultrasound-induced bioeffects," *Proceedings of the National Academy of Sciences*, vol. 108, no. 8, pp. 3258–3263, 2011.

[68] N. McDannold, N. Vykhodtseva, S. Raymond, F. A. Jolesz, and K. Hynynen, "Mri-guided targeted blood-brain barrier disruption with focused ultrasound: histological findings in rabbits," *Ultrasound in medicine & biology*, vol. 31, no. 11, pp. 1527–1537, 2005.

[69] T. Leighton, "The principles of cavitation," *Ultrasound in food processing*, vol. 12, 1998.

[70] S. Hilgenfeldt, D. Lohse, and M. Zomack, "Response of bubbles to diagnostic ultrasound: a unifying theoretical approach," *The European Physical Journal B-Condensed Matter and Complex Systems*, vol. 4, no. 2, pp. 247–255, 1998.

[71] A. A. Doinikov and A. Bouakaz, "Acoustic microstreaming around an encapsulated particle," *The Journal of the Acoustical Society of America*, vol. 127, no. 3, pp. 1218–1227, 2010.

[72] P. Tho, R. Manasseh, and A. Ooi, "Cavitation microstreaming patterns in single and multiple bubble systems," *Journal of fluid mechanics*, vol. 576, pp. 191–233, 2007.

[73] C. P. Lee and T. G. Wang, "Outer acoustic streaming," *The Journal of the Acoustical Society of America*, vol. 88, no. 5, pp. 2367–2375, 1990.

[74] W. L. Nyborg, "Acoustic streaming near a boundary," *The Journal of the Acoustical Society of America*, vol. 30, no. 4, pp. 329–339, 1958.

[75] P. Marmottant and S. Hilgenfeldt, "Controlled vesicle deformation and lysis by single oscillating bubbles," *Nature*, vol. 423, no. 6936, p. 153, 2003.

[76] J. Wu, "Theoretical study on shear stress generated by microstreaming surrounding contrast agents attached to living cells," *Ultrasound in medicine & biology*, vol. 28, no. 1, pp. 125–129, 2002.

[77] F. Magaletti, M. Gallo, L. Marino, and C. M. Casciola, "Shock-induced collapse of a vapor nanobubble near solid boundaries," *International Journal of Multiphase Flow*, vol. 84, pp. 34–45, 2016.

[78] C.-D. Ohl, M. Arora, R. Dijkink, V. Janve, and D. Lohse, "Surface cleaning from laser-induced cavitation bubbles," *Applied physics letters*, vol. 89, no. 7, p. 074102, 2006.

[79] Z. Li, C. Ohl, J. Zhang, J. Tsai, and A. Liu, "Fast localized single cell membrane poration by bubble-induced jetting flow," in *2012 IEEE 25th International Conference on Micro Electro Mechanical Systems (MEMS)*, pp. 819–822, IEEE, 2012.

[80] M. W. Miller, D. L. Miller, and A. A. Brayman, "A review of in vitro bioeffects of inertial ultrasonic cavitation from a mechanistic perspective," *Ultrasound in medicine & biology*, vol. 22, no. 9, pp. 1131–1154, 1996.

[81] R. G. Holt and R. A. Roy, "Measurements of bubble-enhanced heating from focused, mhz-frequency ultrasound in a tissue-mimicking material," *Ultrasound in medicine & biology*, vol. 27, no. 10, pp. 1399–1412, 2001.

[82] S. Hilgenfeldt and D. Lohse, "The acoustics of diagnostic microbubbles: dissipative effects and heat deposition," *Ultrasonics*, vol. 38, no. 1-8, pp. 99–104, 2000.

[83] A. Yudina, M. De Smet, M. Lepetit-Coiffe, S. Langereis, L. Van Ruijssevelt, P. Smirnov, V. Bouchaud, P. Voisin, H. Grüll, and C. Moonen, "Ultrasound-mediated intracellular drug delivery using microbubbles and temperature-sensitive liposomes," *Journal of controlled release*, vol. 155, no. 3, pp. 442–448, 2011.

[84] A. Prosperetti, "Thermal effects and damping mechanisms in the forced radial oscillations of gas bubbles in liquids," *The Journal of the Acoustical Society of America*, vol. 61, no. 1, pp. 17–27, 1977.

[85] K. S. Suslick, "Sonochemistry," *science*, vol. 247, no. 4949, pp. 1439–1446, 1990.

[86] E. B. Flint and K. S. Suslick, "The temperature of cavitation," *Science*, vol. 253, no. 5026, pp. 1397–1399, 1991.

[87] P. Riesz and T. Kondo, "Free radical formation induced by ultrasound and its biological implications," *Free Radical Biology and Medicine*, vol. 13, no. 3, pp. 247–270, 1992.

[88] T. Devasagayam, J. Tilak, K. Boloor, K. S. Sane, S. S. Ghaskadbi, and R. Lele, "Free radicals and antioxidants in human health: current status and future prospects," *Japi*, vol. 52, no. 794804, p. 4, 2004.

[89] C. C. Winterbourn, "Reconciling the chemistry and biology of reactive oxygen species," *Nature chemical biology*, vol. 4, no. 5, p. 278, 2008.

[90] C. McEwan, S. Kamila, J. Owen, H. Nesbitt, B. Callan, M. Borden, N. Nomikou, R. A. Hamoudi, M. A. Taylor, E. Stride, *et al.*, "Combined sonodynamic and antimetabolite therapy for the improved treatment of pancreatic cancer using oxygen loaded microbubbles as a delivery vehicle," *Biomaterials*, vol. 80, pp. 20–32, 2016.

[91] P. Riesz, D. Berdahl, and C. Christman, "Free radical generation by ultrasound in aqueous and nonaqueous solutions.," *Environmental Health Perspectives*, vol. 64, pp. 233–252, 1985.

[92] T. Leighton, A. Walton, and M. Pickworth, "Primary bjerknes forces," *European Journal of Physics*, vol. 11, no. 1, p. 47, 1990.

[93] P. Dayton, A. Klibanov, G. Brandenburger, and K. Ferrara, "Acoustic radiation force in vivo: a mechanism to assist targeting of microbubbles," *Ultrasound in medicine & biology*, vol. 25, no. 8, pp. 1195–1201, 1999.

[94] P. A. Dayton, J. S. Allen, and K. W. Ferrara, "The magnitude of radiation force on ultrasound contrast agents," *The Journal of the Acoustical Society of America*, vol. 112, no. 5, pp. 2183–2192, 2002.

[95] J. J. Rychak, A. L. Klibanov, and J. A. Hossack, "Acoustic radiation force enhances targeted delivery of ultrasound contrast microbubbles: in vitro verification," *IEEE transactions on ultrasonics, ferroelectrics, and frequency control*, vol. 52, no. 3, pp. 421–433, 2005.

[96] S. Wang, J. A. Hossack, A. L. Klibanov, and F. W. Mauldin Jr, "Binding dynamics of targeted microbubbles in response to modulated acoustic radiation force," *Physics in Medicine & Biology*, vol. 59, no. 2, p. 465, 2013.

[97] A. F. Lum, M. A. Borden, P. A. Dayton, D. E. Kruse, S. I. Simon, and K. W. Ferrara, "Ultrasound radiation force enables targeted deposition of model drug carriers loaded on microbubbles," *Journal of Controlled Release*, vol. 111, no. 1-2, pp. 128–134, 2006.

[98] H. A. Hancock, L. H. Smith, J. Cuesta, A. K. Durrani, M. Angstadt, M. L. Palmeri, E. Kimmel, and V. Frenkel, "Investigations into pulsed high-intensity focused ultrasound–enhanced delivery: preliminary evidence for a novel mechanism," *Ultrasound in medicine & biology*, vol. 35, no. 10, pp. 1722–1736, 2009.

[99] C. N. Acconcia, B. Y. Leung, and D. E. Goertz, "The microscale evolution of the erosion front of blood clots exposed to ultrasound stimulated microbubbles," *The Journal of the Acoustical Society of America*, vol. 139, no. 5, pp. EL135–EL141, 2016.

[100] C. F. Caskey, S. Qin, P. A. Dayton, and K. W. Ferrara, "Microbubble tunneling in gel phantoms," *The Journal of the Acoustical Society of America*, vol. 125, no. 5, pp. EL183–EL189, 2009.

[101] G. Samiotaki, F. Vlachos, Y.-S. Tung, and E. E. Konofagou, "A quantitative pressure and microbubble-size dependence study of focused ultrasound-induced blood-brain barrier opening reversibility in vivo using mri," *Magnetic resonance in medicine*, vol. 67, no. 3, pp. 769–777, 2012.

[102] R. Mettin, I. Akhatov, U. Parlitz, C. Ohl, and W. Lauterborn, "Bjerknes forces between small cavitation bubbles in a strong acoustic field," *Physical review E*, vol. 56, no. 3, p. 2924, 1997.

[103] Y. Yamakoshi, Y. Ozawa, M. Ida, and N. Masuda, "Effects of bjerknes forces on gas-filled microbubble trapping by ultrasonic waves," *Japanese Journal of Applied Physics*, vol. 40, no. 5S, p. 3852, 2001.

[104] P. Dayton, A. Goode, K. Morgan, S. Klibanov, G. Brandenburger, and K. Ferrara, "Action of microbubbles when insonified: experimental evidence," in *1996 IEEE Ultrasonics Symposium. Proceedings*, vol. 2, pp. 1131–1134, IEEE, 1996.

[105] X. Chen, J. Wang, J. J. Pacella, and F. S. Villanueva, "Dynamic behavior of microbubbles during long ultrasound tone-burst excitation: Mechanistic insights into ultrasound-microbubble mediated therapeutics using high-speed imaging and cavitation detection," *Ultrasound in medicine & biology*, vol. 42, no. 2, pp. 528–538, 2016.

[106] M. A. Borden, D. E. Kruse, C. F. Caskey, S. Zhao, P. A. Dayton, and K. W. Ferrara, “Influence of lipid shell physicochemical properties on ultrasound-induced microbubble destruction,” *IEEE transactions on ultrasonics, ferroelectrics, and frequency control*, vol. 52, no. 11, pp. 1992–2002, 2005.

[107] M. S. Tartis, J. McCallan, A. F. Lum, R. LaBell, S. M. Stieger, T. O. Matsunaga, and K. W. Ferrara, “Therapeutic effects of paclitaxel-containing ultrasound contrast agents,” *Ultrasound in medicine & biology*, vol. 32, no. 11, pp. 1771–1780, 2006.

[108] M. J. Shortencarier, P. A. Dayton, S. H. Bloch, P. A. Schumann, T. O. Matsunaga, and K. W. Ferrara, “A method for radiation-force localized drug delivery using gas-filled lipospheres,” *IEEE transactions on ultrasonics, ferroelectrics, and frequency control*, vol. 51, no. 7, pp. 822–831, 2004.

[109] D. L. Miller, S. V. Pislaru, and J. F. Greenleaf, “Sonoporation: mechanical dna delivery by ultrasonic cavitation,” *Somatic cell and molecular genetics*, vol. 27, no. 1-6, pp. 115–134, 2002.

[110] C. X. Deng, F. Sieling, H. Pan, and J. Cui, “Ultrasound-induced cell membrane porosity,” *Ultrasound in medicine & biology*, vol. 30, no. 4, pp. 519–526, 2004.

[111] I. Lentacker, I. De Cock, R. Deckers, S. De Smedt, and C. Moonen, “Understanding ultrasound induced sonoporation: definitions and underlying mechanisms,” *Advanced drug delivery reviews*, vol. 72, pp. 49–64, 2014.

[112] R. E. Kumon, M. Aehle, D. Sabens, P. Parikh, Y. Han, D. Kourennyi, and C. Deng, “Spatiotemporal effects of sonoporation measured by real-time calcium imaging,” *Ultrasound in medicine & biology*, vol. 35, no. 3, pp. 494–506, 2009.

[113] J. Park, Z. Fan, R. E. Kumon, M. E. El-Sayed, and C. X. Deng, “Modulation of intracellular ca2+ concentration in brain microvascular endothelial cells in vitro by acoustic cavitation,” *Ultrasound in medicine & biology*, vol. 36, no. 7, pp. 1176–1187, 2010.

[114] F. Hussein, C. Antonescu, and R. Karshafian, “Ultrasound and microbubble induced release from intracellular compartments,” *BMC biotechnology*, vol. 17, no. 1, p. 45, 2017.

[115] K. Miyake and P. L. McNeil, “Vesicle accumulation and exocytosis at sites of plasma membrane disruption.,” *The Journal of cell biology*, vol. 131, no. 6, pp. 1737–1745, 1995.

[116] A. Reddy, E. V. Caler, and N. W. Andrews, “Plasma membrane repair is mediated by ca2+-regulated exocytosis of lysosomes,” *Cell*, vol. 106, no. 2, pp. 157–169, 2001.

[117] A. Van Wamel, K. Kooiman, M. Harteveld, M. Emmer, J. Folkert, M. Versluis, and N. De Jong, “Vibrating microbubbles poking individual cells: drug transfer into cells via sonoporation,” *Journal of controlled release*, vol. 112, no. 2, pp. 149–155, 2006.

[118] S. M. Nejad, S. H. R. Hosseini, H. Akiyama, and K. Tachibana, “Optical observation of cell sonoporation with low intensity ultrasound,” *Biochemical and biophysical research communications*, vol. 413, no. 2, pp. 218–223, 2011.

[119] Z. Fan, H. Liu, M. Mayer, and C. X. Deng, “Spatiotemporally controlled single cell sonoporation,” *Proceedings of the National Academy of Sciences*, vol. 109, no. 41, pp. 16486–16491, 2012.

[120] Z. Fan, D. Chen, and C. X. Deng, “Characterization of the dynamic activities of a population of microbubbles driven by pulsed ultrasound exposure in sonoporation,” *Ultrasound in medicine & biology*, vol. 40, no. 6, pp. 1260–1272, 2014.

[121] Y. Hu, J. M. Wan, and C. Alfred, “Membrane perforation and recovery dynamics in microbubble-mediated sonoporation,” *Ultrasound in medicine & biology*, vol. 39, no. 12, pp. 2393–2405, 2013.

[122] M. Ward, J. Wu, and J.-F. Chiu, "Experimental study of the effects of optison concentration on sonoporation in vitro," *Ultrasound in medicine & biology*, vol. 26, no. 7, pp. 1169–1175, 2000.

[123] S. Le Gac, E. Zwaan, A. van den Berg, and C.-D. Ohl, "Sonoporation of suspension cells with a single cavitation bubble in a microfluidic confinement," *Lab on a Chip*, vol. 7, no. 12, pp. 1666–1672, 2007.

[124] P. Qin, L. Xu, T. Han, L. Du, and C. Alfred, "Effect of non-acoustic parameters on heterogeneous sonoporation mediated by single-pulse ultrasound and microbubbles," *Ultrasonics sonochemistry*, vol. 31, pp. 107–115, 2016.

[125] Y. Zhou, K. Yang, J. Cui, J. Ye, and C. Deng, "Controlled permeation of cell membrane by single bubble acoustic cavitation," *Journal of controlled release*, vol. 157, no. 1, pp. 103–111, 2012.

[126] A. Xie, T. Belcik, Y. Qi, T. K. Morgan, S. A. Champaneri, S. Taylor, B. P. Davidson, Y. Zhao, A. L. Klibanov, M. A. Kuliszewski, *et al.*, "Ultrasound-mediated vascular gene transfection by cavitation of endothelial-targeted cationic microbubbles," *JACC: Cardiovascular Imaging*, vol. 5, no. 12, pp. 1253–1262, 2012.

[127] Y. Zhou, R. E. Kumon, C. X. Deng, and J. Cui, "The size of sonoporation pores on the cell membrane," in *2008 IEEE Ultrasonics Symposium*, pp. 558–561, IEEE, 2008.

[128] K. Kooiman, M. Foppen-Harteveld, A. F. van der Steen, and N. de Jong, "Sonoporation of endothelial cells by vibrating targeted microbubbles," *Journal of controlled release*, vol. 154, no. 1, pp. 35–41, 2011.

[129] N. Kudo, K. Okada, and K. Yamamoto, "Sonoporation by single-shot pulsed ultrasound with microbubbles adjacent to cells," *Biophysical journal*, vol. 96, no. 12, pp. 4866–4876, 2009.

[130] P. Prentice, A. Cuschieri, K. Dholakia, M. Prausnitz, and P. Campbell, "Membrane disruption by optically controlled microbubble cavitation," *Nature physics*, vol. 1, no. 2, p. 107, 2005.

[131] H. Chen, W. Kreider, A. A. Brayman, M. R. Bailey, and T. J. Matula, "Blood vessel deformations on microsecond time scales by ultrasonic cavitation," *Physical review letters*, vol. 106, no. 3, p. 034301, 2011.

[132] C. F. Caskey, S. M. Stieger, S. Qin, P. A. Dayton, and K. W. Ferrara, "Direct observations of ultrasound microbubble contrast agent interaction with the microvessel wall," *The Journal of the Acoustical Society of America*, vol. 122, no. 2, pp. 1191–1200, 2007.

[133] E. E. Konofagou, "Optimization of the ultrasound-induced blood-brain barrier opening," *Theranostics*, vol. 2, no. 12, p. 1223, 2012.

[134] L. J. Juffermans, A. van Dijk, C. A. Jongenelen, B. Drukarch, A. Reijerkerk, H. E. de Vries, O. Kamp, and R. J. Musters, "Ultrasound and microbubble-induced intra-and intercellular bioeffects in primary endothelial cells," *Ultrasound in medicine & biology*, vol. 35, no. 11, pp. 1917–1927, 2009.

[135] A. Abu Taha and H.-J. Schnittler, "Dynamics between actin and the ve-cadherin/catenin complex: novel aspects of the arp2/3 complex in regulation of endothelial junctions," *Cell adhesion & migration*, vol. 8, no. 2, pp. 125–135, 2014.

[136] K. Noda, J. Zhang, S. Fukuhara, S. Kunimoto, M. Yoshimura, and N. Mochizuki, "Vascular endothelial-cadherin stabilizes at cell–cell junctions by anchoring to circumferential actin bundles through α-and β-catenins in cyclic amp-epac-rap1 signal-activated endothelial cells," *Molecular biology of the cell*, vol. 21, no. 4, pp. 584–596, 2010.

[137] Y. A. Komarova, K. Kruse, D. Mehta, and A. B. Malik, "Protein interactions at endothelial junctions and signaling mechanisms regulating endothelial permeability," *Circulation research*, vol. 120, no. 1, pp. 179–206, 2017.

[138] Q. Yao, J. Chen, H. Cao, J. D. Orth, J. M. McCaffery, R.-V. Stan, and M. A. McNiven, “Caveolin-1 interacts directly with dynamin-2,” *Journal of molecular biology*, vol. 348, no. 2, pp. 491–501, 2005.

[139] N. Mizrahi, E. H. Zhou, G. Lenormand, R. Krishnan, D. Weihs, J. P. Butler, D. A. Weitz, J. J. Fredberg, and E. Kimmel, “Low intensity ultrasound perturbs cytoskeleton dynamics,” *Soft matter*, vol. 8, no. 8, pp. 2438–2443, 2012.

[140] S. Zhang, J. Cheng, and Y.-X. Qin, “Mechanobiological modulation of cytoskeleton and calcium influx in osteoblastic cells by short-term focused acoustic radiation force,” *PloS one*, vol. 7, no. 6, p. e38343, 2012.

[141] L. Juffermans, P. A. Dijkmans, R. Musters, C. A. Visser, and O. Kamp, “Transient permeabilization of cell membranes by ultrasound-exposed microbubbles is related to formation of hydrogen peroxide,” *American Journal of Physiology-Heart and Circulatory Physiology*, vol. 291, no. 4, pp. H1595–H1601, 2006.

[142] R. K. Schlicher, H. Radhakrishna, T. P. Tolentino, R. P. Apkarian, V. Zarnitsyn, and M. R. Prausnitz, “Mechanism of intracellular delivery by acoustic cavitation,” *Ultrasound in medicine & biology*, vol. 32, no. 6, pp. 915–924, 2006.

[143] J. L. Goldstein, R. G. Anderson, and M. S. Brown, “Coated pits, coated vesicles, and receptor-mediated endocytosis,” *Nature*, vol. 279, no. 5715, p. 679, 1979.

[144] T. P. Stossel, “Phagocytosis,” *New England Journal of Medicine*, vol. 290, no. 13, pp. 717–723, 1974.

[145] H. Holter, “Pinocytosis,” in *International review of cytology*, vol. 8, pp. 481–504, Elsevier, 1959.

[146] F. Fekri, R. C. D. Santos, R. Karshafian, and C. N. Antonescu, “Ultrasound microbubble treatment enhances clathrin-mediated endocytosis and

fluid-phase uptake through distinct mechanisms," *PloS one*, vol. 11, no. 6, p. e0156754, 2016.

[147] Z. Fan, Y. Sun, D. Chen, D. Tay, W. Chen, C. X. Deng, and J. Fu, "Acoustic tweezing cytometry for live-cell subcellular modulation of intracellular cytoskeleton contractility," *Scientific reports*, vol. 3, p. 2176, 2013.

[148] J. Hauser, M. Hauser, G. Muhr, and S. Esenwein, "Ultrasound-induced modifications of cytoskeletal components in osteoblast-like saos-2 cells," *Journal of Orthopaedic Research*, vol. 27, no. 3, pp. 286–294, 2009.

[149] G. Apodaca, "Modulation of membrane traffic by mechanical stimuli," *American Journal of Physiology-Renal Physiology*, vol. 282, no. 2, pp. F179–F190, 2002.

[150] B. D. Meijering, L. J. Juffermans, A. van Wamel, R. H. Henning, I. S. Zuhorn, M. Emmer, A. M. Versteilen, W. J. Paulus, W. H. van Gilst, K. Kooiman, *et al.*, "Ultrasound and microbubble-targeted delivery of macromolecules is regulated by induction of endocytosis and pore formation," *Circulation research*, vol. 104, no. 5, pp. 679–687, 2009.

[151] I. De Cock, E. Zagato, K. Braeckmans, Y. Luan, N. de Jong, S. C. De Smedt, and I. Lentacker, "Ultrasound and microbubble mediated drug delivery: acoustic pressure as determinant for uptake via membrane pores or endocytosis," *Journal of controlled release*, vol. 197, pp. 20–28, 2015.

[152] P. L. McNeil and M. Terasaki, "Coping with the inevitable: how cells repair a torn surface membrane," *Nature cell biology*, vol. 3, no. 5, p. E124, 2001.

[153] P. L. McNeil and R. A. Steinhardt, "Plasma membrane disruption: repair, prevention, adaptation," *Annual review of cell and developmental biology*, vol. 19, no. 1, pp. 697–731, 2003.

[154] V. Idone, C. Tam, J. W. Goss, D. Toomre, M. Pypaert, and N. W. Andrews, "Repair of injured plasma membrane by rapid ca2+-dependent endocytosis," *The Journal of cell biology*, vol. 180, no. 5, pp. 905–914, 2008.

[155] C. Christiansen, H. Kryvi, P. Sontum, and T. Skotland, "Physical and biochemical characterization of albunex, a new ultrasound contrast agent consisting of air-filled albumin microspheres suspended in a solution of human albumin," *Biotechnology and applied biochemistry*, vol. 19, no. 3, pp. 307–320, 1994.

[156] T. K. Kim, J. K. Han, A. Y. Kim, and B. I. Choi, "Limitations of characterization of hepatic hemangiomas using a sonographic contrast agent (levovist) and power doppler ultrasonography.," *Journal of ultrasound in medicine*, vol. 18, no. 11, pp. 737–743, 1999.

[157] J.-M. Correas, L. Bridal, A. Lesavre, A. Méjean, M. Claudon, and O. Hélénon, "Ultrasound contrast agents: properties, principles of action, tolerance, and artifacts," *European radiology*, vol. 11, no. 8, pp. 1316–1328, 2001.

[158] S. R. Sirsi and M. A. Borden, "State-of-the-art materials for ultrasound-triggered drug delivery," *Advanced drug delivery reviews*, vol. 72, pp. 3–14, 2014.

[159] J. M. Tsutsui, F. Xie, and R. T. Porter, "The use of microbubbles to target drug delivery," *Cardiovascular Ultrasound*, vol. 2, no. 1, p. 23, 2004.

[160] E. Quaia, "Classification and safety of microbubble-based contrast agents," in *Contrast Media in Ultrasonography*, pp. 3–14, Springer, 2005.

[161] Z. Kauerová, *Targeting nanoparticle drug carriers: Functionalized microbubbles and their application in ultrasonography.* PhD thesis, Masarykova univerzita, Přírodovědecká fakulta, 2013.

[162] J. D. Kasprzak and F. J. Ten Cate, "New ultrasound contrast agents for left ventricular and myocardial opacification," *Herz*, vol. 23, no. 8, pp. 474–482, 1998.

[163] M. SCHNEIDER, "Characteristics of sonovue$^{\text{TM}}$," *Echocardiography*, vol. 16, pp. 743–746, 1999.

[164] H. Mulvana, E. Stride, J. V. Hajnal, and R. J. Eckersley, “Temperature dependent behavior of ultrasound contrast agents,” *Ultrasound in medicine & biology*, vol. 36, no. 6, pp. 925–934, 2010.

[165] J.-M. Escoffre, A. Novell, S. Serriere, T. Lecomte, and A. Bouakaz, “Irinotecan delivery by microbubble-assisted ultrasound: in vitro validation and a pilot preclinical study,” *Molecular pharmaceutics*, vol. 10, no. 7, pp. 2667–2675, 2013.

[166] T. Bettinger and F. Tranquart, “Design of microbubbles for gene/drug delivery,” in *Therapeutic Ultrasound*, pp. 191–204, Springer, 2016.

[167] B. Geers, I. Lentacker, N. N. Sanders, J. Demeester, S. Meairs, and S. C. De Smedt, “Self-assembled liposome-loaded microbubbles: The missing link for safe and efficient ultrasound triggered drug-delivery,” *Journal of controlled release*, vol. 152, no. 2, pp. 249–256, 2011.

[168] S. Ibsen, C. E. Schutt, and S. Esener, “Microbubble-mediated ultrasound therapy: a review of its potential in cancer treatment,” *Drug design, development and therapy*, vol. 7, p. 375, 2013.

[169] D. B. Ellegala, H. Leong-Poi, J. E. Carpenter, A. L. Klibanov, S. Kaul, M. E. Shaffrey, J. Sklenar, and J. R. Lindner, “Imaging tumor angiogenesis with contrast ultrasound and microbubbles targeted to α v β 3,” *Circulation*, vol. 108, no. 3, pp. 336–341, 2003.

[170] R. Riahi, A. Tamayol, S. A. M. Shaegh, A. M. Ghaemmaghami, M. R. Dokmeci, and A. Khademhosseini, “Microfluidics for advanced drug delivery systems,” *Current Opinion in Chemical Engineering*, vol. 7, pp. 101–112, 2015.

[171] E. K. Sackmann, A. L. Fulton, and D. J. Beebe, “The present and future role of microfluidics in biomedical research,” *Nature*, vol. 507, no. 7491, p. 181, 2014.

[172] E. Rondeau and J. J. Cooper-White, “Biopolymer microparticle and nanoparticle formation within a microfluidic device,” *Langmuir*, vol. 24, no. 13, pp. 6937–6945, 2008.

[173] L.-H. Hung, S.-Y. Teh, J. Jester, and A. P. Lee, “Plga micro/nanosphere synthesis by droplet microfluidic solvent evaporation and extraction approaches,” *Lab on a Chip*, vol. 10, no. 14, pp. 1820–1825, 2010.

[174] C. A. Serra, I. U. Khan, B. Cortese, M. H. de Croon, V. Hessel, T. Ono, N. Anton, and T. Vandamme, “Microfluidic production of micro-and nanoparticles,” *Encyclopedia of Polymer Science and Technology*, 2002.

[175] L. Liu and S. Choi, “Self-sustainable, high-power-density bio-solar cells for lab-on-a-chip applications,” *Lab on a Chip*, vol. 17, no. 22, pp. 3817–3825, 2017.

[176] D. A. Lavan, T. McGuire, and R. Langer, “Small-scale systems for in vivo drug delivery,” *Nature biotechnology*, vol. 21, no. 10, p. 1184, 2003.

[177] E. W. Esch, A. Bahinski, and D. Huh, “Organs-on-chips at the frontiers of drug discovery,” *Nature reviews Drug discovery*, vol. 14, no. 4, p. 248, 2015.

[178] S. N. Bhatia and D. E. Ingber, “Microfluidic organs-on-chips,” *Nature biotechnology*, vol. 32, no. 8, p. 760, 2014.

[179] I. Wagner, E.-M. Materne, S. Brincker, U. Süßbier, C. Frädrich, M. Busek, F. Sonntag, D. A. Sakharov, E. V. Trushkin, A. G. Tonevitsky, *et al.*, “A dynamic multi-organ-chip for long-term cultivation and substance testing proven by 3d human liver and skin tissue co-culture,” *Lab on a Chip*, vol. 13, no. 18, pp. 3538–3547, 2013.

[180] N. S. Bhise, J. Ribas, V. Manoharan, Y. S. Zhang, A. Polini, S. Massa, M. R. Dokmeci, and A. Khademhosseini, “Organ-on-a-chip platforms for studying drug delivery systems,” *Journal of Controlled Release*, vol. 190, pp. 82–93, 2014.

[181] A. Sontheimer-Phelps, B. A. Hassell, and D. E. Ingber, "Modelling cancer in microfluidic human organs-on-chips," *Nature Reviews Cancer*, p. 1, 2019.

[182] K. Ronaldson-Bouchard and G. Vunjak-Novakovic, "Organs-on-a-chip: a fast track for engineered human tissues in drug development," *Cell Stem Cell*, vol. 22, no. 3, pp. 310–324, 2018.

[183] U. Marx, H. Walles, S. Hoffmann, G. Lindner, R. Horland, F. Sonntag, U. Klotzbach, D. Sakharov, A. Tonevitsky, and R. Lauster, "'human-on-a-chip'developments: a translational cutting-edge alternative to systemic safety assessment and efficiency evaluation of substances in laboratory animals and man?," *Alternatives to Laboratory Animals*, vol. 40, no. 5, pp. 235–257, 2012.

[184] W. A. Muller, "How endothelial cells regulate transmigration of leukocytes in the inflammatory response," *The American journal of pathology*, vol. 184, no. 4, pp. 886–896, 2014.

[185] S. Huveneers, M. J. Daemen, and P. L. Hordijk, "Between rho (k) and a hard place: the relation between vessel wall stiffness, endothelial contractility, and cardiovascular disease," *Circulation research*, vol. 116, no. 5, pp. 895–908, 2015.

[186] A. S. Harney, E. N. Arwert, D. Entenberg, Y. Wang, J. G. Jones, and J. S. Condeelis, "Perivascular macrophages induce localized, transient blood vessel permeability and tumor cell intravasation," 2014.

[187] D. Correa, R. A. Somoza, P. Lin, W. P. Schiemann, and A. I. Caplan, "Mesenchymal stem cells regulate melanoma cancer cells extravasation to bone and liver at their perivascular niche," *International journal of cancer*, vol. 138, no. 2, pp. 417–427, 2016.

[188] L. Cucullo, M. Hossain, V. Puvenna, N. Marchi, and D. Janigro, "The role of shear stress in blood-brain barrier endothelial physiology," *BMC neuroscience*, vol. 12, no. 1, p. 40, 2011.

[189] J. W. Song and L. L. Munn, “Fluid forces control endothelial sprouting,” *Proceedings of the National Academy of Sciences*, vol. 108, no. 37, pp. 15342–15347, 2011.

[190] N. Resnick, H. Yahav, A. Shay-Salit, M. Shushy, S. Schubert, L. C. M. Zilberman, and E. Wofovitz, “Fluid shear stress and the vascular endothelium: for better and for worse,” *Progress in biophysics and molecular biology*, vol. 81, no. 3, pp. 177–199, 2003.

[191] E. Tzima, M. Irani-Tehrani, W. B. Kiosses, E. Dejana, D. A. Schultz, B. Engelhardt, G. Cao, H. DeLisser, and M. A. Schwartz, “A mechanosensory complex that mediates the endothelial cell response to fluid shear stress,” *Nature*, vol. 437, no. 7057, p. 426, 2005.

[192] D. C. Brown and R. S. Larson, “Improvements to parallel plate flow chambers to reduce reagent and cellular requirements,” *BMC immunology*, vol. 2, no. 1, p. 9, 2001.

[193] L. Cucullo, M. Hossain, E. Rapp, T. Manders, N. Marchi, and D. Janigro, “Development of a humanized in vitro blood–brain barrier model to screen for brain penetration of antiepileptic drugs,” *Epilepsia*, vol. 48, no. 3, pp. 505–516, 2007.

[194] B. Prabhakarpandian, K. Pant, R. C. Scott, C. B. Patillo, D. Irimia, M. F. Kiani, and S. Sundaram, “Synthetic microvascular networks for quantitative analysis of particle adhesion,” *Biomedical microdevices*, vol. 10, no. 4, pp. 585–595, 2008.

[195] W. A. Farahat, L. B. Wood, I. K. Zervantonakis, A. Schor, S. Ong, D. Neal, R. D. Kamm, and H. H. Asada, “Ensemble analysis of angiogenic growth in three-dimensional microfluidic cell cultures,” *PloS one*, vol. 7, no. 5, p. e37333, 2012.

[196] M. I. Bogorad, J. DeStefano, J. Karlsson, A. D. Wong, S. Gerecht, and P. C. Searson, “in vitro microvessel models,” *Lab on a Chip*, vol. 15, no. 22, pp. 4242–4255, 2015.

[197] J. R. Anderson, D. T. Chiu, R. J. Jackman, O. Cherniavskaya, J. C. McDonald, H. Wu, S. H. Whitesides, and G. M. Whitesides, "Fabrication of topologically complex three-dimensional microfluidic systems in pdms by rapid prototyping," *Analytical chemistry*, vol. 72, no. 14, pp. 3158–3164, 2000.

[198] J. C. McDonald, D. C. Duffy, J. R. Anderson, D. T. Chiu, H. Wu, O. J. Schueller, and G. M. Whitesides, "Fabrication of microfluidic systems in poly (dimethylsiloxane)," *ELECTROPHORESIS: An International Journal*, vol. 21, no. 1, pp. 27–40, 2000.

[199] S. K. Sia and G. M. Whitesides, "Microfluidic devices fabricated in poly (dimethylsiloxane) for biological studies," *Electrophoresis*, vol. 24, no. 21, pp. 3563–3576, 2003.

[200] M. Tsai, A. Kita, J. Leach, R. Rounsevell, J. N. Huang, J. Moake, R. E. Ware, D. A. Fletcher, and W. A. Lam, "In vitro modeling of the microvascular occlusion and thrombosis that occur in hematologic diseases using microfluidic technology," *The Journal of clinical investigation*, vol. 122, no. 1, 2011.

[201] S. Chung, R. Sudo, V. Vickerman, I. K. Zervantonakis, and R. D. Kamm, "Microfluidic platforms for studies of angiogenesis, cell migration, and cell–cell interactions," *Annals of biomedical engineering*, vol. 38, no. 3, pp. 1164–1177, 2010.

[202] L. Businaro, A. De Ninno, G. Schiavoni, V. Lucarini, G. Ciasca, A. Gerardino, F. Belardelli, L. Gabriele, and F. Mattei, "Cross talk between cancer and immune cells: exploring complex dynamics in a microfluidic environment," *Lab on a Chip*, vol. 13, no. 2, pp. 229–239, 2013.

[203] S. Kim, W. Kim, S. Lim, and J. Jeon, "Vasculature-on-a-chip for in vitro disease models," *Bioengineering*, vol. 4, no. 1, p. 8, 2017.

[204] S. Parlato, A. De Ninno, R. Molfetta, E. Toschi, D. Salerno, A. Mencattini, G. Romagnoli, A. Fragale, L. Roccazzello, M. Buoncervello, *et al.*, "3d microfluidic model for evaluating immunotherapy efficacy by tracking dendritic cell behaviour toward tumor cells," *Scientific reports*, vol. 7, no. 1, p. 1093, 2017.

[205] C. F. Buchanan, S. S. Verbridge, P. P. Vlachos, and M. N. Rylander, "Flow shear stress regulates endothelial barrier function and expression of angiogenic factors in a 3d microfluidic tumor vascular model," *Cell adhesion & migration*, vol. 8, no. 5, pp. 517–524, 2014.

[206] I. K. Zervantonakis, S. K. Hughes-Alford, J. L. Charest, J. S. Condeelis, F. B. Gertler, and R. D. Kamm, "Three-dimensional microfluidic model for tumor cell intravasation and endothelial barrier function," *Proceedings of the National Academy of Sciences*, vol. 109, no. 34, pp. 13515–13520, 2012.

[207] Y. Shin, S. Han, J. S. Jeon, K. Yamamoto, I. K. Zervantonakis, R. Sudo, R. D. Kamm, and S. Chung, "Microfluidic assay for simultaneous culture of multiple cell types on surfaces or within hydrogels," *Nature protocols*, vol. 7, no. 7, p. 1247, 2012.

[208] B. Prabhakarpandian, M.-C. Shen, J. B. Nichols, I. R. Mills, M. Sidoryk-Wegrzynowicz, M. Aschner, and K. Pant, "Sym-bbb: a microfluidic blood brain barrier model," *Lab on a Chip*, vol. 13, no. 6, pp. 1093–1101, 2013.

[209] Y. Zheng, J. Chen, M. Craven, N. W. Choi, S. Totorica, A. Diaz-Santana, P. Kermani, B. Hempstead, C. Fischbach-Teschl, J. A. López, *et al.*, "In vitro microvessels for the study of angiogenesis and thrombosis," *Proceedings of the national academy of sciences*, vol. 109, no. 24, pp. 9342–9347, 2012.

[210] K. H. Wong, J. M. Chan, R. D. Kamm, and J. Tien, "Microfluidic models of vascular functions," *Annual review of biomedical engineering*, vol. 14, pp. 205–230, 2012.

[211] B. M. Baker, B. Trappmann, S. C. Stapleton, E. Toro, and C. S. Chen, “Microfluidics embedded within extracellular matrix to define vascular architectures and pattern diffusive gradients,” *Lab on a chip*, vol. 13, no. 16, pp. 3246–3252, 2013.

[212] L. L. Bischel, E. W. Young, B. R. Mader, and D. J. Beebe, “Tubeless microfluidic angiogenesis assay with three-dimensional endothelial-lined microvessels,” *Biomaterials*, vol. 34, no. 5, pp. 1471–1477, 2013.

[213] A. D. Wong and P. C. Searson, “Live-cell imaging of invasion and intravasation in an artificial microvessel platform,” *Cancer research*, vol. 74, no. 17, pp. 4937–4945, 2014.

[214] O. Sarig-Nadir, N. Livnat, R. Zajdman, S. Shoham, and D. Seliktar, “Laser photoablation of guidance microchannels into hydrogels directs cell growth in three dimensions,” *Biophysical journal*, vol. 96, no. 11, pp. 4743–4752, 2009.

[215] A. Hasan, A. Paul, N. E. Vrana, X. Zhao, A. Memic, Y.-S. Hwang, M. R. Dokmeci, and A. Khademhosseini, “Microfluidic techniques for development of 3d vascularized tissue,” *Biomaterials*, vol. 35, no. 26, pp. 7308–7325, 2014.

[216] J. H. Yeon, H. R. Ryu, M. Chung, Q. P. Hu, and N. L. Jeon, “In vitro formation and characterization of a perfusable three-dimensional tubular capillary network in microfluidic devices,” *Lab on a Chip*, vol. 12, no. 16, pp. 2815–2822, 2012.

[217] D.-H. T. Nguyen, S. C. Stapleton, M. T. Yang, S. S. Cha, C. K. Choi, P. A. Galie, and C. S. Chen, “Biomimetic model to reconstitute angiogenic sprouting morphogenesis in vitro,” *Proceedings of the National Academy of Sciences*, vol. 110, no. 17, pp. 6712–6717, 2013.

[218] W. T. Shi, F. Forsberg, P. Vaidyanathan, A. Tornes, J. Østensen, and B. B. Goldberg, “The influence of acoustic transmit parameters on the destruction of contrast microbubbles in vitro,” *Physics in medicine and biology*, vol. 51, no. 16, p. 4031, 2006.

[219] R. Karshafian, P. D. Bevan, R. Williams, S. Samac, and P. N. Burns, “Sonoporation by ultrasound-activated microbubble contrast agents: effect of acoustic exposure parameters on cell membrane permeability and cell viability,” *Ultrasound in medicine & biology*, vol. 35, no. 5, pp. 847–860, 2009.

[220] A. van Wamel, A. Bouakaz, M. Versluis, and N. de Jong, “Micromanipulation of endothelial cells: ultrasound-microbubble-cell interaction,” *Ultrasound in medicine & biology*, vol. 30, no. 9, pp. 1255–1258, 2004.

[221] Y. Lin, L. Lin, M. Cheng, L. Jin, L. Du, T. Han, L. Xu, A. C. Yu, and P. Qin, “Effect of acoustic parameters on the cavitation behavior of sonovue microbubbles induced by pulsed ultrasound,” *Ultrasonics Sonochemistry*, vol. 35, no. Part A, pp. 176 – 184, 2017.

[222] Y. C. Park, C. Zhang, S. Kim, G. Mohamedi, C. Beigie, J. O. Nagy, R. G. Holt, R. O. Cleveland, N. L. Jeon, and J. Y. Wong, “Microvessels-on-a-chip to assess targeted ultrasound-assisted drug delivery,” *ACS applied materials & interfaces*, vol. 8, no. 46, pp. 31541–31549, 2016.

[223] S. P. Deosarkar, B. Prabhakarpandian, B. Wang, J. B. Sheffield, B. Krynska, and M. F. Kiani, “A novel dynamic neonatal blood-brain barrier on a chip,” *PloS one*, vol. 10, no. 11, p. e0142725, 2015.

[224] T. B. Terrell-Hall, A. G. Ammer, J. I. Griffith, and P. R. Lockman, “Permeability across a novel microfluidic blood-tumor barrier model,” *Fluids and Barriers of the CNS*, vol. 14, no. 1, p. 3, 2017.

[225] J. M. Tarbell, “Shear stress and the endothelial transport barrier,” *Cardiovascular research*, vol. 87, no. 2, pp. 320–330, 2010.

[226] J. G. DeStefano, Z. S. Xu, A. J. Williams, N. Yimam, and P. C. Searson, “Effect of shear stress on ipsc-derived human brain microvascular endothelial cells (dhbmecs),” *Fluids and Barriers of the CNS*, vol. 14, no. 1, p. 20, 2017.

[227] R. Apfel, "Acoustic cavitation: a possible consequence of biomedical uses of ultrasound.," *The British journal of cancer. Supplement*, vol. 5, p. 140, 1982.

[228] H. Flynn and C. C. Church, "A mechanism for the generation of cavitation maxima by pulsed ultrasound," *The Journal of the Acoustical Society of America*, vol. 76, no. 2, pp. 505–512, 1984.

[229] C. K. Holland and R. E. Apfel, "An improved theory for the prediction of microcavitation thresholds," *IEEE transactions on ultrasonics, ferroelectrics, and frequency control*, vol. 36, no. 2, pp. 204–208, 1989.

[230] R. E. Apfel and C. K. Holland, "Gauging the likelihood of cavitation from short-pulse, low-duty cycle diagnostic ultrasound," *Ultrasound in medicine & biology*, vol. 17, no. 2, pp. 179–185, 1991.

[231] G. Ter Haar, "Safety and bio-effects of ultrasound contrast agents," *Medical & biological engineering & computing*, vol. 47, no. 8, pp. 893–900, 2009.

[232] S. B. Barnett, G. R. Ter Haar, M. C. Ziskin, H.-D. Rott, F. A. Duck, and K. Maeda, "International recommendations and guidelines for the safe use of diagnostic ultrasound in medicine," *Ultrasound in medicine & biology*, vol. 26, no. 3, pp. 355–366, 2000.

[233] K. Hynynen, N. McDannold, N. Vykhodtseva, and F. A. Jolesz, "Noninvasive mr imaging–guided focal opening of the blood-brain barrier in rabbits," *Radiology*, vol. 220, no. 3, pp. 640–646, 2001.

[234] S. Datta, C.-C. Coussios, L. E. McAdory, J. Tan, T. Porter, G. De Courten-Myers, and C. K. Holland, "Correlation of cavitation with ultrasound enhancement of thrombolysis," *Ultrasound in medicine & biology*, vol. 32, no. 8, pp. 1257–1267, 2006.

[235] O. Louisnard and J. González-García, "Acoustic cavitation," in *Ultrasound technologies for food and bioprocessing*, pp. 13–64, Springer, 2011.

[236] E. Neppiras and B. Noltingk, “Cavitation produced by ultrasonics: theoretical conditions for the onset of cavitation,” *Proceedings of the Physical Society. Section B*, vol. 64, no. 12, p. 1032, 1951.

[237] F. G. Blake Jr, “Onset of cavitation in liquids.,” 1949.

[238] M. S. Plesset and A. Prosperetti, “Bubble dynamics and cavitation,” *Annual review of fluid mechanics*, vol. 9, no. 1, pp. 145–185, 1977.

[239] W. H. Besant, *A treatise on hydrostatics and hydrodynamics.* Deighton, Bell, 1859.

[240] L. Rayleigh, “Viii. on the pressure developed in a liquid during the collapse of a spherical cavity,” *The London, Edinburgh, and Dublin Philosophical Magazine and Journal of Science*, vol. 34, no. 200, pp. 94–98, 1917.

[241] M. S. Plesset, “The dynamics of cavitation bubbles,” *Journal of applied mechanics*, vol. 16, pp. 277–282, 1949.

[242] B. E. Noltingk and E. A. Neppiras, “Cavitation produced by ultrasonics,” *Proceedings of the Physical Society. Section B*, vol. 63, no. 9, p. 674, 1950.

[243] W. Lauterborn and T. Kurz, “Physics of bubble oscillations,” *Reports on progress in physics*, vol. 73, no. 10, p. 106501, 2010.

[244] M. Minnaert, “Xvi. on musical air-bubbles and the sounds of running water,” *The London, Edinburgh, and Dublin Philosophical Magazine and Journal of Science*, vol. 16, no. 104, pp. 235–248, 1933.

[245] V. Sboros, C. MacDonald, S. Pye, C. Moran, J. Gomatam, and W. McDicken, “The dependence of ultrasound contrast agents backscatter on acoustic pressure: theory versus experiment,” *Ultrasonics*, vol. 40, no. 1-8, pp. 579–583, 2002.

[246] M.-X. Tang and R. J. Eckersley, “Frequency and pressure dependent attenuation and scattering by microbubbles,” *Ultrasound in medicine & biology*, vol. 33, no. 1, pp. 164–168, 2007.

[247] W. Lauterborn, “Numerical investigation of nonlinear oscillations of gas bubbles in liquids,” *The Journal of the Acoustical Society of America*, vol. 59, no. 2, pp. 283–293, 1976.

[248] M. Azmin, C. Harfield, Z. Ahmad, M. Edirisinghe, and E. Stride, “How do microbubbles and ultrasound interact? basic physical, dynamic and engineering principles,” *Current pharmaceutical design*, vol. 18, no. 15, pp. 2118–2134, 2012.

[249] c. e. P. Epstein and M. S. Plesset, “On the stability of gas bubbles in liquid-gas solutions,” *The Journal of Chemical Physics*, vol. 18, no. 11, pp. 1505–1509, 1950.

[250] N. de Jong, L. Hoff, T. Skotland, and N. Bom, “Absorption and scatter of encapsulated gas filled microspheres: theoretical considerations and some measurements,” *Ultrasonics*, vol. 30, no. 2, pp. 95–103, 1992.

[251] N. de Jong and L. Hoff, “Ultrasound scattering properties of albunex microspheres,” *Ultrasonics*, vol. 31, no. 3, pp. 175–181, 1993.

[252] C. C. Church, “The effects of an elastic solid surface layer on the radial pulsations of gas bubbles,” *The Journal of the Acoustical Society of America*, vol. 97, no. 3, pp. 1510–1521, 1995.

[253] L. Hoff, P. C. Sontum, and J. M. Hovem, “Oscillations of polymeric microbubbles: Effect of the encapsulating shell,” *The Journal of the Acoustical Society of America*, vol. 107, no. 4, pp. 2272–2280, 2000.

[254] K. E. Morgan, J. S. Allen, P. A. Dayton, J. E. Chomas, A. Klibaov, and K. W. Ferrara, “Experimental and theoretical evaluation of microbubble behavior: Effect of transmitted phase and bubble size,” *IEEE transactions on ultrasonics, ferroelectrics, and frequency control*, vol. 47, no. 6, pp. 1494–1509, 2000.

[255] K. Sarkar, A. Katiyar, and P. Jain, “Growth and dissolution of an encapsulated contrast microbubble: effects of encapsulation permeability,” *Ultrasound in medicine & biology*, vol. 35, no. 8, pp. 1385–1396, 2009.

[256] L. Hoff, P. C. Sontum, and B. Hoff, “Acoustic properties of shell-encapsulated, gas-filled ultrasound contrast agents,” in *1996 IEEE Ultrasonics Symposium. Proceedings*, vol. 2, pp. 1441–1444, IEEE, 1996.

[257] P. Marmottant, S. van der Meer, M. Emmer, M. Versluis, N. de Jong, S. Hilgenfeldt, and D. Lohse, “A model for large amplitude oscillations of coated bubbles accounting for buckling and rupture,” *The Journal of the Acoustical Society of America*, vol. 118, no. 6, pp. 3499–3505, 2005.

[258] I. Langmuir, “The mechanism of the surface phenomena of flotation,” *Transactions of the Faraday Society*, vol. 15, no. June, pp. 62–74, 1920.

[259] S. Lee, D. H. Kim, and D. Needham, “Equilibrium and dynamic interfacial tension measurements at microscopic interfaces using a micropipet technique. 2. dynamics of phospholipid monolayer formation and equilibrium tensions at the water- air interface,” *Langmuir*, vol. 17, no. 18, pp. 5544–5550, 2001.

[260] N. De Jong, M. Emmer, C. T. Chin, A. Bouakaz, F. Mastik, D. Lohse, and M. Versluis, ““compression-only” behavior of phospholipid-coated contrast bubbles,” *Ultrasound in medicine & biology*, vol. 33, no. 4, pp. 653–656, 2007.

[261] H. Oguz and A. Prosperetti, “The natural frequency of oscillation of gas bubbles in tubes,” *The Journal of the Acoustical Society of America*, vol. 103, no. 6, pp. 3301–3308, 1998.

[262] H. Miao, S. M. Gracewski, and D. Dalecki, “Ultrasonic excitation of a bubble inside a deformable tube: Implications for ultrasonically induced hemorrhage,” *The Journal of the Acoustical Society of America*, vol. 124, no. 4, pp. 2374–2384, 2008.

[263] T. A. Hay, Y. A. Ilinskii, E. A. Zabolotskaya, and M. F. Hamilton, “Model for the dynamics of a spherical bubble undergoing small shape oscillations between parallel soft elastic layers,” *The Journal of the Acoustical Society of America*, vol. 134, no. 2, pp. 1454–1462, 2013.

[264] V. Bjerknes, *Fields of force: supplementary lectures, applications to meteorology; a course of lectures in mathematical physics delivered December 1 to 23, 1905.* No. 1, The Columbia university press, 1906.

[265] L. A. Crum, “Bjerknes forces on bubbles in a stationary sound field,” *The Journal of the Acoustical Society of America*, vol. 57, no. 6, pp. 1363–1370, 1975.

[266] H. J. Vos, F. Guidi, E. Boni, and P. Tortoli, “Method for microbubble characterization using primary radiation force,” *IEEE transactions on ultrasonics, ferroelectrics, and frequency control*, vol. 54, no. 7, pp. 1333–1345, 2007.

[267] V. Kazantsev, “The motion of gaseous bubbles in a liquid under the influence of bjerknes forces arising in an acoustic field,” in *Soviet Physics Doklady*, vol. 4, p. 1250, 1960.

[268] K. Yasui, J. Lee, T. Tuziuti, A. Towata, T. Kozuka, and Y. Iida, “Influence of the bubble-bubble interaction on destruction of encapsulated microbubbles under ultrasound,” *The Journal of the Acoustical Society of America*, vol. 126, no. 3, pp. 973–982, 2009.

[269] S. Harput, B. Raiton, J. R. McLaughlan, S. D. Evans, and S. Freear, “The periodicity between the aggregated microbubbles by secondary radiation force,” in *2011 IEEE International Ultrasonics Symposium*, pp. 1630–1633, IEEE, 2011.

[270] A. Doinikov and S. Zavtrak, “On the mutual interaction of two gas bubbles in a sound field,” *Physics of Fluids*, vol. 7, no. 8, pp. 1923–1930, 1995.

[271] A. A. Doinikov, "Bjerknes forces between two bubbles in a viscous fluid," *The Journal of the Acoustical Society of America*, vol. 106, no. 6, pp. 3305–3312, 1999.

[272] M. Ida, "Investigation of transition frequencies of two acoustically coupled bubbles using a direct numerical simulation technique," *Journal of the Physical Society of Japan*, vol. 73, no. 11, pp. 3026–3033, 2004.

[273] T. Barbat, N. Ashgriz, and C.-S. Liu, "Dynamics of two interacting bubbles in an acoustic field," *Journal of Fluid Mechanics*, vol. 389, pp. 137–168, 1999.

[274] W. G. Hertlein, "Practical photolithography for modern semiconductor production," in *Optical Microlithographic Technology for Integrated Circuit Fabrication and Inspection*, vol. 811, pp. 48–54, International Society for Optics and Photonics, 1987.

[275] Y. Xia and G. M. Whitesides, "Soft lithography," *Annual review of materials science*, vol. 28, no. 1, pp. 153–184, 1998.

[276] S. Parlato, A. De Ninno, R. Molfetta, E. Toschi, D. Salerno, A. Mencattini, G. Romagnoli, A. Fragale, L. Roccazzello, M. Buoncervello, *et al.*, "3d microfluidic model for evaluating immunotherapy efficacy by tracking dendritic cell behaviour toward tumor cells," *Scientific Reports*, vol. 7, 2017.

[277]

[278] D. B. Weibel, W. R. DiLuzio, and G. M. Whitesides, "Microfabrication meets microbiology," *Nature Reviews Microbiology*, vol. 5, no. 3, p. 209, 2007.

[279] S. Lelu, M. Afadzi, S. Berg, A. Åslund, S. H. Torp, W. Sattler, and C. d. L. Davies, "Primary porcine brain endothelial cells asin vitromodel to study effects of ultrasound and microbubbles on blood–brain barrier function," *IEEE transactions on ultrasonics, ferroelectrics, and frequency control*, vol. 64, no. 1, pp. 281–290, 2016.

[280] T. D. Pollard and J. A. Cooper, “Actin and actin-binding proteins. a critical evaluation of mechanisms and functions,” *Annual review of biochemistry*, vol. 55, no. 1, pp. 987–1035, 1986.

[281] J. Seebach, J. Cao, and H. Schnittler, “Quantitative dynamics of ve-cadherin at endothelial cell junctions at a glance: basic requirements and current concepts,” *Discoveries*, vol. 4, no. 3, p. e63, 2016.

[282] N. Jiménez, V. J. Krouwer, and J. A. Post, “A new, rapid and reproducible method to obtain high quality endothelium in vitro,” *Cytotechnology*, vol. 65, no. 1, pp. 1–14, 2013.

[283] E. Dejana and C. Giampietro, “Vascular endothelial-cadherin and vascular stability,” *Current opinion in hematology*, vol. 19, no. 3, pp. 218–223, 2012.

[284] M. B. Esch, D. J. Post, M. L. Shuler, and T. Stokol, “Characterization of in vitro endothelial linings grown within microfluidic channels,” *Tissue Engineering Part A*, vol. 17, no. 23-24, pp. 2965–2971, 2011.

[285] C. C. Kumar, “Signaling by integrin receptors,” *Oncogene*, vol. 17, no. 11, p. 1365, 1998.

[286] A. Carisey and C. Ballestrem, “Vinculin, an adapter protein in control of cell adhesion signalling,” *European journal of cell biology*, vol. 90, no. 2-3, pp. 157–163, 2011.

[287] B. Geiger, J. P. Spatz, and A. D. Bershadsky, “Environmental sensing through focal adhesions,” *Nature reviews Molecular cell biology*, vol. 10, no. 1, p. 21, 2009.

[288] L. Zanetta, S. G. Marcus, J. Vasile, M. Dobryansky, H. Cohen, K. Eng, P. Shamamian, and P. Mignatti, “Expression of von willebrand factor, an endothelial cell marker, is up-regulated by angiogenesis factors: A potential method for objective assessment of tumor angiogenesis,” *International journal of cancer*, vol. 85, no. 2, pp. 281–288, 2000.

[289] J. Seebach, G. Donnert, R. Kronstein, S. Werth, B. Wojciak-Stothard, D. Falzarano, C. Mrowietz, S. W. Hell, and H.-J. Schnittler, "Regulation of endothelial barrier function during flow-induced conversion to an arterial phenotype," *Cardiovascular research*, vol. 75, no. 3, pp. 598–607, 2007.

[290] W. H. Goldmann, R. Galneder, M. Ludwig, W. Xu, E. D. Adamson, N. Wang, and R. M. Ezzell, "Differences in elasticity of vinculin-deficient f9 cells measured by magnetometry and atomic force microscopy," *Experimental cell research*, vol. 239, no. 2, pp. 235–242, 1998.

[291] M. Cheng, F. Li, T. Han, C. Alfred, and P. Qin, "Effects of ultrasound pulse parameters on cavitation properties of flowing microbubbles under physiologically relevant conditions," *Ultrasonics sonochemistry*, vol. 52, pp. 512–521, 2019.

[292] K. Ivanov, M. Kalinina, and Y. I. Levkovich, "Blood flow velocity in capillaries of brain and muscles and its physiological significance," *Microvascular research*, vol. 22, no. 2, pp. 143–155, 1981.

[293] F. P. Branca, *Fondamenti di Ingegneria Clinica-Volume 2: Volume 2: Ecotomografia*, vol. 2. Springer Science & Business Media, 2008.